

©2020

SIDDHESH NARAYAN DALVI

ALL RIGHTS RESERVED

UNDERSTANDING CONTACT MECHANICS AND FRICTION ON ROUGH
SURFACES

A Dissertation

Presented to

The Graduate Faculty of The University of Akron

In Partial Fulfillment

of the Requirements for the Degree

Doctor of Philosophy

Siddhesh Narayan Dalvi

May, 2020

UNDERSTANDING CONTACT MECHANICS AND FRICTION ON ROUGH
SURFACES

Siddhesh Narayan Dalvi

Dissertation

Approved:

Accepted:

Advisor
Dr. Ali Dhinojwala

Department Chair
Dr. Tianbo Liu

Committee Member
Dr. Tevis DB Jacobs

Dean of the College
Dr. Ali Dhinojwala

Committee Member
Dr. Jutta Luettmmer-Strathmann

Acting Dean of the Graduate School
Dr. Marnie Saunders

Committee Member
Dr. Mesfin Tsigie

Date

Committee Member
Dr. Hunter King

ABSTRACT

Understanding the mechanism of adhesion and friction in soft materials is critical to the fields of transportation (tires, wiper blades, seals etc.), prosthetics and soft robotics. Most surfaces are inherently rough and the interfacial area between two contacting bodies depends largely on the material properties and surface topography of the contacting bodies. Johnson, Kendall and Roberts (JKR) derived an equilibrium energy balance for the behavior of smooth elastic spherical bodies in adhesive contact that predicts a thermodynamic work of adhesion for two surfaces in contact. The JKR equation gives a reversible work of adhesion value during approach and retraction. However, viscoelastic dissipation, surface roughness and chemical bonding result in different work of adhesion values for approach and retraction. This discrepancy is termed adhesion hysteresis. Roughness is undermined as a cause of hysteresis in adhesion studies.

Recently, a continuum mechanics model has been developed that predicts the work of adhesion on rough surfaces with known roughness in the form of power spectral density (PSD) function. To test the above mentioned theoretical model, we have conducted JKR experiments between highly cross-linked smooth polydimethylsiloxane (PDMS) of four different elastic moduli and diamond surfaces of four different crystal sizes and roughness. The rough diamond surfaces are characterized for topography using stylus profilometry, atomic force microscopy and

in-situ transmission electron microscopy combined to give a comprehensive PSD. Results suggest that the observed work of adhesion during approach is equivalent to energy required to stretch the PDMS network at the surface and in the bulk to form the real rough contact area. However, in retraction work of adhesion is found to be proportional to the ratio of excess energy spent in the loading-unloading cycle and the true contact area obtained from topography indicating conformal contact matching fracture mechanics behavior. Thus, the study resolves adhesion hysteresis discrepancy on rough surfaces.

It is known that adhesion hysteresis increases interfacial friction on rough surfaces. However, an experimentally proven quantitative model is still missing. Previous studies on smooth surfaces have shown that shear stress increases with velocity initially, reaching a maximum and then either plateaus out or decreases depending upon the modulus of the sliding elastomer. We have performed shear measurements with velocities ranging from nm/sec to cm/sec between PDMS elastomers and diamond surfaces. Data suggests higher shear stresses at lower velocities for rough surfaces and thus a shift for the peak previously observed on smooth surfaces. Additionally, there are states such as steady-state sliding, stick-slip and detachment waves with increasing stress in the same order. These states are found to occur at a critical stress and their onset is linearly proportional to the elastic modulus of the sliding rubber. The stress predictions using existing theories do not decouple adhesion and deformation energy losses during friction observed experimentally on rough surfaces and further investigation is required in order to obtain a better friction model.

ACKNOWLEDGEMENTS

At first, I would like to take this opportunity to thank my family, my parents Maya and Narayan Dalvi, my sister Neha Dalvi, who have been a constant emotional support. It is for them that I believed in myself and was motivated to do this noble deed.

I will be forever grateful to my advisor Dr. Ali Dhinojwala for his incessant guidance and training which had not only helped me develop my personality as a scientist but also made me a better human. Sometimes, the easiest solution to a problem is one human interaction away and that is what comes to my mind when I think of my advisor. It is his philosophy of individual freedom and learning to lift yourself up every time you are made to bite the dust that has kept me highly motivated throughout the five years of my doctoral studies.

I would like to thank all my committee members Dr. Mesfin Tsige, Dr. Andrey Dobrynin, Dr. Hunter King and Dr. Tevis D.B. Jacobs for their constant guidance and support beyond laboratory and classrooms. I would also like to thank Dr. Younjin Min for being a part of my committee during my Formal Seminar and Research Presentation. Special thanks to Dr. Jacobs for collaborating with us on this project without which this work is unimaginable and so is my Ph. D. With all due credit to Dr. Jacobs's student, Abhijeet Gujrati, for characterizing surfaces used in this work and running the MATLAB code for predictions. Abhijeet has

always been a good friend. I would also like to thank Dr. Lars Pastewka for his invaluable contributions and inputs throughout our collaborative work.

As far as my research group is concerned, both past and present members, they are the best people I have interacted with in my life. May it be few hours long intellectual conversations or seconds of small talks, it was always fun with my colleagues. Many spoken and unspoken ideas emerged while talking to them and those are the ones that have indirectly helped me maneuver my way through tough situations. I would like to thank Sukhmanjot Kaur, Nityanshu Kumar, Amal Narayanan, Michael Wilson, Saranshu Singla, Anvay Patil, Mario Eccheveri, Kzin Htut and others. I greatly appreciate Daniel Maksuta for his help in later stage of my Ph. D. journey in analyzing my data and having deep philosophical conversations. I would also like to thank Dr. Adrian Defante for teaching me contact angle measurement and basics of surface science that has tremendously helped in building my fundamental understanding right. I also thank past Ph. D. students who were always open to listen to my thoughts especially Dr. Nishad Dhopatkar, Dr. Emmanuel Anim-Danso, Dr. Pushkar Sathe, Alankar Rastogi, Dr. Parker(He) Zhu, Dr. Mena Klittich, Dr. Ming Xiao, Dr. Yang Zhou and Dr. Yu Zhang.

Apart from my group members, there have been so many intelligent and interesting people I've met at Akron that I might not remember them enough to mention here. I would like to appreciate Dr. Zhorro Nikolov's help in training me for XPS, Auger Electron Spectroscopy and Ellipsometry for my early research work. I would like to thank Dr. Meysam Hashemnejad and Dr. Jiansheng Feng for help in rheology and AFM.

I have had a tough time at Akron outside the university premises at a personal level but I had a good time with my roommates at different points of time, Tanmay Jain and Dr. Alex Kleinfehn. My friends have made my life easier and given me moral support outside lab. Ashish Bandekar and Aditya Jindal were the people responsible for keeping me settled when I landed on United States soils for the first time. Ajinkya Deshmukh, Harshal Gade, Sagar Bangar, Abhishek Panchal and Shrish Patel have been my goto people whenever in trouble.

Last but not at all the least, I'm very thankful to the supreme God who has given me the strength and intellect to carry out this incredible task and blessed me with success and privilege not bestowed upon many. Yet, I promise to be grounded and keep working with minimal expectations for the life I've been given and for the betterment of future of the Universe.

TABLE OF CONTENTS

	Page
LIST OF TABLES	x
LIST OF FIGURES	xvii
CHAPTER	
I. INTRODUCTION	1
II. BACKGROUND	5
2.1 ROUGHNESS	6
2.2 SURFACE FORCES	13
2.3 WORK OF ADHESION (THERMODYNAMICS)	17
2.4 CLASSICAL CONTACT/FRACTURE MECHANICS	20
2.5 FRICTION	45
III. EXPERIMENTAL	64
3.1 WATER CONTACT ANGLE	64
3.2 FABRICATION OF SELF-ASSEMBLED MONOLAYERS	65
3.3 FABRICATION OF ROUGH DIAMOND SURFACES	65
3.4 FABRICATION OF SOFT ELASTIC POLYDIMETHYL- SILOXANE (PDMS)	66
3.5 DYNAMIC MECHANICAL ANALYSIS OF CROSS- LINKED PDMS	67
3.6 SURFACE TOPOGRAPHY CHARACTERIZATION	68

3.7 CONTACT ANGLE AND CONTACT ANGLE HYSTERESIS OF NANODIAMOND	78
3.8 ADHESION MEASUREMENTS USING JKR-BASED SETUP	79
3.9 FRICTION MEASUREMENTS USING CANTILEVER SETUP	81
IV. LINKING ENERGY LOSS IN SOFT ADHESION TO SURFACE ROUGHNESS	83
V. SHEAR BEHAVIOR OF ELASTOMER SLIDING ON ROUGH SURFACES	96
5.1 Introduction	96
5.2 Experimental	99
5.3 Results	100
5.4 Discussion	110
5.5 Summary	112
VI. CONCLUSIONS	114
REFERENCES	117

LIST OF TABLES

Table	Page
3.1 Roughness parameters (2D) of the nanodiamond substrates	75
3.2 PDMS-OTS contact with JKR Analysis for four different moduli . . .	81
4.1 Comparison of different work of adhesion values for nanodiamond substrates	94

LIST OF FIGURES

Figure	Page
2.1	Definition of the arithmetic average height (R_a)[1]. 8
2.2	shows that scalar measurement of root-mean-square height is identical for A. two superposed sine waves (hierarchical roughness) and B. a frozen capillary wave (random roughness) however, their power spectral density functions are different[2]. 10
2.3	A. Koch Snowflake of dimension $D=1.26$; B. Romanesco Broccoli [3]. 11
2.4	PSD when surface is self-affine for $q_0 < q < q_1$ where, q_0 and q_1 are the long-distance and short-distance roll-off wave-vectors respectively, that are determined by the limits of measuring instrument. While the smallest possible wave-vector q_L depends upon the maximum lateral dimension of measurement. 12
2.5	Typical van der Waals interaction energy (or potential) function $w(r)$ and force function $F(r)$ between two atoms, which are related by $F(r) = -dw/dr$. The plotted curves are for a Lennard-Jones potential with parameters $A = 10^{-77} J/m^6$ and $B = 10^{-134} J/m^{12}$ [4]. 14
2.6	Van der Waals interaction energy W and force F between macroscopic bodies of different geometries in terms of their Hamaker Constant, A . Negative F implies attraction (A positive); positive F means repulsion (A negative). The Hamaker constant A is defined as $A = \pi C \rho_1 \rho_2$ where ρ_1 and ρ_2 are the number of atoms per unit volume in the two bodies and C is the coefficient in the atom-atom pair potential (top row) [4]. 16
2.7	Bulk and surface dipoles depicted to show cancellation of dipoles at the interface of a gas (G) and a liquid (L)[5]. 17

2.8	(a) Dependence of the normalized surface stress on strain for large deformations. (b) Universal dependence of the normalized surface stress on the ratio λ/λ_{max} . Inset: relative change of the normalized surface stress as a function of the relative change of the bond energy. $E_b(\lambda)$ is the bond energy in the film at different deformation ratios, and $E_{b,0}$ is the bond energy in the undeformed film. Data are shown for films of polymer networks with average numbers of cross-links per chain n_{cr} and initial film thicknesses h_0 : 6.25 and 60.3σ (purple circles); 10.42 and 59.6σ (blue triangles); 13.54 and 59.2σ (green left triangles); 16.67 and 58.9σ (yellow right triangles) [6]	21
2.9	The difference in contact area for Hertz (dashed line) and JKR (bold line) show that only compressive stresses exist in an Hertzian contact while there is compression at the center and tension at the contact line for JKR contact.	23
2.10	Adhesion hysteresis compared for PDMS hemisphere in contact with A. an alkylsilane and B. fluoroalkylsilane monolayer deposited on a flat mica substrate, the solid lines are the fits using JKR model (eq. 2.25). The work of adhesion obtained for loading and unloading are different for both PDMS-substrate combinations, where in case of alkylsilane the difference is less and within error bars, while the difference is significant for fluorosilane monolayer [7].	25
2.11	The increase in contact area due to irreversible processes	25
2.12	Stresses around a crack tip for a tensile type loading [8].	30
2.13	The three fracture modes A. Cleavage mode: model I, B. In-plane shear mode: mode II, C. antiplane shear mode: mode III [9].	30
2.14	Vicinity of a crack tip describing dissipated or plastic zone (Irwin's model)[10].	31
2.15	Schematic of a weakly cross-linked and entangle pressure-sensitive adhesive and a crosslinked rubber [10]	32
2.16	A simplistic view of rough surfaces as assumed by Dahlquist for developing PSAs	32
2.17	Comparison of roughness models assumed in development of different theories [11].	35
2.18	depicts the contact on a self-affine surface where at each magnification a different real area of contact can be imagined [12].	36
2.19	A. shows the state of conformal contact between rubber continuum and hard rough surface, B. shows deformation at a single asperity contact [13]	37

2.20	Relative pull-off force for smooth rubber spheres in contact with a flat Perspex surface as a function of the roughness of Perspex. Effects of modulus, E , of the rubber: curve I, $2.4 \times 10^6 \text{ N m}^{-2}$; curve II, $6.8 \times 10^5 \text{ N m}^{-2}$; curve III, $2.2 \times 10^5 \text{ N m}^{-2}$ [14].	41
2.21	Relative adhesion energies calculated from pull-off for a smooth rubber surface in contact with a Perspex surface as a function of the roughness, using a crossed cylinder configuration. \bigcirc RTV 602 ($E = 487 \text{ kPa}$) Δ Dow Corning XF-13-523 ($E = 63 \text{ kPa}$) [15].	42
2.22	$50 \times 50 \mu\text{m}$ AFM scans of sand blasted glass surfaces along with their Power Spectral Density functions.	44
2.23	The effective adhesion energy as a function of RMS roughness for 7 different rough glass surfaces. Blue curve is the theoretical predictions, green curve (a) is experimental pull-off at $0.2 \mu\text{m}/\text{sec}$ and red curve (b) is at $2 \mu\text{m}/\text{sec}$	44
2.24	A. Schematic of Load versus Displacement (P-h) curve as per JKR theory. The pull-in (i - > ii) and pull-off (iii - > iv) instabilities are marked with the corresponding configurations. A complete contact cycle includes the loading (red arrows) and unloading (blue arrows) phases. The size of the hysteresis loop formed in the contact cycle due to the elastic instabilities denotes the hysteretic energy loss ΔE_i . B. Experiment with rough surfaces showing a P-h curve with a large hysteresis loop that is load- or depth-dependent[16].	45
2.25	A. As the load or depth increases the energy lost due to hysteresis for an AFM glass bead in contact with rough PDMS surface increases. B. Energy lost plotted as a function of RMS roughness of the elastic half-space [16].	46
2.26	Stribeck curve with three different regimes for friction with lubrication[17, 18].	49
2.27	Coefficient of friction as a function of load. Full lines are the theoretical predictions. The dotted line is experimental points for hard rubber [19].	51
2.28	Coefficient of friction as function of the sliding velocity at various temperatures of the natural rubber on clean silicon carbide. Curves are shown in two groups for clarity. The symbols denote different temperatures ranging from -60C to 90C	53
2.29	A. The mastercurve of all the curves superposed from Fig. 2.28 using time-temperature superposition principle to give coefficient of friction for natural rubber B. Master curves for the coefficient of friction of natural rubber on the three surfaces, - - - wavy glass, — clean silicon carbide, - . . - dusted silicon carbide; all curves referred to 20 C	54

2.30	Master curves of the coefficient of friction of rubbers B, C, D and E on glass referred to their respective T_g temperature. Below: Loss modulus curves E'' as function of frequency for the four rubbers referred to their respective T_s temperatures. Velocity and frequency have been displaced with respect to each other by $\log_{10}\lambda = 6.2$., - . - . - B styrene butadiene; — C acrylonitrile butadiene; - - - D butyl rubber, - . - . - E natural rubber	55
2.31	Contact between natural rubber and perspex track, $v=0.23$ c/s. Single frame of a film of the contact between perspex and a butyl sphere sliding over it at 0.043 c/s.	57
2.32	A cosine roughness profile with the wave vector A along, and B perpendicular to the sliding direction. Only in case A will the surface roughness generate time-dependent (fluctuating) deformations of the rubber block.	58
2.33	The kinetic friction coefficient as a function of the logarithm of the sliding velocity. The solid and dashed curves are with and without flash temperature effects, respectively.	59
2.34	The kinetic friction coefficient for rubber sliding on a carborundum surface under different conditions [20]. Experimental results for a rubber block sliding on dry clean ~dashed line, dusted ~dashed?dotted, and wet ~solid line carborundum stone surfaces. . .	60
2.35	Extended correlations of hysteresis and adhesion friction under wet and dry conditions for carbon black filled Solution-Styrene Butadiene Rubber on rough granite [21].	61
2.36	Time record of the deceleration of a car in a locked wheel braking experiment.	62
3.1	Casting procedure for elastic PDMS lenses inspired by works in refs. [22–24].	68
3.2	Stylus profilometry of the polished UNCD (A), UNCD (B), NCD (C) and MCD (D).	70
3.3	Power spectral densities of the four surfaces, with indication of the specific regimes of applicability of each technique. The present figure uses line style (solid, dashed, dotted) to indicate the specific bandwidth over which different techniques were applied. Because of the nature of tip artifacts, the minimum size from stylus and AFM data differ between surfaces.	74
3.4	2D power spectral densities, after conversion from the 1D values . . .	74

3.5	Plot of the correction $g(h'_{rms})$ to the small-slope approximation. For values of $g(h'_{rms}) \approx 1$ the small slope approximation is valid (A) Validation of Eq. 3.13 using computer-generated self-affine surfaces with varying RMS slope h'_{rms} and Hurst exponents H (B) The solid line shows the analytic result given by Eq. 3.13.	77
3.6	A. The comparison of static and advancing and receding angles for the smooth OTS coated silicon wafer and nanodiamond surfaces. As the roughness increases there is a decrease in static angle while the difference in advancing and receding is increased. B. shows the difference plotted as contact angle hysteresis (CAH) as a function of RMS slope for the surfaces.	78
3.7	Schematic of the JKR apparatus.	80
3.8	Schematic of the home built setup for measuring friction (A) showing simultaneous capture of friction force (from spring deflection and known spring constant) and contact area (from high speed camera). The frames analyzed through deflection tracking and edge detection are plotted as a function of time (B) were the raw data gives the apparent shear stress from force/area.	82
4.1	The contact radius data for the PDMS hemispheres on the OTS surface show low hysteresis between loading (empty symbols) and unloading (filled symbols). The dashed lines indicate JKR model fits for loading and solid lines indicate the JKR model fits for unloading.	84
4.2	Comprehensive topography characterization for four rough nanodiamond surfaces. The surface topography was measured using a multi-resolution approach that combines transmission electron microscopy (rightmost region of the curves), atomic force microscopy (intermediate region), and stylus profilometry (leftmost region). The nanodiamond surfaces are designated using the following nomenclature: ultrananocrystalline diamond (UNCD) is shown in red; nanocrystalline diamond (NCD) in black; microcrystalline diamond (MCD) in green, and a polished form of UNCD (polished UNCD) in blue. AFM images (of 5-micron lateral size) are shown in the left inset; TEM images are shown in the right inset. More than 50 measurements for each surface are combined using the power spectral density, which reveals the contribution to overall roughness from different length scales (wavelengths). These comprehensive descriptions of surface topography enable the determination of true surface area and stored mechanical energy due to the topography, which are necessary to understand adhesion.	85

4.3	Contact radius was measured as a function of applied force plots for PDMS spheres with elastic modulus of 0.7 MPa (A), 1 MPa (B), 1.9 MPa (C), and 10 MPa (D). The loading data are represented using hollow symbols and are fit using Eq. 1 (dashed line) to extract the apparent work of adhesion W_{app} . The separation data are represented using filled symbols; a subset of the data are fit using Eq. S1 (solid line) to extract $W_{app,ret}$	86
4.4	During adhesion, the materials go from the initial state (left) to the final state (right). However, to fully account for the energy change, one must consider the change in area of the soft material, which is represented schematically by including the intermediate state (middle).	87
4.5	Adhesion measurements during approach and retraction. Loading and adhesion tests were performed with ultra-smooth PDMS hemispheres of varying stiffness from 0.7 to 10 MPa. Representative curves from one material (with $E=1.9$ MPa) are presented in this figure. The load-dependent contact radius (A) was measured using in situ optical microscopy. The apparent work of adhesion upon approach W_{app} was extracted by fitting the loading data (hollow points) using the JKR model (dashed lines). The force-displacement curves (B) were used to calculate the energy loss E_{loss} during contact by performing a closed-circuit integral (inset). Both approach and retraction experiments were conducted at a very low speed, 60 nm/s.	88
4.6	The experimental measurements of W_{app} can be compared against the unmodified Persson-Tosatti model, which does not account for the change in area of the soft elastomer.	92
4.7	Comparison of work of adhesion and energy loss with the proposed model of conformal contact. Experimental measurements of apparent work of adhesion during approach (A) are well-fit using the balance of adhesive and elastic energy described in the Eqs. 4.6 to 4.8; here the solid line represents $y = x$. In panel B, the energy loss is plotted as a function of true contact area (Eq. 4.8). The solid line is a linear fit to the data and has a slope of 46.1 ± 7.8 mJ/m ² ($R^2 = 0.8$).	93
5.1	Real shear stress observed by averaging the maxima obtained from the stress curves as a function of modulus and sliding velocity. The solid lines are the Gaussian fitting functions to the shear stress curves as a function of velocity, similar to eq. 1 showing maxima at a particular velocity independent of elastic modulus. However, as the modulus increases the shear stress increases proportionally.	101

5.2	The plot of shear stress curves as a function of time for 0.7 MPa PDMS on OTS surface at three different velocities showing three different states of steady state sliding (2.6 mm/sec), periodic stick-slip (0.17 mm/sec) and Schallamach wave behavior (3 $\mu\text{m}/\text{sec}$).	102
5.3	Depicts the three states through the contact area images captured before and after sliding on a rough UNCD surface wherein the detachment wave is visible in C. The different contact area changes during sliding along with the stress variations (through colors) are depicted qualitatively in the side view schematics drawn on the right-hand-side. The stresses increase according to the order of colors- blue, green, yellow, orange, red.	103
5.4	Comparative plot for the maximum shear stresses as a function of velocity between PDMS hemisphere and the rigid surfaces of smooth OTS monolayer and rough diamond surfaces i.e. UNCD and Polished UNCD for 0.7 MPa (A), 1 MPa (B) and 1.9 MPa (C). The different symbol types show distinction in moduli and frictional states.	104
5.5	The increasing trend of critical stresses for the instabilities (stick-slip in red and detachment waves in blue) as a function of modulus for all the surfaces showing there is a critical stress irrespective of roughness. The solid lines are a guide to the eye.	105
5.6	DMA temperature sweep plots for the 0.7 (A), 1 (B) and 1.9 MPa (C) PDMS sheets showing complex elastic, storage and loss moduli. The range of temperatures (-130 to 130 C) translates to the range of frequencies required for friction model.	107
5.7	TTS plots for the 0.7, 1 and 1.9 MPa sheets showing complex elastic modulus and loss modulus for 15 orders of frequencies. The spline function for the loss moduli were used to predict the second term in eq. 5.5.	108
5.8	Predictions for frictional stress on rough surfaces as a function of velocity as compared to the experimental observations.	109

CHAPTER I

INTRODUCTION

Polymers in the form of elastomers are used in a humungous quantity as adhesives, seals, tires, dental prosthetics, stents, coatings etc. where they are desirable since their mechanical properties can be tuned easily depending upon the type of contact required. It is intuitive that in ambient conditions, how they interact with a given surface is not governed by just the polymer surface composition but also their ability to flow and resist deformation i.e. their visco-elasticity. It is this structure-property relationship that makes polymers behave differently than other materials. Hence, it is very crucial to understand physical mechanisms and relate them to macromolecular properties before we develop technologies to manufacture and apply polymers.

Surface adhesive interactions are a consequence of attractive intermolecular forces and, for a flat surface, can be characterized using thermodynamic parameters such as surface energy and work of adhesion. However, surface topography plays a very strong role in modifying the apparent work of adhesion between two surfaces. For two hard materials in contact, peaks and valleys on a surface will increase the average separation between the surfaces and thus reduce the overall surface adhesion [25, 26]. For a soft material on a hard substrate, the effect of surface roughness is more complex; a roughness-induced increase in real contact area can increase the overall adhesion, but the strain required for the soft material

to conform to the rough substrate causes an energy penalty that can reduce overall adhesion[27]. At the same time, millions of years of evolution has enabled living beings to adhere and climb difficult terrains with the help of soft pads[28]. Design parameters such as hierarchical nanostructures and material properties such as effective modulus have been optimized to overcome the problem of adhesive contact on rough surfaces. Yet mimicking and taking advantage of bio-inspired designs for their reversibility and adaptability on surfaces have limitations[29–33]. Recent progress in transfer printing technology, soft robotics and haptics have shown requirement of theoretical basis and explanation for observed adhesion on rough surfaces where nano-scale metrics matter the most[34–36].

Our understanding of adhesive contact between soft elastic materials was elegantly resolved in a seminal paper in 1971, where Johnson, Kendall, and Roberts (JKR) showed that the contact area under applied load is larger than predicted by the classic Hertz model[37, 38]. However, the presence of surface roughness significantly alters the contact behavior. As a rough contact is loaded, it obeys the trends of the JKR model, but the measured apparent work of adhesion W_{app} is significantly lower than the intrinsic value W_{int} ; the latter is a thermodynamic parameter that depends on intermolecular interactions between the materials[4]. Upon retraction, adhesion hysteresis is observed on rough surfaces, where the behavior deviates significantly from that of loading and from the JKR predictions. If the JKR formalism is applied, one calculates a work of adhesion (for retraction) that is much larger than W_{int} and may not have thermodynamic significance[14, 15, 39–41].

Even though all practical surfaces are rough, quantifying the loss of adhesion due to roughness has remained a challenge. Surface roughness exists over many length scales, including down to the atomic scale, and is not easily measured using conventional techniques (such as profilometry or atomic force microscopy) nor described by conventional metrics (such as root-mean-square roughness or the standard deviation of asperity heights)[42, 43]. Persson has developed a set of continuum mechanics models to describe soft-material adhesion at rough contacts as a function of the power spectral density (PSD)[13, 44, 45]. The PSD, C is a mathematical tool for separating contributions to topography from different length scales λ , and is commonly represented as a function of wavevector $q=2\pi/\lambda$. However, there is only limited experimental validation of these theories, due primarily to the difficulty of characterizing the smallest-scale topography, which has been shown to be critically important for contact and adhesion.

The understanding of adhesion hysteresis during retraction is even less developed. The increase in adhesion energy upon retraction is often attributed (sometimes without evidence) to velocity-dependent dissipation of energy due to bulk viscoelasticity[23, 46, 47]. However, roughness-induced adhesion hysteresis is still observed even for systems that show no evidence of viscoelasticity on smooth surfaces[48, 49]. Furthermore, it is not clear whether a meaningful work of adhesion can be computed by applying equilibrium-based theoretical models (such as JKR for smooth surfaces or Persson's model for rough surfaces) to the non-equilibrium separation behavior[50, 51]. In addition to roughness and viscoelasticity, adhesion hysteresis is also observed as a result of interfacial bonding (for example, PDMS in contact with silica surfaces)[52, 53]. Thus, our current

understanding of adhesion hysteresis is incomplete. In chapter 4, we investigate the origins of energy loss in order to demonstrate the fundamental contribution of surface roughness.

A major area of exploration with respect to application of continuum mechanics is tribology dealing with sliding of surfaces against each other. Whether the established laws related to friction are applicable universally or not remains a debated topic [54, 55]. Rubber friction has been identified as a velocity-dependent viscoelastic process with relaxation mechanisms including steady sliding, stick-slip or detachment waves [56, 57]. Furthermore, it is known that adhesion hysteresis increases interfacial friction on rough surfaces. Previous studies on smooth surfaces have shown that shear stress increases with velocity initially, reaches a maximum, and then either plateaus or decreases depending upon the modulus of the sliding elastomer[23, 58]. However, an experimentally validated quantitative model that incorporates surface roughness is still lacking.

In chapter 5, we have performed friction measurements with sliding velocities ranging from nm/sec to m/sec between PDMS hemispheres and rough surfaces using a home-built setup with a microscope simultaneously observing the changes in contact area during sliding. All the three state transitions are seen on rough surfaces where the onset of stick-slip and Schallamach waves is at far lower velocities (5 orders lower) as compared to smooth surfaces. Thus, roughness acts as a shear stress or adhesion promoter. Furthermore, predicting such stress behavior might be an exercise for future work.

CHAPTER II

BACKGROUND

In this chapter, a detailed overview of roughness, adhesion and friction will provide the necessary foundation for the following chapters. Along with certain terminologies and definitions most mathematical symbols used here would have similar significance in the rest of the dissertation. The background should also help in giving a historical perspective to the topic. The first definition concerned is that of a surface or an interface, where the question of "what exactly is a surface?" has been intriguing and a topic of debate for centuries. In this study, we would define surface as the superficial boundary of a bulk phase surrounded by vacuum or air. An interface would be a common boundary of two surfaces in direct contact. From the perspective of contact mechanics, contribution of bulk to changes in adhesion, friction and wetting can be simply predicted by knowing the material properties[56, 59, 60]. However, the surface contribution is much more complicated and requires information of chemical bonding or heterogeneity for e.g. through spectroscopy [61], inter-digitation or inter-diffusion and surface roughness through microscopy or interferometry [14, 39]. Our focus in the following studies is the effect of roughness or surface topography on interfacial phenomena.

2.1 ROUGHNESS

For the development of scientific theories related to engineering, geophysics, biology, cavitation, catalysis and most other disciplines, the early stages have always thought of ideal conditions neglecting a very crucial physical aspect of surfaces in use, the inherent roughness [62, 63]. Since antiquity humans have thought about roughness to understand the physical world. Many of the earlier known civilizations have used friction and adhesion between rough surfaces to grind food-grains, to carry stone blocks uphill and other mechanical works that made life easier. Perhaps Leonardo da Vinci was the first scientist who made observations that surface roughness has an impact on how easy it is to slide different objects and thus began the field of tribology [64]. At that time, microscopy was in its nascent stage and the ability of human eyes is only about 50-60 μm resolution as far as length scales are concerned. Only in modern times with the advent of electron microscopy and atomic force microscopy (AFM) have we been able to measure asperities in length scales lower than few microns. Thus, what appears as a smooth surface could be extremely rough at smaller length-scales. Thus, surface metrology becomes crucial and today's technological advancements enable one to push limits of measuring topography from meters to Ångströms. Nonetheless, it is important to first look at the developed methodologies that have been used to quantify surface roughness using statistical variables.

2.1.1 SURFACE ROUGHNESS MEASUREMENT PARAMETERS

Essentially, there are two different ways surface roughness or topography can be measured, through line profile or areal profile. Line profile is a one-

dimensional scan that measures heights of asperities, while an areal profile is the two-dimensional map of the entire surface. Thus, there are two different types of roughness parameters obtained from the above techniques categorized according to ISO and ASTM definitions. The most basic surface roughness parameter especially in metal finishing for quality check is the arithmetic average R_a also known as centre line average l_a which is the absolute deviation from the mean reference line as shown in Fig. 2.1 ('y' is the deviation at position 'x'). The mathematical and numerical definitions for R_a are:

$$R_a = \frac{1}{l} \int_0^l |y(x)| dx, \quad (2.1)$$

$$R_a = \frac{1}{n} \sum_{i=1}^n |y_i|, \quad (2.2)$$

The most widely used and recognized parameter is the root-mean-square (RMS) height that is defined as the standard deviation of the distribution of heights of the surface asperities. Statistically, RMS height is more sensitive than R_a to larger deviations from the mean and is calculated by the following expressions:

$$h_{rms} = \sqrt{\frac{1}{l} \int_0^l y(x)^2 dx}, \quad (2.3)$$

$$h_{rms} = \sqrt{\frac{1}{n} \sum_{i=1}^n y_i^2}, \quad (2.4)$$

The mean line for RMS is the dividing line for the profile so that the sum of the squares of the deviations of the profile heights is equal to zero. There are

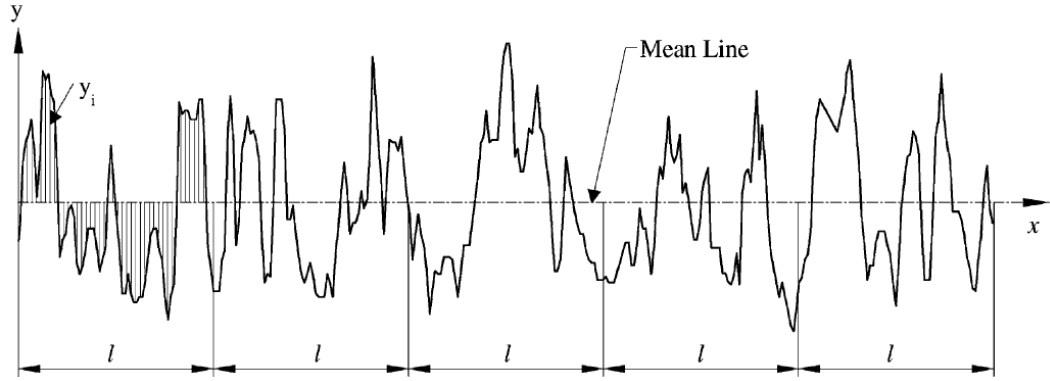


Figure 2.1: Definition of the arithmetic average height (R_a)[1].

other parameters which also deal with measuring the peaks and valleys such as skewness and kurtosis along with autocorrelation function and correlation length that are derived from height probability distribution functions. However, all the single roughness parameters can lead to representation of whole of a surface with one particular height or spacing and can lead to wrong interpretation based on the statistical measure used.

A more complex parameter used in tribology, elastic contact and fatigue crack initiation is the RMS Slope of the profile (Δ_q or ∇h) which is a combination of both height or amplitude and spacing. It signifies the correlation between asperity height and spacing (can also be thought of as amplitude and wavelength). The mathematical (eq. 2.5) and numerical (eq. 2.6) relations used to calculate RMS Slope are:

$$\Delta_q = \sqrt{\frac{1}{L} \int_0^L (\theta(x) - \dot{\theta})^2 dx}, \dot{\theta} = \frac{1}{L} \int_0^L \theta(x) dx \quad (2.5)$$

where $\theta(x) = \left| \frac{dy}{dx} \right|$ is the value of slope at point (x, y) .

$$\Delta_q = \sqrt{\frac{1}{n-1} \sum_{i=1}^{n-1} \left(\frac{\delta_{y_i}}{\delta_{x_i}} - \theta_m \right)^2}, \theta_m = \frac{1}{n-1} \sum_{i=1}^{n-1} \left(\frac{y_i - y_{i-1}}{x_i - x_{i-1}} \right) \quad (2.6)$$

RMS Curvature is another hybrid parameter that measures the root-mean-squared average of radii of curvature of the asperities.

2.1.2 POWER SPECTRAL DENSITY

Similar to roughness parameter, a Power Spectral Density (PSD) function is a mathematical depiction of a rough surface, however, a PSD divides a surface into sine-waves of numerous wavelengths and amplitudes. Thus, it gives information about the topography at multiple length-scales giving a complete understanding of a surface. The Fig. 2.2 below is an accurate exhibition of the power of PSD function.

A surface roughness power spectrum or PSD, $C(q)$ is mathematically written as,

$$C(q) = \frac{1}{(2\pi)^2} \int d^2x \langle h(x)h(0) \rangle e^{-iq \cdot x} \quad (2.7)$$

Here, $x = (x, y)$ and $z = h(x)$ is the substrate height measured from the average surface plane, defined so that $\langle h \rangle = 0$. The $\langle \dots \rangle$ stands for ensemble averaging, i.e., averaging over a collection of different spots on the surface with identical statistical properties. The assumption is that the statistical properties of the substrate are translationally invariant, so that the correlation

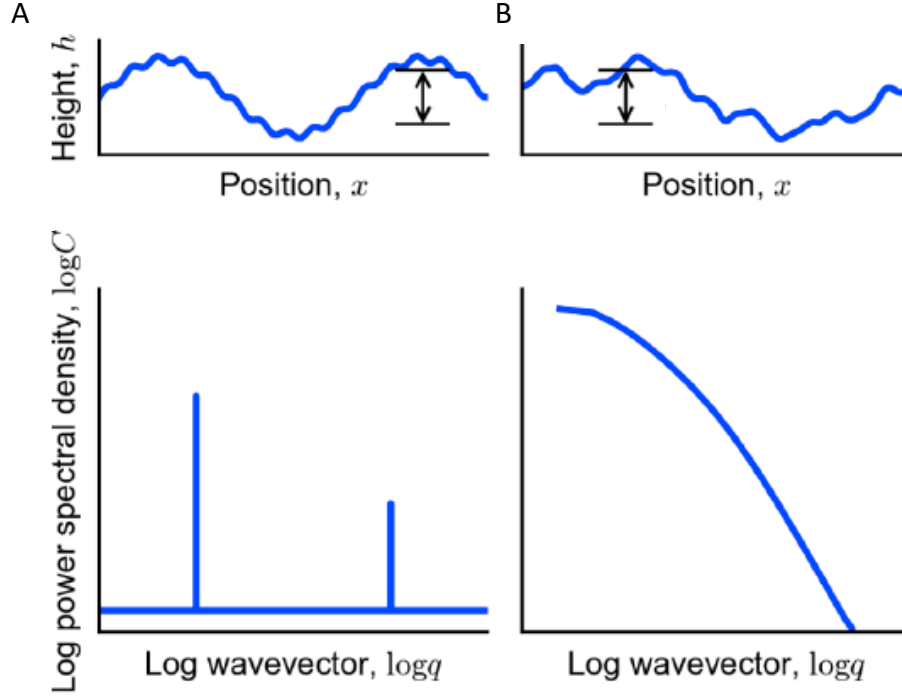


Figure 2.2: shows that scalar measurement of root-mean-square height is identical for A. two superposed sine waves (hierarchical roughness) and B. a frozen capillary wave (random roughness) however, their power spectral density functions are different[2].

$\langle h(x+x_0)h(x_0) \rangle$ does not depend on the choice of x_0 , but only on the in-plane distance vector x . q is the wave vector where $q = 2\pi/\lambda$.

The RMS surface roughness parameters discussed earlier (2.1.1) can be represented as moments of the PSD. For e.g., RMS height (h_{rms}), slope (h'_{rms}) and curvature (h''_{rms}) are the first, third and fifth moment :

$$h_{rms} = \sqrt{\frac{1}{\pi} \int_{q_0}^{q_1} qC(q) dq}, \quad (2.8)$$

$$h'_{rms} = \sqrt{\frac{1}{\pi} \int_{q_0}^{q_1} q^3 C(q) dq}, \quad (2.9)$$

$$h''_{rms} = \sqrt{\frac{1}{\pi} \int_{q_0}^{q_1} q^5 C(q) dq}, \quad (2.10)$$

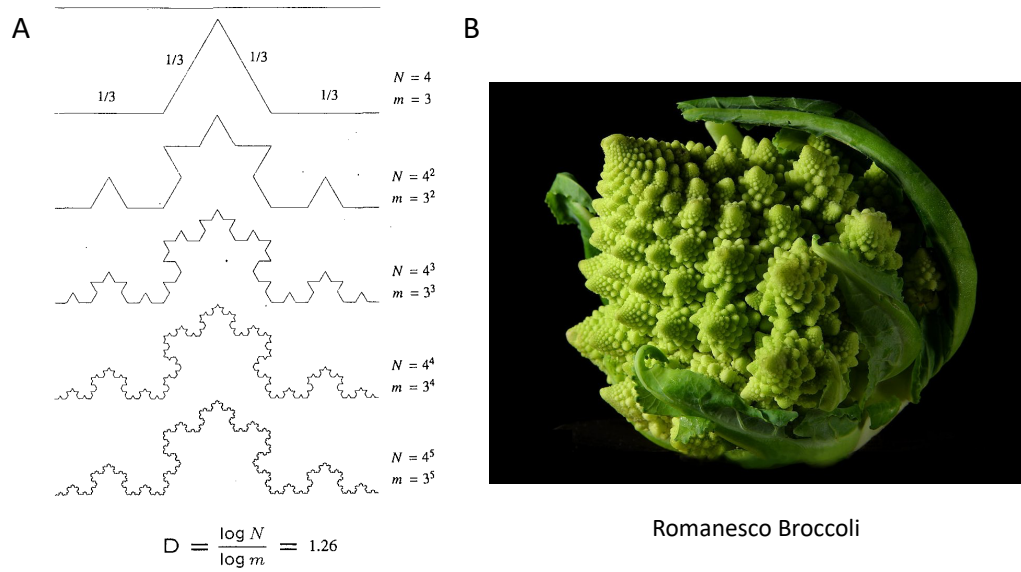


Figure 2.3: A. Koch Snowflake of dimension $D=1.26$; B. Romanesco Broccoli [3].

2.1.3 FRACTAL

Any random or chaotic process leads to some form of pattern and regularity which is very difficult to distinguish at first, for e.g. particles diffusing through Brownian motion. Similarly, in nature, nucleation results from an instability or defect and forms geometrical patterns that lead to shapes such as a snow-flake from ice nucleation. A fractured surface is also a result of crack propagation which was nucleated from a defect in the solid. Formation of what looked like an irregular surface from fracture was known as "fractal", coined by Benoit Mandelbrot at IBM Inc., who is responsible for the development of "theory of self-similarity and roughness" [65]. He defines fractal as a shape made up of "parts similar to the whole in some way". This shows a feature of self-similarity or self-affinity wherein shapes are recursive in different dimensions and magnifications e.g. a Koch snow-flake or Romanesco Broccoli shown in Fig. 2.3b[3, 66].

Let us consider a rough surface and represent it along number of positions in a plane such that $z = h(x, y)$ where 'z' represents the height of asperities. Then

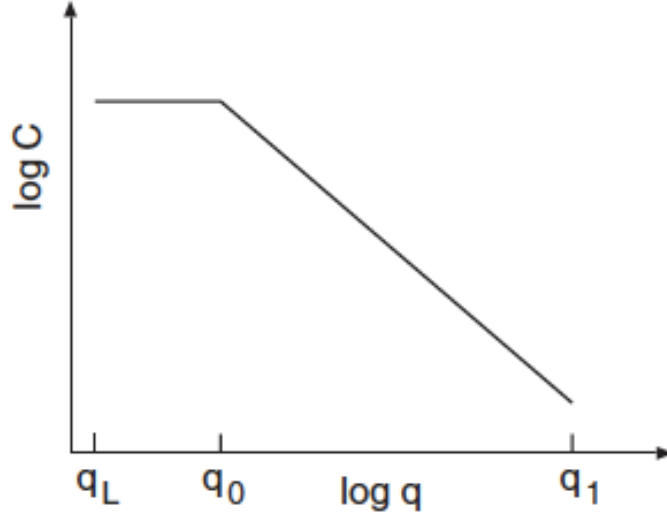


Figure 2.4: PSD when surface is self-affine for $q_0 < q < q_1$ where, q_0 and q_1 are the long-distance and short-distance roll-off wave-vectors respectively, that are determined by the limits of measuring instrument. While the smallest possible wave-vector q_L depends upon the maximum lateral dimension of measurement.

a self-similar surface and a self-affine surface are analogous except for the fact that a self-similar surface when magnified in any dimension appears the same. While in case of self-affine surfaces the magnification factor along z-direction is different from the in-pane magnification factor such that the Hurst exponent, H defines the scaling/magnification factor λ^H along the z-direction for recovering the same statistical properties. The values of H can lie between 0 and 1; when H=1, the surface represents self-similarity. The PSD for such a surface can be derived as a function of Hurst exponent, where:

$$C(q) = q^{-2(H+1)} \quad (2.11)$$

Thus, the power spectrum of a self-affine surface decreases as $q^{-2(H+1)}$ with increasing wavevector perfectly represented as a decay plot in Fig. 2.4. The Hurst exponent is related to the fractal dimension D_f through the formula $D_f = 3 - H$.

2.2 SURFACE FORCES

When atoms interact with each other, the forces acting can be weaker or stronger depending upon the physical nature. These interactive forces are mainly electro-magnetic and gravitational and thus they interact over distances in space. Depending upon the range of interactions they can be long range or short range. An attractive interaction potential for the force between atoms can be written in a general form of a power law as a function of inter-particle distance $w(r) = -C/r^n$ where, r is their separation, C a constant, and n some integer. The strength of this interaction potential and subsequently the force ($F = -dw(r)/dr = -nC/r^{n+1}$) largely depend upon the power law index n . Hence, gravitational, electrical and magnetic field potentials where $n = 1$ are considered long range forces.

With his well known equation of state for real gases, van der Waals in 1873 was able to show that an added amount of pressure a/v^2 exists between gas molecules due to intermolecular forces and that results into deviation from ideal gas law along with the volume change due to finite size of molecules b [67].

$$(P + a/V^2)(V - b) = RT \quad (2.12)$$

Mie in 1903 proposed an interaction pair potential of the form :

$$w(r) = -A/r^n + B/r^m \quad (2.13)$$

which for the first time included repulsive as well as attractive terms. A Lennard-Jones potential for intermolecular forces is a special case for Mie potential where $n = 6$ and $m = 12$:

$$w(r) = -A/r^6 + B/r^{12} \quad (2.14)$$

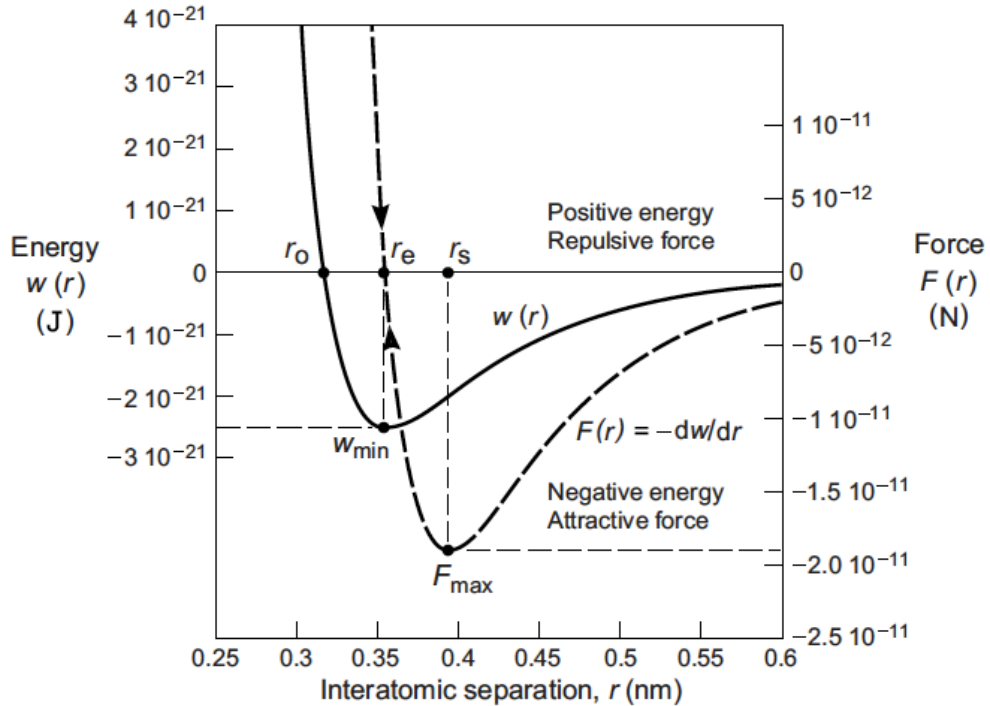


Figure 2.5: Typical van der Waals interaction energy (or potential) function $w(r)$ and force function $F(r)$ between two atoms, which are related by $F(r) = -dw/dr$. The plotted curves are for a Lennard-Jones potential with parameters $A = 10^{-77} J/m^6$ and $B = 10^{-134} J/m^{12}$ [4].

The attractive (negative) component is the van der Waals interaction potential which dominates at large distances. The equilibrium separation is where the force is zero and the energy is a minimum. Beyond the equilibrium separation as the bodies are pushed together the repulsive part starts to come into play. The adhesion or "pull-off" force is the point at which the two atoms or particles separate spontaneously when pulled apart by a force F_{max} , as shown in Fig. 2.5.

There are other stronger interactions which are not the focus of this thesis work such as electrostatics or Coulombic and chemical bond interactions. They are defined by different field potentials. With the advent of quantum electrodynamics it was possible to understand the true nature of all the interactions through first principles. It is difficult to understand the origin of interactions without a clear understanding of how molecules as dipoles influence other dipoles and their

polarizabilities. Such dipolar polarizabilities are responsible for the strength of interactions and thus physically the constant in pair potentials can be calculated to derive accurate interaction energy numbers. The constant for Van der Waal's interaction potential in eq. 2.13 is called as Hamaker's constant.

2.2.1 HAMAHER'S CONSTANT

In the previous section, we derived expression for inter-atomic and inter-particle interactions. Large surfaces require an integration of all the induced dipoles on the surface to obtain accurate interaction energy. Fig. 2.6 describes the energy and force between bodies of different geometries using the Hamaker's constant.

For two bodies (1 and 2) in a medium (3), the Lifshitz van der Waal's theory gives accurate predictions of Hamaker constant using properties such as dielectric constants and refractive indices:

$$A_{123} \approx \frac{3}{4} k_B T \left(\frac{\epsilon_1 - \epsilon_3}{\epsilon_1 + \epsilon_3} \right) \left(\frac{\epsilon_2 - \epsilon_3}{\epsilon_2 + \epsilon_3} \right) + \frac{3h\nu_e}{8\sqrt{2}} \frac{(n_1^2 - n_3^2)(n_2^2 - n_3^2)}{(n_1^2 + n_3^2)^{1/2}(n_2^2 + n_3^2)^{1/2}[(n_1^2 + n_3^2)^{1/2} + (n_2^2 + n_3^2)^{1/2}]} \quad (2.15)$$

where, $\epsilon_1, \epsilon_2, \epsilon_3$ are the dielectric constants or relative permittivity and n_1, n_2, n_3 are the refractive indices. ν_e is the absorption frequency for the materials in contact which is typically 4×10^{15} /sec.

Thus, the work of adhesion or the interaction energy for two surfaces in a medium is written as:

$$W = -\frac{A_{123}}{12\pi D_0^2} \quad (2.16)$$

where D_0 is the minimum separation distance and this number varies from interface to interface. A typical value is about 1.6 \AA .

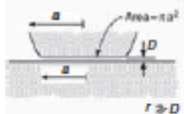
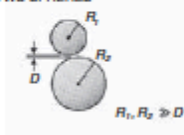
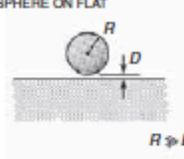
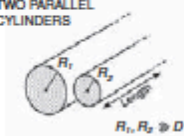
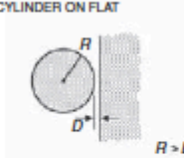
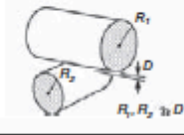
Geometry of bodies with surfaces D apart ($D \ll R$)		Van der Waals Interaction*	
		Energy, W	Force, $F = -dW/dD$
Two atoms or small molecules	TWO ATOMS or SMALL MOLECULES 	$-Cr^6$	$-6Cr^7$
Two flat surfaces (per unit area)	TWO FLAT SURFACES 	$W_{\text{flat}} = -A/12\pi D^2$	$-A/6\pi D^3$
Two spheres or macromolecules of radii R_1 and R_2	TWO SPHERES 	$\frac{-A}{6D} \left(\frac{R_1 R_2}{R_1 + R_2} \right)$	$\frac{-A}{6D^2} \left(\frac{R_1 R_2}{R_1 + R_2} \right)$ Also $F = 2\pi \left(\frac{R_1 R_2}{R_1 + R_2} \right) W_{\text{flat}}$
Sphere or macromolecule of radius R near a flat surface	SPHERE ON FLAT 	$-AR/6D$	$-AR/6D^2$ Also $F = 2\pi R W_{\text{flat}}$
Two parallel cylinders or rods of radii R_1 and R_2 (per unit length)	TWO PARALLEL CYLINDERS 	$\frac{-A}{12\sqrt{2}D^{3/2}} \left(\frac{R_1 R_2}{R_1 + R_2} \right)^{1/2}$	$\frac{-A}{8\sqrt{2}D^{5/2}} \left(\frac{R_1 R_2}{R_1 + R_2} \right)^{1/2}$
Cylinder of radius R near a flat surface (per unit length)	CYLINDER ON FLAT 	$\frac{-A\sqrt{R}}{12\sqrt{2}D^{3/2}}$	$\frac{-A\sqrt{R}}{8\sqrt{2}D^{5/2}}$
Two cylinders or filaments of radii R_1 and R_2 crossed at 90°	CROSSED CYLINDERS 	$\frac{-A\sqrt{R_1 R_2}}{6D}$	$\frac{-A\sqrt{R_1 R_2}}{6D^2}$ Also $F = 2\pi\sqrt{R_1 R_2} W_{\text{flat}}$

Figure 2.6: Van der Waals interaction energy W and force F between macroscopic bodies of different geometries in terms of their Hamaker Constant, A . Negative F implies attraction (A positive); positive F means repulsion (A negative). The Hamaker constant A is defined as $A = \pi C \rho_1 \rho_2$ where ρ_1 and ρ_2 are the number of atoms per unit volume in the two bodies and C is the coefficient in the atom-atom pair potential (top row) [4].

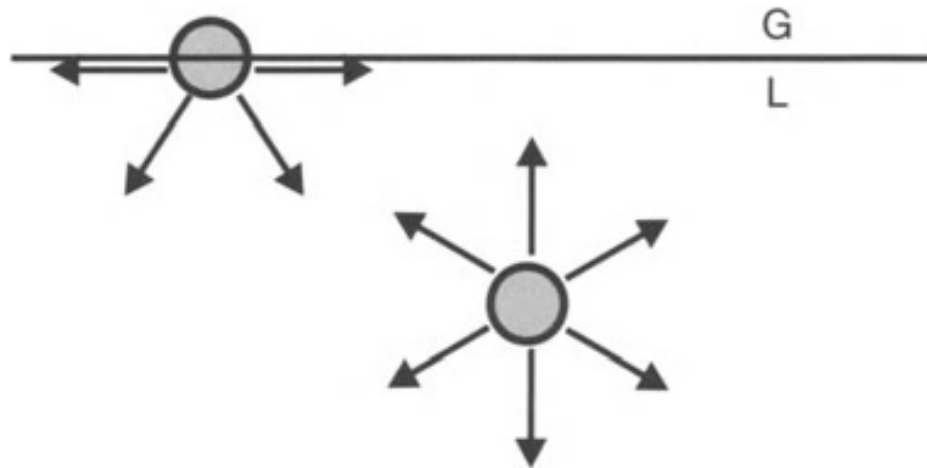


Figure 2.7: Bulk and surface dipoles depicted to show cancellation of dipoles at the interface of a gas (G) and a liquid (L)[5].

2.3 WORK OF ADHESION (THERMODYNAMICS)

In this section, the physical properties pertinent to the understanding and analysis of experimental results are defined.

2.3.1 SURFACE TENSION AND SURFACE ENERGY

Matter interacts through surfaces and interfaces. Langmuir realized that the intermolecular interactions across surfaces act through the outermost molecular layers [68, 69]. At a given surface, the surface dipoles are more active as compared to the bulk dipoles, where the net force is not cancelled out as shown in the Fig. 2.7.

Thus, there is an excess force per unit length at the surface of the liquid, known as surface tension, γ . It is this phenomena that enables formation of soap bubbles and allows a water-strider to walk on the surface of a water body. Surface tension and surface energy are related when work is done to extend the surface per unit area at adiabatic conditions. For liquids, the two quantities are same(γ_l) since

the extended surface brings new molecules from the bulk and the surface chemical composition remains as is. In case of solids, the chemical potential changes when surface is extended. Thus, the surface tension (γ_s) and surface energy for solids are different.

An indirect method of measuring solid surface tension is by wetting the surface with liquids of known surface tension and measuring the contact angle. A linear relation between cosine of the contact angle with the surface tension gives a generic plot known as Zisman plot. Zisman defined the point where this line meets $\text{Cos}\Theta = 1$ as the critical surface tension γ_c . γ_c is a measure of the surface free energy of solids but not equal to it unless the correction factor, for intermolecular interactions is equal to unity [70–72]. However, it is a useful parameter that characterizes surfaces and gives us an idea of how their free energy behaves.

2.3.2 INTERFACIAL TENSION AND WORK OF ADHESION

When two dissimilar surfaces interact in a medium, the total energy required to adhere them together is given by the Dupre equation :

$$W_{12} = \gamma_1 + \gamma_2 - \gamma_{12} \quad (2.17)$$

Where, W_{12} is the reversible work of adhesion between the surfaces of bodies 1 and 2, i.e. the separation energy is equal to adhesion energy. γ_1 and γ_2 are the surface energies of the two bodies respectively and γ_{12} is the interfacial energy between them. The interfacial energy between two surfaces is governed by the intermolecular forces acting between the two surfaces such as acid-base interactions, van der Waals forces etc. If the two surfaces that are brought into contact are identical, they will coalesce to form a homogeneous body. Then, the

decrease in free energy is the work of cohesion (W_c) which is the reversible work necessary to create two new surfaces,

$$(W_c)_1 = 2\gamma_1, (W_c)_2 = 2\gamma_2 \quad (2.18)$$

Girifalco and Good reexamined the work of adhesion and developed an interaction parameter, ϕ , which is the ratio of the work of adhesion of an interface to the geometric mean of the individual works of cohesion[73–75],

$$\phi = \frac{(W_a)_{12}}{[(W_c)_1(W_c)_2]^{1/2}} = \frac{\gamma_1 + \gamma_2 - \gamma_{12}}{2(\gamma_1\gamma_2)^{1/2}} \quad (2.19)$$

Rearranging this equation in terms of interfacial energies,

$$\gamma_{12} = \gamma_1 + \gamma_2 - 2\phi(\gamma_1\gamma_2)^{1/2} \quad (2.20)$$

That gives the Good-Girifalco equation for Work of Adhesion,

$$W_{12} = 2\phi(\gamma_1\gamma_2)^{1/2} \quad (2.21)$$

If a complete picture of surface chemical composition is known, ϕ can be calculated. In most cases, this is not feasible. Fowkes [76] gave a different approach and suggested that surface tension can be decomposed into components that show specific interactions,

$$\gamma_1 = \gamma_1^d + \gamma_1^h + \gamma_1^p + \gamma_1^i + \gamma_1^e + \dots \quad (2.22)$$

2.3.3 STRAIN-DEPENDENCE OF SURFACE ENERGY

It was Gibbs in 1876 who realized that the surface tension and the Helmholtz surface free energy of a solid surface are not the same. He verified

for crystalline solids that the value of surface tension is different in different crystal plane directions. A direct relation between surface tension and the change in surface free energy was first given by Shuttleworth in 1950, where the Shuttleworth equation is[77]:

$$\Upsilon_{ij} = \gamma\delta_{ij} + \frac{d\gamma}{d\epsilon_{ij}^s} \quad (2.23)$$

Where, δ_{ij} is the identity tensor and ϵ_{ij}^s is the surface strain tensor. Measuring this surface stress or tension has been a great challenge for soft gels, elastomers and thin films[78, 79]. Recently, Dufresne et al. and Dalnoki-Veress et al. have been able to develop methodologies using contact mechanics at sub-micron scale and contact angle measurements to show the exact nature of surface stresses at different strains[80–83]. Dobrynin et. al. has shown the increase in surface stress for an elastomer with different cross-linking densities as shown in the Fig. 2.8 [6].

2.4 CLASSICAL CONTACT/FRACTURE MECHANICS

Merriam-Webster dictionary defines mechanics as "a branch of physical science that deals with energy and forces and their effect on bodies". Without going into the development of classical mechanics, we focus on mechanics of bodies in contact. As per Newton's laws, a physical body subjected to a force will overcome inertia and undergo displacement relative to the environment to achieve certain accelerated motion. Solids when touching each other in a direction perpendicular to their surfaces, can undergo deformation, the study of this phenomena is the field of contact mechanics. Heinrich Hertz in 1882, observed that glass spheres in

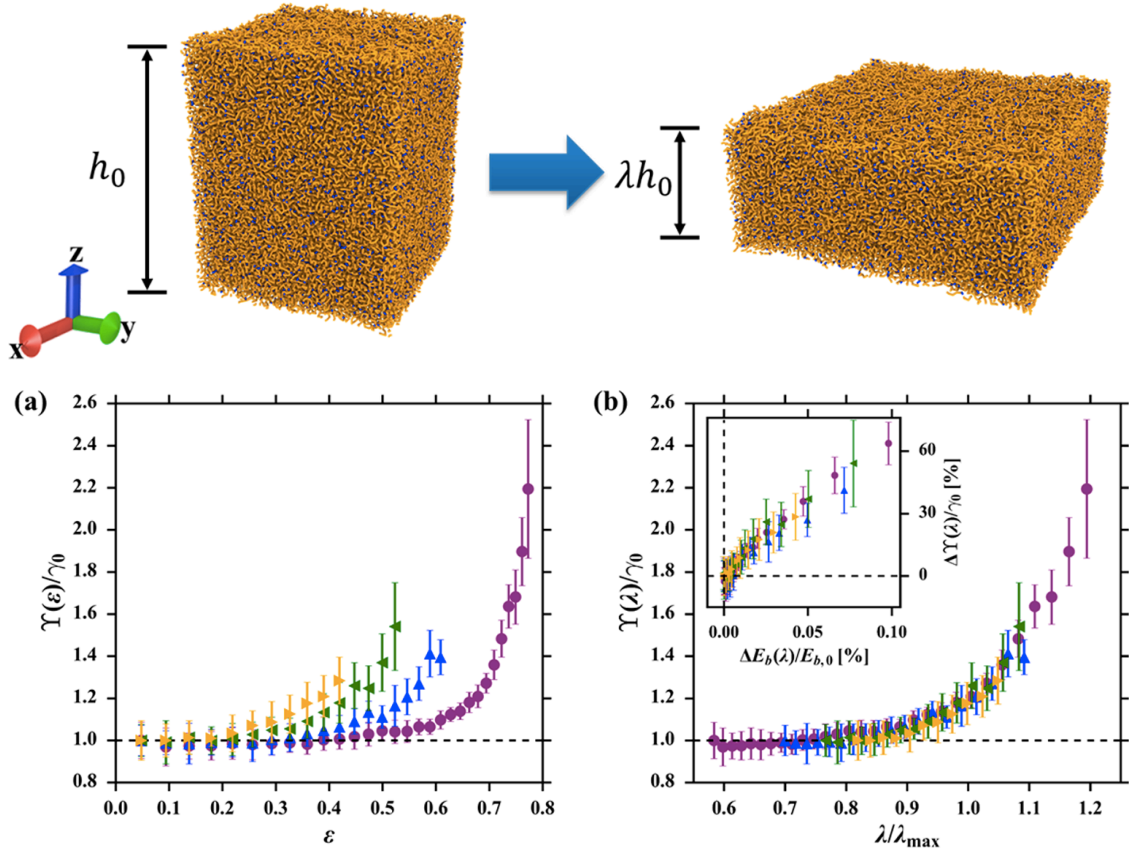


Figure 2.8: (a) Dependence of the normalized surface stress on strain for large deformations. (b) Universal dependence of the normalized surface stress on the ratio λ/λ_{max} . Inset: relative change of the normalized surface stress as a function of the relative change of the bond energy. $E_b(\lambda)$ is the bond energy in the film at different deformation ratios, and $E_{b,0}$ is the bond energy in the undeformed film. Data are shown for films of polymer networks with average numbers of cross-links per chain n_{cr} and initial film thicknesses h_0 : 6.25 and 60.3σ (purple circles); 10.42 and 59.6σ (blue triangles); 13.54 and 59.2σ (green left triangles); 16.67 and 58.9σ (yellow right triangles) [6]

contact showed a certain contact area and derived a relation for the contact radius relating to the modulus of the two contact bodies, the applied normal load and the geometry (or the radii) of lenses[37],

$$a^3 = \frac{RP}{K} \quad (2.24)$$

The Hertzian model works best for bodies having smooth surfaces and highly rigid bulk with no surface forces acting. However, in case of soft matter where the deformation is large for small stresses, the observed contact area is much larger than what is predicted using Hertzian model. At the same time, there is a non-zero contact area even when the applied force is removed provided the surfaces are clean and dry indicating strong adhesion. This was first discovered independently by Johnson alone and further developed into a theory along with Kendall and Roberts in 1971; famously abbreviated as the "JKR" (Johnson-Kendall-Roberts) model [38]. Assuming thermodynamic equilibrium, where the contact area remains constant with respect to time, the total energy balance of mechanical, elastic and surface energies gives a relation:

$$a^3 = \frac{R}{K} [P + 3\pi WR + \sqrt{6\pi WRP + (3\pi WR)^2}] \quad (2.25)$$

Figure 2.9 shows the exact difference between the contact area predicted by JKR with that predicted by Hertz.

The JKR model predicts a theoretical pull-off force found as a second solution for the energy balance:

$$F_p = \frac{3}{2}\pi WR \quad (2.26)$$

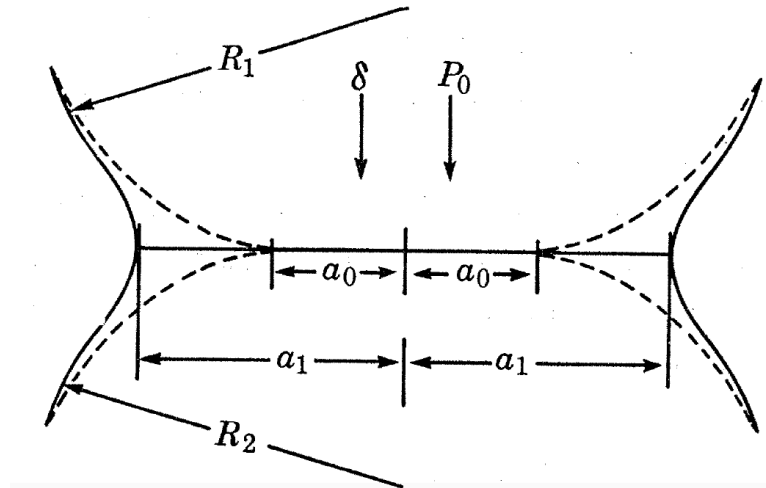


Figure 2.9: The difference in contact area for Hertz (dashed line) and JKR (bold line) show that only compressive stresses exist in an Hertzian contact while there is compression at the center and tension at the contact line for JKR contact.

The JKR contact predicts that there are infinite tensile stresses at the edge. However, the attractive forces between two surfaces must have finite range based on a Lennard-Jones force law. The JKR theory is found to be best applicable to solids with low elastic modulus and high radius of curvature [84]. The JKR theory is challenged by another theory for solids with high modulus, the Derjaguin-Muller-Toporov (DMT) theory. They argued that attractive forces between such solids must be effective in a region just outside the contact area [85]. It was later suggested that the two theories are actually two limiting cases of a general deformation behavior[86]. The cross-over limits are discussed in details by Maugis [84, 87].

2.4.1 Tabor Parameter

In 1977, Tabor argued that the assumptions of JKR theory are appropriate for contact between sphere of radius R and a plane when [88]:

$$\mu = \frac{1}{\epsilon} \left(\frac{R(\Delta\gamma)^2}{E^*} \right)^{1/3} \quad (2.27)$$

where, μ is the Tabor parameter, E^* is the effective modulus, ϵ is a length characterizing the range of interaction of the adhesive forces and $\Delta\gamma$ is the interfacial energy. It was later shown how with increasing Tabor parameter the contact quasi-rigid behavior changes from DMT to JKR [89].

2.4.2 ADHESION HYSTERESIS

Any deviation or lag of a thermodynamic quantity is termed hysteresis. Thus, any deviation in the reversible thermodynamic work of adhesion is called adhesion hysteresis. In case of contact mechanics the difference in obtained areas during loading and unloading indicates hysteretic behavior. In a JKR experiment, the a^3 v/s P (force) curve must be overlapping for approach and retraction. However, during hysteresis the curves do not overlap and the work of adhesion 'W' or ' W_a ' or ' W_{adh} ' obtained for approach and retraction are different. Fig. 2.10 describes the difference in systems with or without adhesion hysteresis.

There are numerous instances where adhesion hysteresis is observed and can be categorized into inter-penetration or diffusion of polymers at the surface, chemical surface bonds formation, viscoelastic bulk energy dissipation or increased interfacial area because of roughness. The resultant increased area gives larger interfacial energy required to separate the surfaces which is thermodynamically irreversible, as shown in Figure 2.11. Out of all reasons, roughness has been a less explored subject for its influence on adhesion hysteresis.

Except for roughness, the science of adhesion and adhesion hysteresis in terms of fracture mechanics which focuses only on the retraction or separation

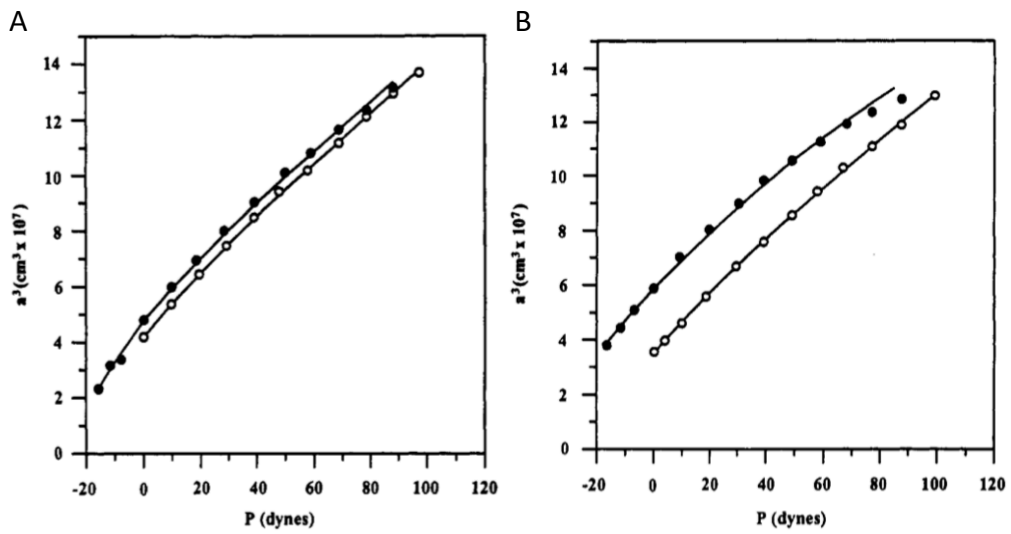


Figure 2.10: Adhesion hysteresis compared for PDMS hemisphere in contact with A. an alkylsilane and B. fluoroalkylsilane monolayer deposited on a flat mica substrate, the solid lines are the fits using JKR model (eq. 2.25). The work of adhesion obtained for loading and unloading are different for both PDMS-substrate combinations, where in case of alkylsilane the difference is less and within error bars, while the difference is significant for fluorosilane monolayer [7].

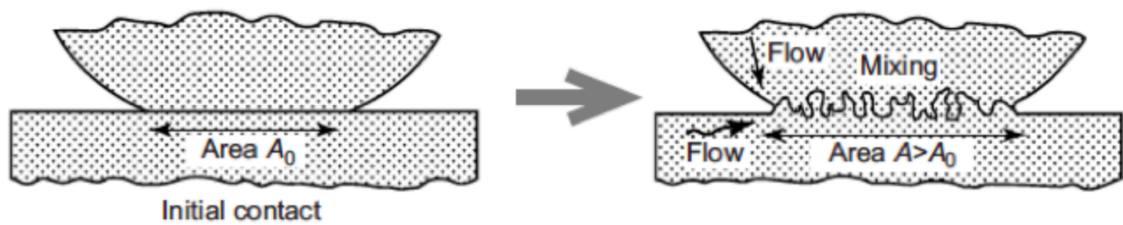


Figure 2.11: The increase in contact area due to irreversible processes

of two joint surfaces has been extensively studied. There are two different approaches that have been proposed to understand fracture. One is the energy balance approach which is somewhat similar to the discussion so far with respect to thermodynamic work of adhesion. Griffith in 1921 suggested that there should be sufficient energy available to form two new surfaces [90]. In other words, fracture occurs only if the energy (strain energy release rate, G) is larger than the critical energy necessary to extend a crack over a unit area. While, the other approach deals with the stress field around a sharp crack, which should satisfy the condition to overcome the intermolecular forces. Irwin developed regimes for this stress field and termed it as stress intensity factor, K . Fracture only occurs when K exceeds a critical value called fracture toughness [91]. Let us briefly consider these two approaches.

2.4.2.1 Energy Balance Approach

A certain amount of energy is required to create a unit area of fracture surface, δA . Therefore, the crack can only propagate if this amount of energy, or more, is available. The source of this energy is work (w) done on the system by external forces and the release of elastic energy (U) in the system due to the relaxation of the stresses at the crack. The difference between the two sources is the potential energy available for the fracture. The rate of change of this energy difference in a lamina of thickness b with respect to crack extension δa ($\delta A = b \delta a$) is the strain energy release rate,

$$G = \frac{\delta(w - U)}{\delta A} \quad (2.28)$$

If P is the load acting on the system at the onset of crack propagation and u is the displacement, $\delta w = P\delta u$ and for a linearly elastic material and small displacement, $U = \frac{1}{2}Pu$, then,

$$G\delta A = P\delta P - \frac{1}{2}(P\delta u + u\delta P) \quad (2.29)$$

If the compliance of the system is given by $C = u/P$,

$$G = \frac{P^2}{2} \frac{\delta C}{\delta A} \quad (2.30)$$

The crack will only propagate when G is equal to or exceeds a critical energy release rate, G_c , sometimes called the fracture surface energy. Naturally, this condition is satisfied when P corresponds to the minimum amount of force that can propagate the crack, P_c . Consequently, the criterion for fracture is represented as,

$$G \geq G_c = \frac{P_c^2}{2} \frac{\delta C}{\delta A} \quad (2.31)$$

When the length of crack growth is much smaller than the size of the whole system, the fracture process can be considered to be under fixed-growth or constant load. Therefore, C can be measured or calculated as a function of A and P_c can be measured at the onset of crack growth. Then, G_c can be unambiguously obtained by using equation 2.29. This equation is also valid for cracks at or near an interface as it is in adhesion processes. Most importantly, G_c may be related to W_a . Since two new surfaces are formed during fracture, G_c should be converted into surface free energy. However, the energy required for crack propagation was found to be far greater than W_a . This is firstly because crack growth along interfaces (or

in materials) often incorporates rupture of intrinsic bonds such as secondary (e.g. van der Waals forces) and primary bonds (e.g. chemical bonds). This energy is the intrinsic fracture energy, G_0 . Secondly, fracture often causes viscoelastic and/or plastic deformation due to high strains. Therefore, realistically, in the presence of energy dissipation,

$$G_c = G_0 + \psi \quad (2.32)$$

where ψ is the energy dissipated in viscoelastic and plastic deformations at the crack tip. Through this parameter, the fracture energy becomes rate and temperature dependent. Gent and Kinloch [92], Andrews and Kinloch [93, 94] as well as Gent and Schultz [95] proposed that ψ depends on G_0 as,

$$\psi = G_0 \mathfrak{f}(\dot{a}, T, \epsilon) \quad (2.33)$$

Thus, equation 2.31 becomes,

$$\psi = G_0(1 + \mathfrak{f}(\dot{a}, T, \epsilon)) \quad (2.34)$$

also known as the Gent equation, where \mathfrak{f} is a function that depends on crack growth rate (\dot{a}), temperature (T), and strain level (ϵ). This relationship is a result of the fact that there can only be stress developed around the crack tip if the region ahead of the crack tip is intact with intermolecular forces. When viscoelastic and plastic energy losses are negligible, $\mathfrak{f}(\dot{a}, T, \epsilon) \rightarrow 0$ and the measured fracture energy is a measure of G_0 . If only secondary bonds are effective at the interface, the value of G_0 should be equal to the value of W_a . The ψ function is found to be heavily dependent on the chain networks entanglement, conformation, size

and the all the factors that could influence the relaxation time. Gent and Petrich observed that the crack growth rate or the rate of peel shows a single master curve over a wide range of temperatures by means of Williams-Landel & Ferry (WLF) frequency-temperature equivalence [96, 97].

2.4.2.2 Stress Intensity Factor Approach

An unperturbed system is held together by intermolecular forces. In such a system crack can only propagate if the stresses at the crack tip are enough to rupture these forces. The crack tip stresses shown in Fig. 2.12 can be calculated using Irwin's approach. it is assumed that the crack is uniformly stressed in a homogeneous system, the strain is infinitesimal (r is much smaller than the overall length of the crack) and the behavior of the material obeys Hooke's Law (Linear Elastic Fracture Mechanics) [98].

$$\sigma_{yy} = \frac{K_I}{(2\pi r)^{1/2}} \cos(\theta/2) [1 + \sin(\theta/2) \sin(3\theta/2)] \quad (2.35)$$

$$\sigma_{xx} = \frac{K_I}{(2\pi r)^{1/2}} \cos(\theta/2) [1 + \sin(\theta/2) \sin(3\theta/2)] \quad (2.36)$$

$$\sigma_{xy} = \frac{K_I}{(2\pi r)^{1/2}} \cos(\theta/2) [1 + \sin(\theta/2) \sin(3\theta/2)] \quad (2.37)$$

where σ_{ij} are the stress tensor components at the vicinity of the crack at a point P described by the pola coordinates r and θ . The analysis here is for plane stress where the out of plane stress $\sigma_z = 0$. K is the stress intensity factor which depends upon the applied stress and the geometry the geometry of the crack and the system. The subscript 'I' refers to a mode I crack propagation.

Considering a crack embedded in a linear elastic material which extends in the negative x-direction with its tip at $x = 0$, the crack may be stressed in three

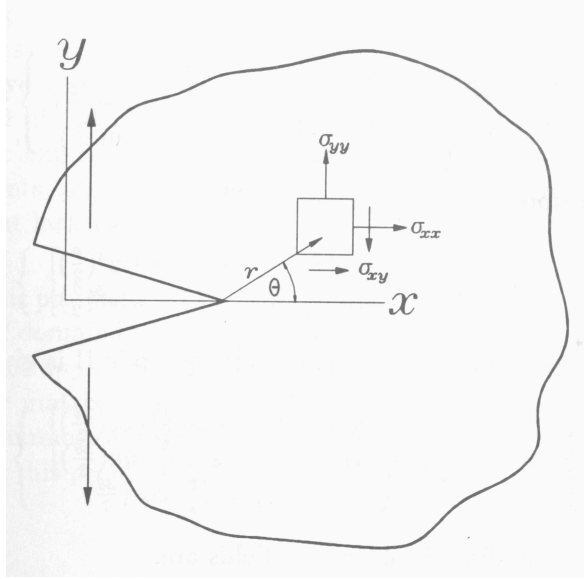


Figure 2.12: Stresses around a crack tip for a tensile type loading [8].

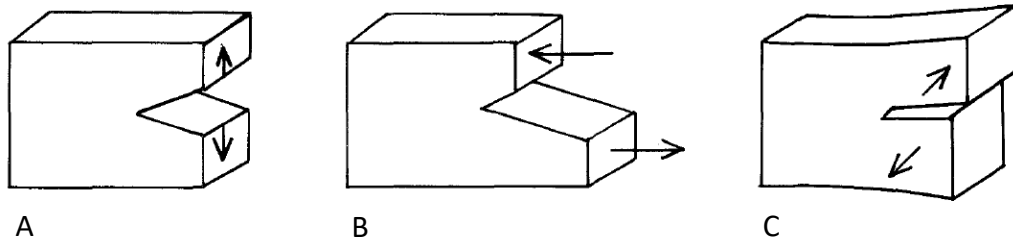


Figure 2.13: The three fracture modes A. Cleavage mode: mode I, B. In-plane shear mode: mode II, C. antiplane shear mode: mode III [9].

different modes as shown in Fig. 2.13 : (a) the cleavage (tensile-opening) mode (mode I), (b) the in-plane shear mode (mode II) and (c) the antiplane shear mode (mode III). The superposition of all the three modes describes the loading. The fracture mode I is the most relevant to adhesion failure.

From eq 2.36 it is seen that the stresses are effective when P approaches to the crack tip. Eventually, $\sigma \rightarrow \infty$ and becomes singular as $r \rightarrow 0$. This means that ahead of the crack tip a zone exists where the stresses exceed the plastic yield stress level of the polymer. In general, this plastic zone is assumed to be small enough not to disturb the elastic stress field. Only then it may be defined by the elastic stresses. An important characteristic of the singularity mentioned above is

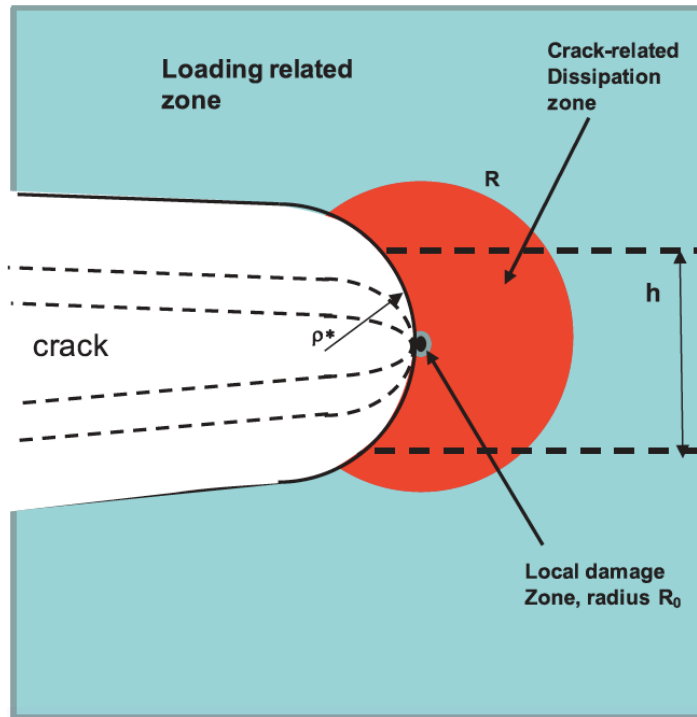


Figure 2.14: Vicinity of a crack tip describing dissipated or plastic zone (Irwin's model)[10].

that the stress field local to the crack tip is similar for all loadings. The difference is only apparent in the magnitude of K which makes this parameter the main interest in the stress intensity factor approach. As a result, the level of K uniquely defines the stress field around the crack. Thus, fracture occurs when K exceeds a critical value. This leads to the criterion for crack propagation postulated by Irwin (schematic in Fig. 2.14).

2.4.3 PRESSURE-SENSITIVE ADHESIVES (PSAs)

An adhesive with both viscous and elastic components that spreads onto a surface based upon the applied pressure is known as a pressure-sensitive adhesive (PSA). A pressure sensitive adhesive can react to both positive and negative pressures and thus is usually reversible. A PSA is usually made up of a lightly cross-linked polymer as shown in the figure 2.15 above.

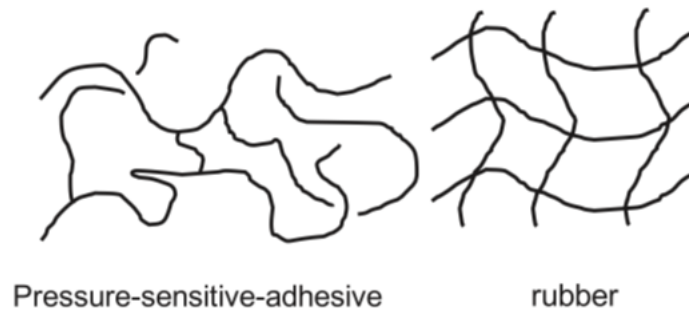


Figure 2.15: Schematic of a weakly cross-linked and entangle pressure-sensitive adhesive and a crosslinked rubber [10]

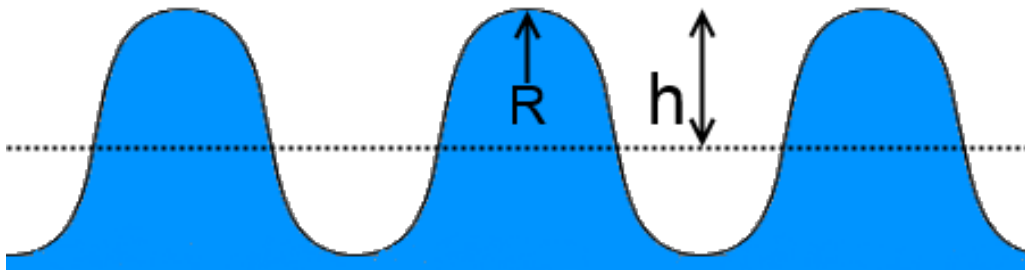


Figure 2.16: A simplistic view of rough surfaces as assumed by Dahlquist for developing PSAs

A scientist at 3M, Carl Dahlquist, described an empirical theory for designing pressure sensitive adhesives, also known as "the Dahlquist criterion of tack" where, based upon the size of the asperities (curvature radius and height) and the work of adhesion between adhesive surface and the rough surface, the desired critical modulus for a particular adhesive can be calculated. For micron size asperities and work of adhesion of about $50 \text{ mJ}/\text{m}^2$, the number is around 0.3 MPa using the following empirical relation and Figure 2.16 [99],

$$G_c = W \sqrt{\frac{R}{h^3}}. \quad (2.38)$$

However, this empirical relation does not include the viscous effects which are necessary for a PSA to work. Hence, assumptions of truly elastic systems can be valid only through thermodynamic equilibrium models such as JKR.

2.4.4 ADHESION ON ROUGH SURFACES

A simple Hertzian or JKR model that works for smooth surfaces in contact becomes difficult to test for a rough surface. As we have seen earlier that a rough surface has asperity sizes of various different length scales; it becomes difficult to incorporate surface topography directly into thermodynamic models to measure true work of adhesion between surfaces. Adhesion between rough surfaces was seen to be very critical for electrical conduction between linearly elastic metal surfaces [100]. Researchers looked at the contact areas when stationary as well as sliding [25], where it was found that the conductance of contacting metal surfaces is pressure-dependent and the real contact area between them is extremely smaller (1/10000 times) than the apparent area. In shear motion, where interfacial friction comes into play, the deformation of soft materials affects the forces observed and hence understanding contact mechanics first is crucial before moving to shear geometry. In 1957, Archard was the first to measure adhesion on fractal surfaces and he showed that area of real contact (A_{real}) is proportional to normal load (P), $A_{real} \sim P$ [26] for conforming elastic contact, extending the two Amontons's laws of friction where,

1. The shear force is proportional to applied normal load.

$$F_s \propto P \tag{2.39}$$

2. The coefficient of friction is independent of the apparent area of contact.

$$\mu_f \neq A_{app} \quad (2.40)$$

Following his study, there have been various research efforts that predicted the area of real contact on a self-affine fractal surface as a function of normal load proportional to a power law[42, 101, 102].

2.4.3.1 Multi-asperity Contact Models

Greenwood and Williamson studied the real area of contact between a smooth elastic surface and a rough elastic surface. In the GW model, it is assumed that the rough surface is represented by asperities with identical radius of curvature, β , while their heights follow a Gaussian distribution as[42],

$$\phi(z) = \frac{1}{h_{rms}} e^{-z^2/2h_{rms}^2}. \quad (2.41)$$

By applying Hertzian theory for each contact asperity, the total contact area, A_c , and total force, F_0 , can be obtained as:

$$A_c = \pi\beta N \int_d^\infty (z - d)\phi(z)dz. \quad (2.42)$$

Where N is the total number of asperities and total separation force, F_0 , can be obtained as:

$$F_0 = \frac{3}{2}\sqrt{\beta}NE_s \int_d^\infty (z - d)^{3/2}\phi(z)dz. \quad (2.43)$$

$1/E_s = (1 - \nu_1^2)/E_1 + (1 - \nu_2^2)/E_2$ is the effective elastic modulus. Multi-asperity contact theory was initiated by this original GW model and was later refined by Bush, Gibson and Thomas(BGT) [103] and recently by Carbone [104]. The Fig.

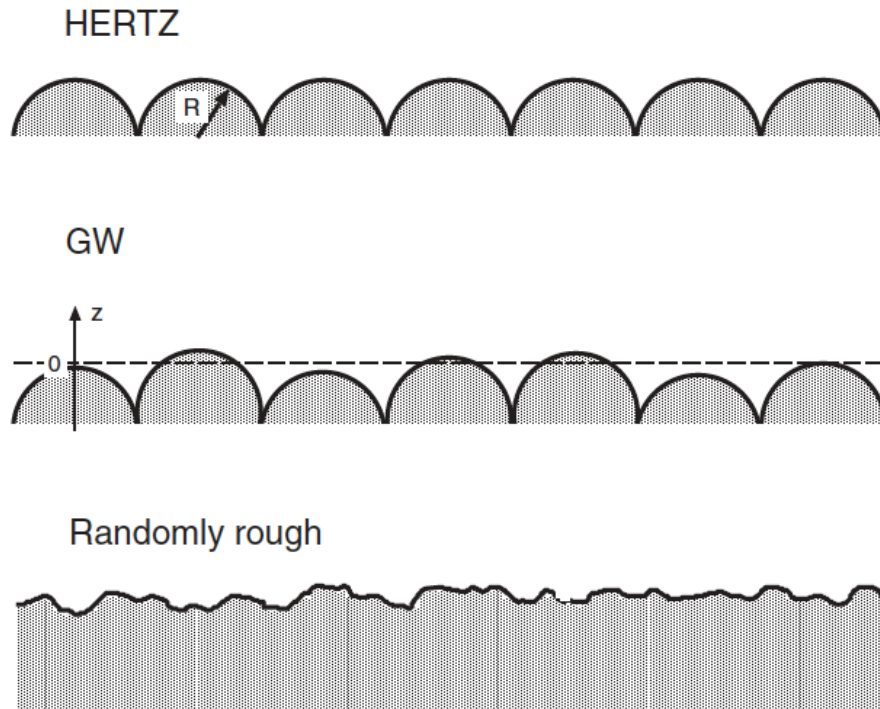


Figure 2.17: Comparison of roughness models assumed in development of different theories [11].

2.17 shows the difference for model surfaces between Hertz, GW and a randomly rough surface.

The GW multi-asperity model discussed above is limited in that there are no interactions between neighboring asperities. For pressures substantially greater than the elastic modulus or roughness size, contact regions might physically get close enough to form a larger domain. Furthermore, the distribution of the size and shape of asperities depends on the measurement parameters i.e. bandwidth sufficiency and multi-scale nature of rough surfaces. On one hand, if the roughness profile is bandwidth limited, the sampling frequency must be sufficiently high to completely resolve the profile. On the other hand, considering the broadband multi-scale character of the profile is a more subtle issue. All these limitations are even more severe for the contact of rough surfaces or compliant materials.

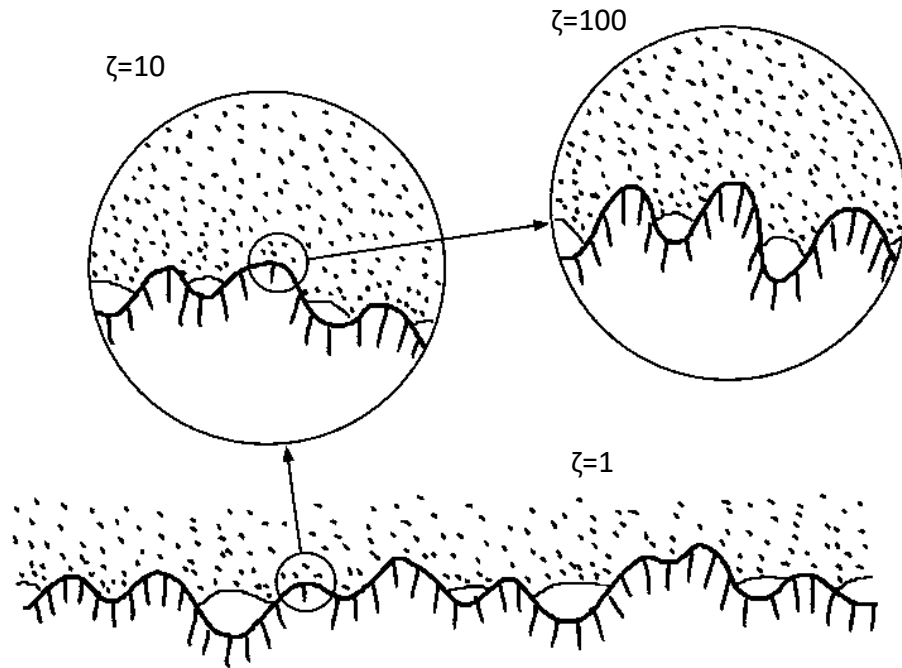


Figure 2.18: depicts the contact on a self-affine surface where at each magnification a different real area of contact can be imagined [12].

2.4.3.2 Persson's Theory

Figure 2.18 depicts an accurate picture of contact between two rough surfaces at different magnifications. At the lowest magnification, $\zeta = 1$, it looks as though there is complete contact for larger asperities. On increasing the magnification, the roughness at smaller and smaller length scales is detected revealing that the contact is taking place only at high asperities[12]. As a matter of fact, the real contact area would vanish if there is no short distance cut-off[105]. Persson's theory of contact mechanics on rough surfaces focuses on including roughness on all length scales [27].

Persson and Tosatti developed a theory for elastic soft surface in contact with a randomly rough surface [13]. As shown in Fig. 2.19b, assume a uniform stress σ acts within a circular area (radius R) of a semi-infinite body having elastic modulus E . This results in a perpendicular displacement u by a distance which

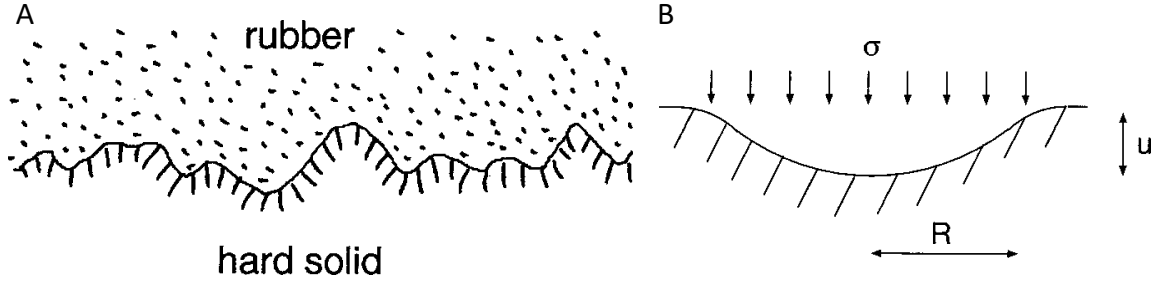


Figure 2.19: A. shows the state of conformal contact between rubber continuum and hard rough surface, B. shows deformation at a single asperity contact [13]

can be calculated using continuum mechanics, $u/R \approx \sigma/E$. Thus, $u \sim (\sigma/E)R$. Thus, if h and λ represent perpendicular and parallel roughness length scales, respectively, then if $h/\lambda \approx \sigma/E$ and the perpendicular stress will be sufficiently large to deform the rubber to make conformal contact with the substrate. Let us now look at the rubber-substrate adhesive interaction. When the rubber deforms and fills out a surface cavity of the substrate, an elastic energy $U_{el} \approx E\lambda h^2$ will be stored in the rubber. Now, if this elastic energy is smaller than the gain in adhesion energy $U_{ad} \approx -\Delta\gamma\lambda^2$, where $-\Delta\gamma$ is the local change of surface free energy upon contact due to the rubber-substrate interaction, then (even in the absence of the load F_N the rubber will deform spontaneously to reach the valleys between asperities. The condition $U_{el} = -U_{ad}$ gives $h/\lambda \approx (\Delta\gamma/E\lambda)^{1/2}$. For example, for very rough surfaces with $h/\lambda \approx 1$, and with parameters typical of rubber $E=1$ MPa and $\Delta\gamma = 3$ meV/Å, the adhesion interaction will be able to deform the rubber and completely fill out the cavities if $\lambda < 0.1\mu\text{m}$. For very smooth surfaces $h/\lambda \sim 0.01$ or smaller, so that the rubber will be able to follow the surface roughness profile up to the length scale $\lambda \sim 1$ mm or longer.

The qualitative argument discussed above assumes roughness on a single length scale λ . But the surfaces or real solids have roughness on a wide distribution

of length scales. Having said that, Persson further derived expressions for stored deformation energy and the adhesion energy for a self-affine surface (described in section 2.1.3). However, keeping this work in focus, where our generalized assumption of a rough surface being randomly rough, without deriving adhesion theory of self-affinity or self-similarity, works perfectly in practical experiments. Hence, we will not discuss Persson's qualitative argument further.

Persson also discusses a quantitative argument which is useful in every sense for the following chapters. Here, a complete theory is developed based upon the stored elastic energy and adhesive energy for a smooth elastic surface in contact with a rough surface having known power spectral density function. As seen in Fig. 2.19a, a rubber surface is in complete conformal contact with the rough surface. Assuming that the conditions of conformal contact are met, let us calculate the difference in free energy before the elastomer came into contact with the surface and after complete contact is achieved. Let $z=h(x)$ be the height of the rough surface above a flat reference plane such that $\langle h \rangle = 0$. Assume first that the rubber is in direct contact with the substrate over the whole nominal contact area. The surface adhesion energy is assumed proportional to the contact area so that

$$U_{ad} = -\Delta\gamma \int d^2x [1 + (\nabla h(x))^2]^{1/2} \quad (2.44)$$

$$\approx -\Delta\gamma \left[A_0 + \frac{1}{2} \int d^2x (\nabla h(x))^2 \right] \quad (2.45)$$

where it is assumed that $|\nabla h| \ll 1$ (small slope approximation). Using, $h(x) = \int d^2q h(q) e^{iq \cdot x}$ we get,

$$\begin{aligned}
\int d^2x (\nabla h(x))^2 &= \int d^2x \int d^2q d^2q' (-q \cdot q') \langle h(q)h(q') \rangle e^{i(q+q') \cdot x} \\
&= (2\pi)^2 \int d^2q q^2 \langle h(q)h(-q) \rangle \\
&= A_0 \int d^2q q^2 C(q)
\end{aligned} \tag{2.46}$$

where the surface roughness power spectrum is given as :

$$C(q) = \frac{1}{(2\pi)^2} \int d^2x \langle h(x)h(0) \rangle e^{-iq \cdot x} \tag{2.47}$$

Thus, using eqs. 2.44. and 2.45:

$$U_{ad} \approx -A_0 \Delta \gamma \left[1 + \frac{1}{2} \int d^2q q^2 C(q) \right] \tag{2.48}$$

We can now calculate the elastic energy stored in the deformation field in the vicinity of the interface. Let $u_z(x)$ be the normal displacement field of the surface of the elastic solid. We obtain,

$$\begin{aligned}
U_{el} &\approx -\frac{1}{2} \int d^2x \langle u_z(x) \sigma_z(x) \rangle \\
&= -\frac{(2\pi)^2}{2} \int d^2q \langle u_z(q) \sigma_z(-q) \rangle
\end{aligned} \tag{2.49}$$

From solid mechanics and Persson's derivation [27], we know that,

$$u_z(q) = M_{zz}(q) \sigma_z(q), \tag{2.50}$$

where,

$$M_{zz}(q) = -\frac{2(1-\nu^2)}{Eq}, \tag{2.51}$$

E being the elastic modulus and ν the Poisson's ratio. If we assume that complete contact occurs between the solids, then $u_z = h(x)$ and from Eqs. 2.47 and 2.49-2.51,

$$\begin{aligned} U_{el} &\approx -\frac{(2\pi)^2}{2} \int d^2q \langle u_z(q)\sigma_z(-q) \rangle [M_{zz}(-q)]^{-1} \\ &= \frac{A_0 E}{4(1-\nu^2)} \int d^2q q C(q) \end{aligned} \quad (2.52)$$

Thus, the change in free energy when the rubber block is in contact with the rough substrate is given by the sum of Eqs. 2.48 and 2.52,

$$U_{el} + U_{ad} = -\Delta\gamma_{eff} A_0, \quad (2.53)$$

where,

$$\Delta\gamma_{eff} = \Delta\gamma \left[1 + \pi \int_{q_0}^{q_1} dq q^3 C(q) - \frac{\pi E}{2(1-\nu^2)\Delta\gamma} \int_{q_0}^{q_1} dq q^2 C(q) \right] \quad (2.54)$$

The above derivation is applicable for surfaces with arbitrary random roughness which is the case for most of the natural surfaces. Persson and many others have used the above general theory to solve complex contact mechanics problems both in experiments and simulations, that we would be briefly discussing in following section.

2.4.3.3 Previous Experiments and Simulation Results

In 1970s, After the development of JKR theory that sufficiently explained the role of surface forces on contact between elastic solids, there were attempts to bring soft materials in contact with rough surfaces to understand the influence of roughness on adhesion. Hemispherical lenses of different types of rubber casted from polished smooth molds were brought in contact with roughened Perspex

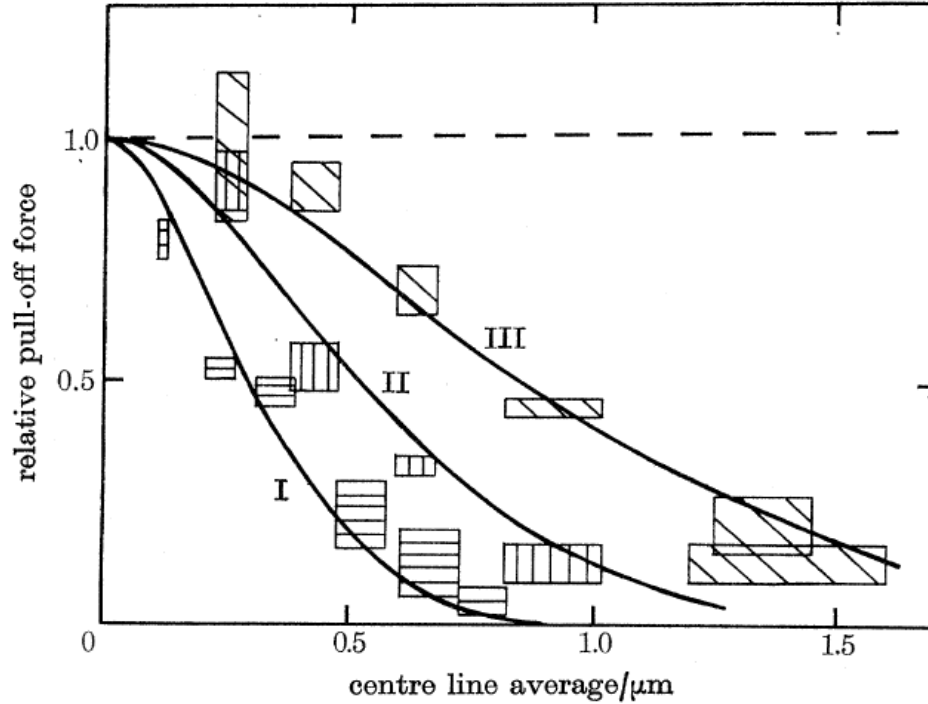


Figure 2.20: Relative pull-off force for smooth rubber spheres in contact with a flat Perspex surface as a function of the roughness of Perspex. Effects of modulus, E , of the rubber: curve I, $2.4 \times 10^6 \text{ N m}^{-2}$; curve II, $6.8 \times 10^5 \text{ N m}^{-2}$; curve III, $2.2 \times 10^5 \text{ N m}^{-2}$ [14].

(commercial polymethylmethacrylate (PMMA)). The roughness of Perspex and the modulus of rubber were varied. However, these experiments had very little control over surface chemistry and roughness measurements given the technological developments during that time. Fuller and Tabor used three different moduli with three different roughened Perspex surfaces such that the arithmetic average (R_a) or center line average for the rough surfaces was different [14].

As it can be seen from the Fig. 2.20 that the pull-off forces between rubbers and perspex decreases with increasing roughness parameter and increasing modulus. Fuller and Tabor also compared these results with rolling friction experiments to show that the friction forces scale similarly to adhesion on rough surfaces; which we will discuss in the next section. Following Fuller and Tabor's work, Briggs and Briscoe also performed similar experiments using surfaces with

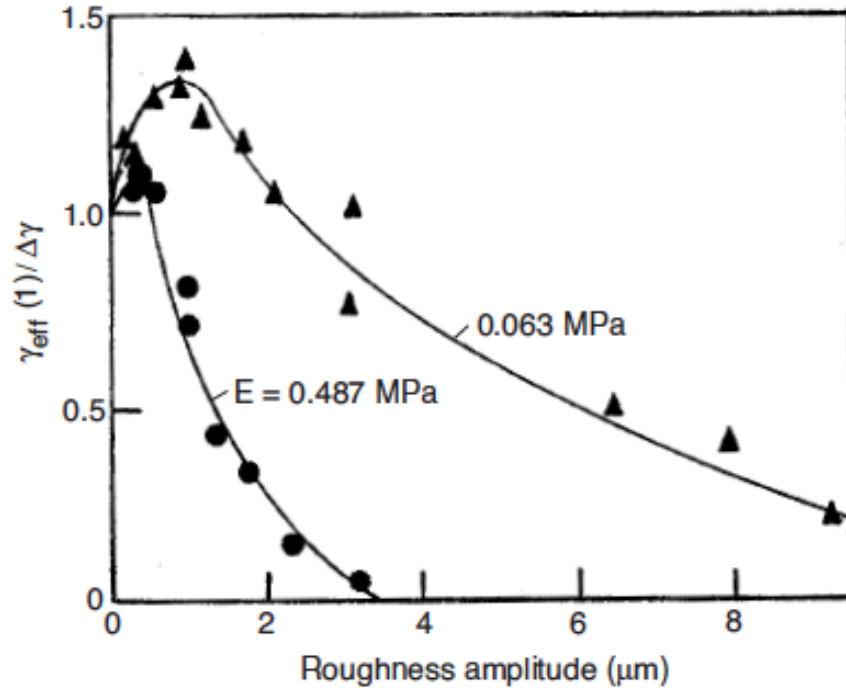


Figure 2.21: Relative adhesion energies calculated from pull-off for a smooth rubber surface in contact with a Perspex surface as a function of the roughness, using a crossed cylinder configuration. \circ RTV 602 ($E = 487 \text{ kPa}$) Δ Dow Corning XF-13-523 ($E = 63 \text{ kPa}$) [15].

even smaller average roughness and softer rubber on a cross-cylindrical setup. They observed that the relative adhesion energy (calculated from the theoretical pull-off obtained using JKR equation) was highest for an intermediate roughness and softer rubber as seen in the Fig. 2.21 below [15, 106].

Briggs and Briscoe's experiments were a proof that roughness can enhance adhesion and can result in significant adhesion hysteresis and that sub-micron size asperities can increase adhesion dramatically for soft rubber. As we have seen earlier that single surface roughness parameters can be same for surfaces with different topographies (section 2.1.1) it is not appropriate to make comparisons to the observations of more recent studies where theory of surface roughness has matured.

For experiments on rough surfaces with known PSDs that apply Persson's theory, there have been multiple studies that show striking observations. Peresadko et al. performed contact measurements between PDMS and sand-blasted glass surfaces with known surface roughness (the AFM scans and resulting PSDs are shown in Fig. 2.22 to show that the pull-off adhesion measurement is independent of the effective surface area due to roughness (effective adhesion energy from pull-off is compared in Fig. 2.23). The reasoning for the observation was that since the hysteresis or pull-off adhesion is dependent on the stored elastic energy and thus the third moment of PSD while the surface area depends on the second moment of PSD, there is little influence due to surface area[50]. While at first glance, this might be a correct interpretation for the measured adhesion energy during pull-off, the deeper investigation was necessary to understand the difference in predicted or approach work of adhesion versus the pull-off adhesion energy.

JKR-like contact experiments between an AFM tip and rough elastic substrates are also hysteretic in comparison to a smooth surface predictions as shown in Kesari's experiments in Fig. 2.24 wherein the force-displacement curves are not exactly reversible for rough surfaces (Fig. 2.24 A and B). As a result, application of JKR theory becomes difficult to extract work of adhesion. However, the observations of hysteresis loops for an ideal smooth surface and on a rough surface stand as a proof of adhesion hysteresis solely as a consequence of roughness.

The authors further calculated the energy lost through integration of the force-displacement curves for elastic surfaces with varying RMS roughness. As seen in Fig. 2.25 B, the plot shows an optimum length scale of asperities that increases

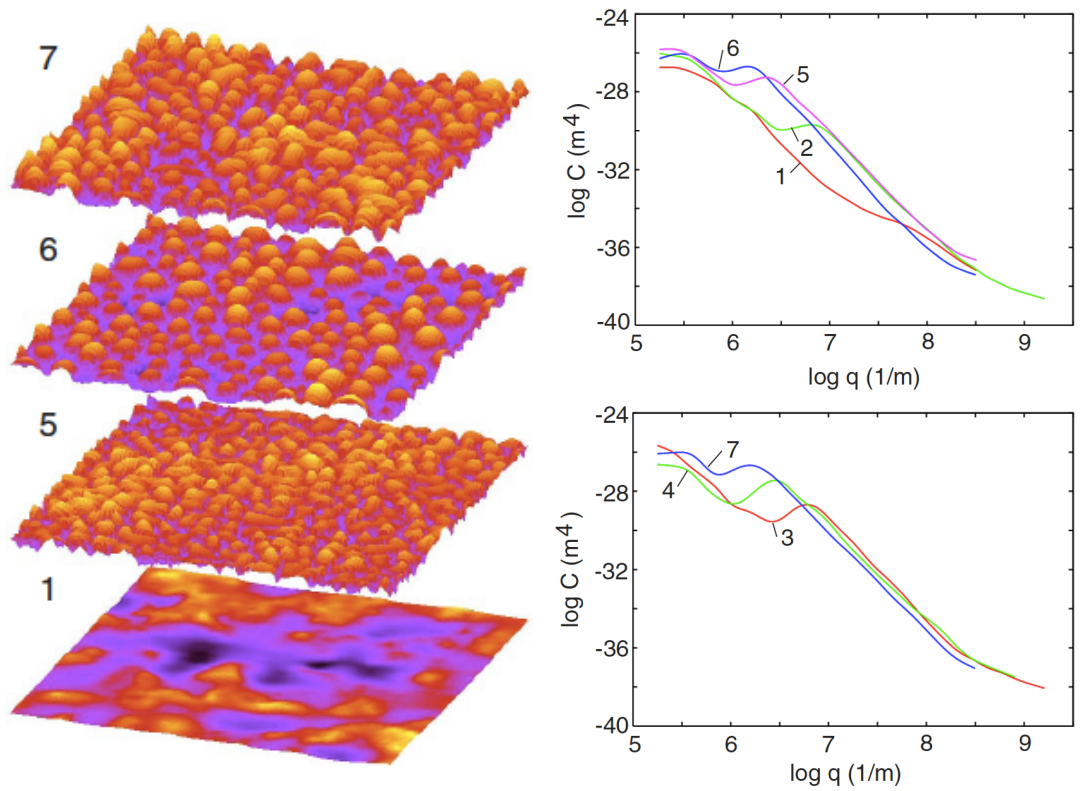


Figure 2.22: $50 \times 50 \mu\text{m}$ AFM scans of sand blasted glass surfaces along with their Power Spectral Density functions.

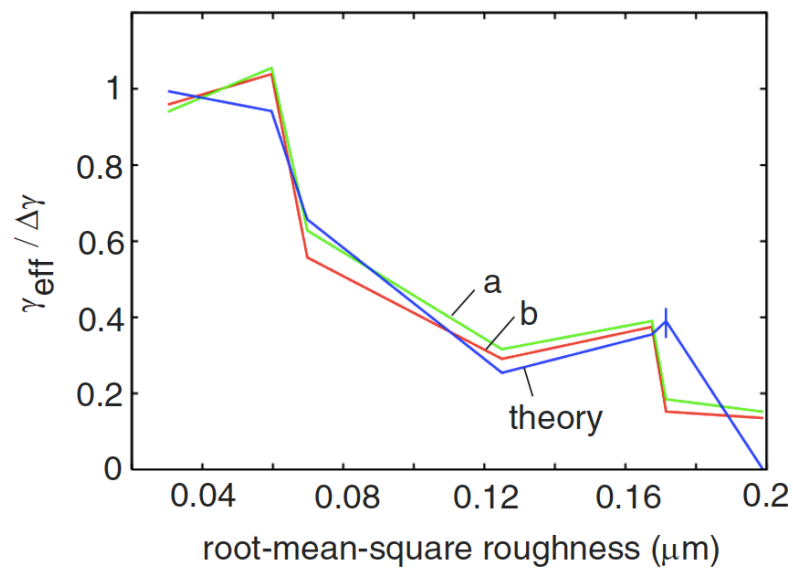


Figure 2.23: The effective adhesion energy as a function of RMS roughness for 7 different rough glass surfaces. Blue curve is the theoretical predictions, green curve (a) is experimental pull-off at $0.2 \mu\text{m}/\text{sec}$ and red curve (b) is at $2 \mu\text{m}/\text{sec}$.

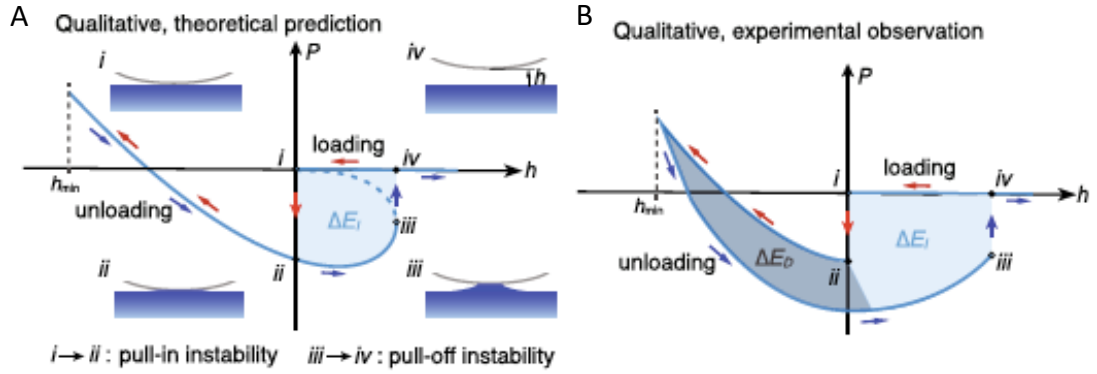


Figure 2.24: A. Schematic of Load versus Displacement (P-h) curve as per JKR theory. The pull-in ($i \rightarrow ii$) and pull-off ($iii \rightarrow iv$) instabilities are marked with the corresponding configurations. A complete contact cycle includes the loading (red arrows) and unloading (blue arrows) phases. The size of the hysteresis loop formed in the contact cycle due to the elastic instabilities denotes the hysteretic energy loss ΔE_i . B. Experiment with rough surfaces showing a P-h curve with a large hysteresis loop that is load- or depth-dependent[16].

adhesion. It is to be noted that the loss of energy also varies with normal loads which is highlighted in Kesari's work and is termed as Depth-Dependent Hysteresis (DDH) [16, 107]. All the above experiments point to questions as to whether scalar roughness parameters can be reliable to predict soft elastic adhesion. However, as it is seen here there could be varied observations for similar experiments depending upon the range of length scales chosen.

2.5 FRICTION

Friction is a response to shear between two surfaces and is measured by the resisting force offered by the interface between the two surfaces sliding past each other. During shear, there could be different processes such as toppling, wear, lubrication or pure sliding depending upon the path taken for releasing the applied energy. Thus, all these phenomena show non-conservation and energy dissipation that happens during friction. Most of the applied energy eventually is transmitted

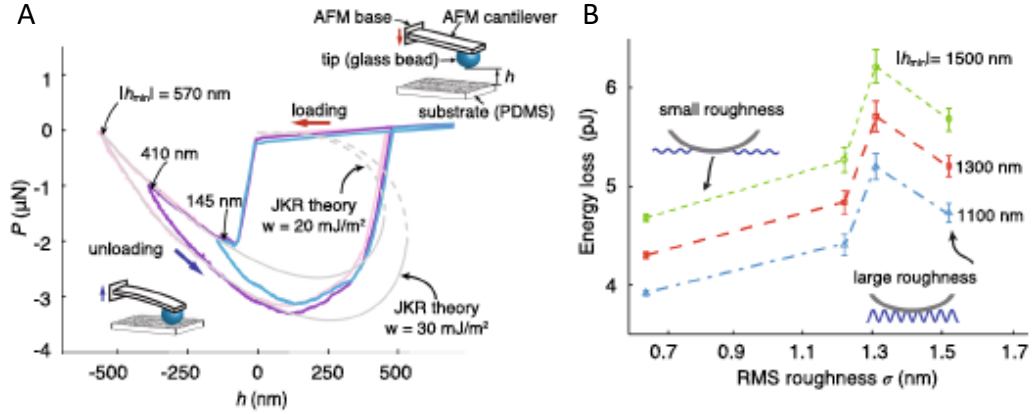


Figure 2.25: A. As the load or depth increases the energy lost due to hysteresis for an AFM glass bead in contact with rough PDMS surface increases. B. Energy lost plotted as a function of RMS roughness of the elastic half-space [16].

as heat. Before the advent of soft materials such as polymers and elastomers, most of the metallic and mineral materials exhibited dry solid friction. The component of friction that is desirable is the traction or grip during motion useful to land vehicles for acceleration, deceleration and changing directions. Starting from Da Vinci and Amontons, many findings on friction have been reported, some contradictory and all incomplete. However, they have laid down the foundations for the modern scientific studies in the field of tribology. More progress in the study of friction depends on detailed characterization and molecular level understanding of surfaces and interfaces. This led to the resurrection of the adhesion aspect of friction that was first proposed by Desaguliers in 1734 [108]. Since the mechanical interlocking approach was never able to explain friction completely, the adhesion hypothesis was the best alternative. In 1929, Tomlinson elaborated on the molecular adhesion approach and suggested that the normal load and the friction force are linearly related to the number of interacting atoms but his attempts did not produce any quantitative result [109]. Bowden and Tabor developed the adhesion theory of friction and they recognized that two surfaces make contact only

at peaks of asperities. Under very high stresses these points are subject to local plastic deformations. If the real area of contact is A , the hardness of the softer material is H , and the shear strength of the bond is S , then the average normal pressure, P , and friction force, F , can simply be expressed by,

$$P = AH \quad (2.55)$$

$$F = AS \quad (2.56)$$

$$\mu = \frac{F}{P} = \frac{S}{H} \quad (2.57)$$

The simple empirical model (based on Coulombic friction [110]) fails to explain experimental results since the theory neglects deformation and interactions accounting only the adhesive part of friction. The shear strength of the interface is a term used in calculation however, it is very difficult to measure independently. It is shown to miscalculate the friction force in elastic materials by about a factor of 10 with no incorporation of contribution from surface roughness. At very smooth surfaces, the friction is high due to large area of contact, whereas at very rough surfaces the friction is high due to interlocking. The friction is at its minimum and almost independent of roughness in the intermediate range[111]. Besides, plowing (equivalent to abrasion and accumulation of debris) and electrical interactions are two other major factors that contribute to friction. The former takes place when a surface with sharp asperities of slope ' θ ' slides over a softer surface. These asperities dig into the soft material producing grooves. The plowing term has been considered by the adhesion theory by adding $\tan\theta$ since it creates additional resistance to sliding. $\tan\theta$ may be large for rough surfaces such as sandpaper

causing the plowing contribution to be large. However, $\tan\theta$ usually has a value around 0.05 and the plowing term is negligible. The electrical interactions are effective when an electrical double layer exists at the interface. Sliding requires the separation of opposite charges and thus causes an increase in the friction force. There is no term in the adhesion theory to account for the electrical interactions but it is believed to have an extremely small contribution. Though the tribology community is convinced that there is adhesion at every interface between any two surfaces, a complete theory cannot be developed unless the contribution of adhesion is resolved.

An effective engineering solution to avoid complete contact between surfaces to reduce friction is lubrication. It is important to shed light on what happens when lubricants are present at the interface since there is a lot to draw resemblance with friction on rough surfaces. Essentially, a lubricant limits solid-solid contact to reduce wear and friction wherein roughness can also limit contact between solids with the lubricant replaced by air or vacuum. Many important studies at the beginning of twentieth century among tribologists such as Mayo D. Hersey and Richard Stribeck showed that the friction force in presence of lubricants is non-linear function of applied normal load [112–114]. In simple terms, the friction coefficient varies with different normal loads (P), velocities (v) and the viscosity(η) of the lubricant used. There could be three different regimes based on the boundary condition obtained using a dimensionless parameter known as the Hersey's number ($= \eta * v/P$). The plot of friction coefficient versus Hersey's number is known as the Stribeck curve as shown in the Fig. 2.26.

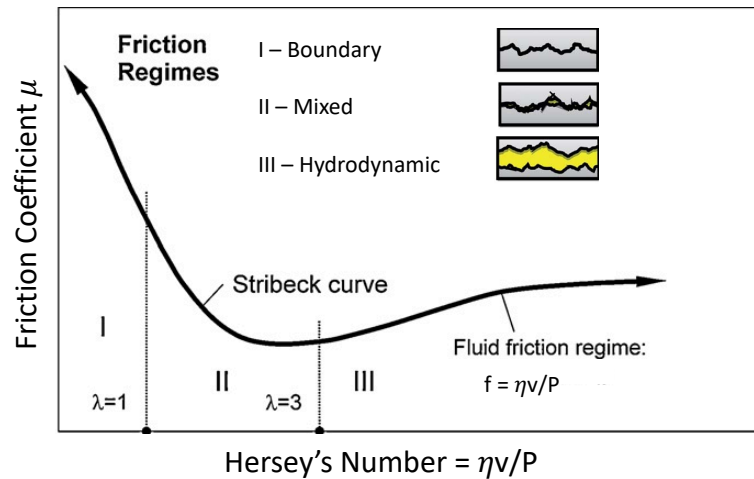


Figure 2.26: Stribeck curve with three different regimes for friction with lubrication[17, 18].

The above characteristics of the Stribeck curve highlight the non-linear nature of friction and supports the hypotheses that friction is not solely Coulombic in nature. One observation among non-linear effects, which is of practical significance, is that of stick-slip behavior wherein the two surfaces overcome a static friction and undergo slip instabilities repeatedly instead of steady sliding in kinetic friction. These are the same instabilities that create the squeaking or cracking sound through the metal hinges when you open the door. Notice that this sound is only heard when the door opens at intermediate velocities and not when you open it very quickly. Stick-slip behavior can be periodic (usually sawtooth and oscillatory) and the philosophical debate that still exists is about the origin of these instabilities. The geological phenomena known to create earthquakes is the constant stick-slip that cascades between two tectonic plates[115]. The stick-slip behavior can be observed with or without interfacial chemical bonds and elastic deformation that happens during solid-solid contact[116]. If the elastic solid is soft (in case of elastomers) or there is possibility of glassy or crystalline ordering

of the interface (such as a hydrocarbon monolayer or grafted brushes), the elastic deformation due to interfacial adhesion and chain extension along with state transitions from solid-like to liquid-like can cause stick-slip[117, 118].

2.5.1 RUBBER FRICTION ON ROUGH SURFACES

In previous section, we understood some of the important characteristics of friction for solid-solid contact especially stick-slip behavior which was also the earlier discovery in tribology. There are many other instabilities that occur for soft elastomers sliding on surfaces and in this section we will explain how roughness plays its role. The simplest of all cases is when there is steady state sliding between two bodies under dry conditions. But in reality this is observed only at extremely low velocities for most sliding interfaces where distinction between only static and kinetic regions can be made[119]. We discuss the most relevant aspects without much exploration into the complete history of rubber friction. As the velocity increases the elastic or viscoelastic deformation due to adhesion has higher local stresses for the rubber. In general, it is found that if certain critical stress matched the modulus of the rubber during sliding there would be a state transition or occurrence of instabilities as a function of sliding velocity. A few experimental examples are given below. Apart from coefficient of friction, the other important measurable parameter using friction is the overall shear stress observed. The observed trends are similar since stress is just the shear force normalized with the total contact area ($\sigma_s = F_s/A$) and thus coefficient of friction and stress are linearly proportional ($\sigma_s = \mu P/A$) [23, 119].

One of the pioneering experiments in friction of elastomers was done by two eminent contemporaries, Grosch and Schallamach. Schallamach first measured

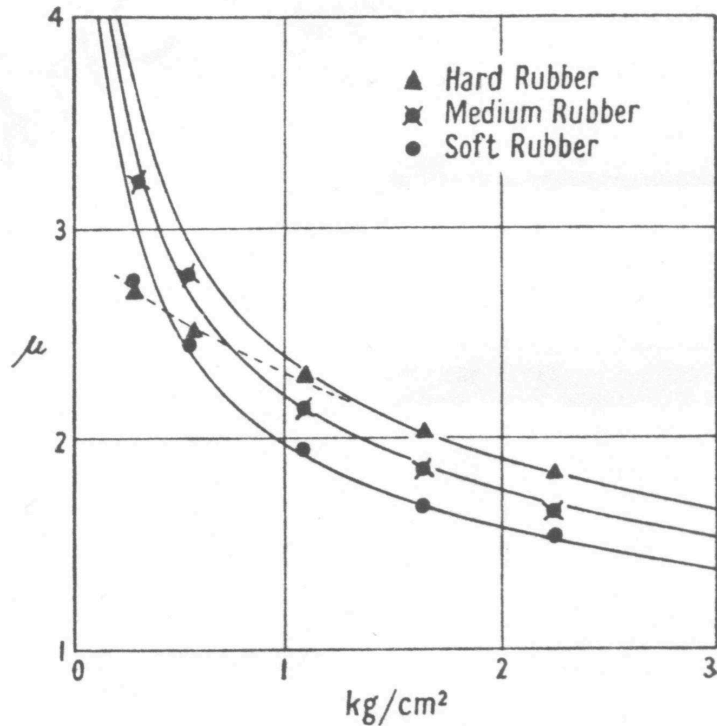


Figure 2.27: Coefficient of friction as a function of load. Full lines are the theoretical predictions. The dotted line is experimental points for hard rubber [19].

friction for elastomer of three different moduli (soft, medium and hard) along with load dependence experiments. As seen in Fig. 2.27 below, the frictional force increases with modulus for all systems but at low loads the behavior of hard rubber departs from the theoretical predictions. Schallamach avoided the modulus dependency but tried to explain the behavior of the hard rubber with the contact area dependency. Since contact is achieved by the asperities, at low loads only the tallest asperities are in touch and the true area of contact is smaller than the ideal case. The smaller asperities come gradually into contact as the load is increased and the true area of contact eventually reaches the ideal case. According to Schallamach, this should be most pronounced with the hard rubber.

Schallamach also investigated the effects of velocity and temperature on rubber friction [120]. He observed that at a constant temperature frictional force

increases with sliding velocity and at a constant velocity it decreases with an increase in temperature. Schallamach concluded that such a behavior follows Eyring's theory of reaction rates. Therefore sliding of an interface is solely an adhesion mechanism where formation and breakage of molecular bonds take place in separate, thermally activated events. This sliding process is governed by an activation energy that he found to have a value of 30 kcal/mole. Greenwood and Tabor argued that some part of the energy must be dissipated for the deformation of the elastomeric material [121]. However, Grosch is known to perform the most systematic study [56]. He tested the friction of various rubbers with different viscoelastic properties for temperature (-50C to 90C), velocity ($\mu\text{m}/\text{sec}$ to cm/sec) and roughness effects using a belt-driven system with flat rubber sheet surface in contact with flat solid surface. Friction increased nonlinearly with velocity and decreased with increasing temperature as seen in the Fig. 2.28 as an example for natural rubber. This velocity and temperature dependence was transformed into a master curve shown in Fig. 2.29 by using the superposition principle of Williams, Landel, and Ferry [97]. According to the time temperature superposition principle, for a polymer which is visco-elastic, rate and temperature are inter-changable i.e. it has similar mechanical response at high rate and low temperature and vice versa above its glass transition temperature (T_g). In polymer physics, glass transition is point at which a rubbery viscoelastic polymer becomes frozen in chain mobility and becomes amorphous usually at low temperatures. Grosch found the same amount of characteristic shift factor (a_T) that reduces to a mastercurve for coefficient of friction as obtained for the viscoelastic rubber for a range of velocities at different temperatures. With the help of following equation, the reference temperature at 20

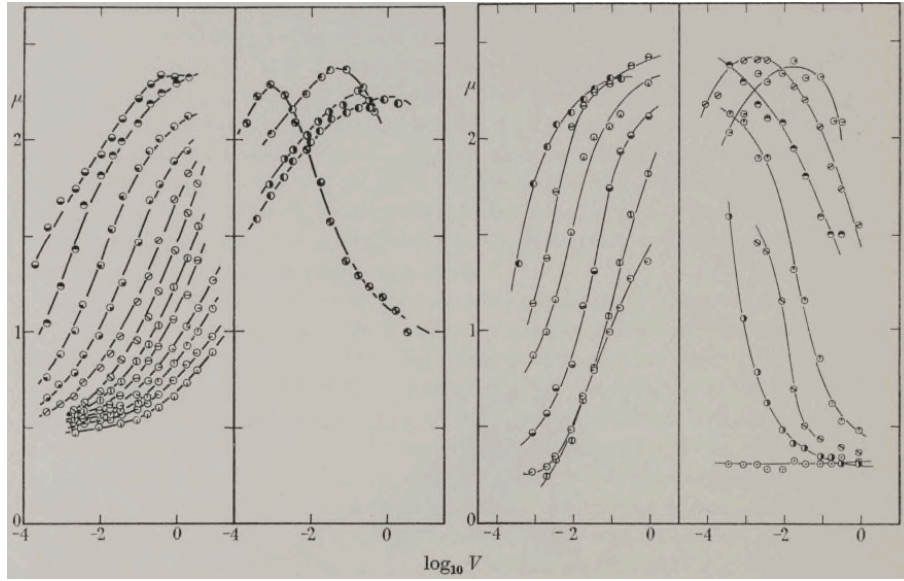


Figure 2.28: Coefficient of friction as function of the sliding velocity at various temperatures of the natural rubber on clean silicon carbide. Curves are shown in two groups for clarity. The symbols denote different temperatures ranging from -60C to 90C.

C is shifted from a standard temperature which is a characteristic of the elastomer and found to be 50 C higher than its glass transition temperature $T_s = T_g + 50$:

$$\log_{10} a_T = \frac{-8.86(T - T_s)}{101.5 + T - T_s}. \quad (2.58)$$

As it can be seen that the friction on smooth silicon carbide shows a peak at an intermediate velocity before which it increases monotonically. Grosch also performed friction on wavy glass and dusted silicon carbide, here coefficient of friction exhibits a peak shown in Fig. 2.29B. When the smooth surface is dusted with magnesia powder to prevent contact, the friction remains almost constant indicating that friction on smooth surfaces is due to interfacial adhesion. While the friction at lower velocities is higher on rough dusted surface as compared to the smooth surface, Grosch argued that this higher shear force is due to higher deformation energy required to conform to increased area. The deformation energy loss is absent or minimal on smooth surface. Grosch's results showed that

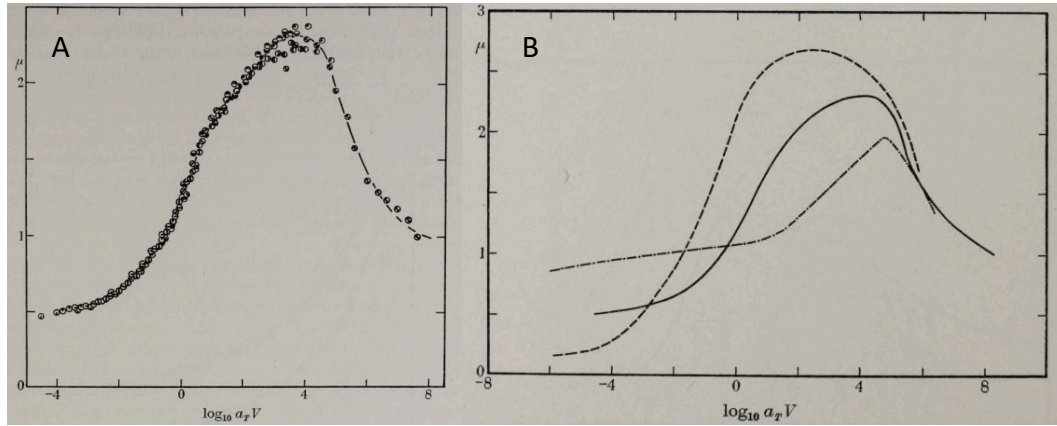


Figure 2.29: A. The mastercurve of all the curves superposed from Fig. 2.28 using time-temperature superposition principle to give coefficient of friction for natural rubber B. Master curves for the coefficient of friction of natural rubber on the three surfaces, - - - wavy glass, — clean silicon carbide, - . . - dusted silicon carbide; all curves referred to 20 C

both adhesion and deformation contributes to friction. This adhesion component correlates well with the loss component of the rubber and thus the relaxations at the interface during sliding are related to the segmental energy dissipation of the polymer chain (see Fig. 2.30). The ratio of the velocity at the maximum friction to the frequency at the maximum viscoelastic loss is 7 nm. This length scale represents the distance of the molecular jumps during sliding.

Grosch mentioned the possibility of frictional heating at high velocity but Schallamach showed that a single master curve can still be obtained by taking the true surface temperature into account [122]. A very interesting finding in Grosch's study is the frictional behavior at low velocities. In this region, considering viscoelasticity, friction is expected to fall to very small values while it actually becomes almost independent of velocity and temperature.

Following Grosch's observations, Schallamach refined his theory to correct for the insufficient explanations regarding the monotonic dependence of dynamic friction on velocity [122]. However, he maintained his view that friction is caused

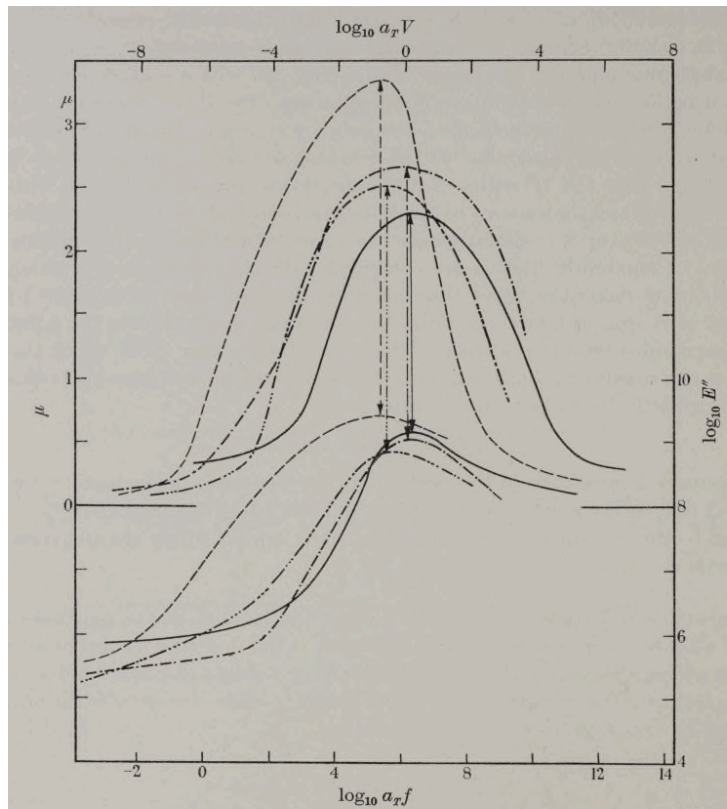


Figure 2.30: Master curves of the coefficient of friction of rubbers B, C, D and E on glass referred to their respective T_g temperature. Below: Loss modulus curves E'' as function of frequency for the four rubbers referred to their respective T_s temperatures. Velocity and frequency have been displaced with respect to each other by $\log_{10} \lambda = 6.2$. - . - . - B styrene butadiene; — C acrylonitrile butadiene; - - - D butyl rubber, - . . . - E natural rubber

purely by molecular adhesion on smooth surfaces. He proposed a general equation for friction that involves the number and average life of bonds as well as the average time between the breakage and reformation of a bond. This molecular stochastic model was further refined by Chernyak and Leonov wherein the total time chain spend in stretching, debonding and reattaching result into overall stress behavior. All these time scales would depend upon the length and density of the chain as well as velocity of chain pull-out [58]. The Chernyak-Leonov model is discussed in chapter 5 with more relevance.

When Schallamach conducted experiments at very high velocities between rubber lenses and smooth surfaces, he observed prominent instabilities traveling through the contact area. These detachment waves move from front of the contact area to the back at a higher velocity than the sliding velocity of rubber (observe Fig. 2.31). The observed contact displacement and thus nominal stress is considerably reduced which is contrary to expectations of monotonically increasing friction with velocity. This shows that the Schallamach waves occurrences are a stress relaxation mechanism beyond a critical strain or extension ratio [123]. Lateral observations clearly show air pockets traveling as waves through the rubber sliding over the surface [124]. Thus, detachment waves reduce the contact area at the interface. Some of the recent studies have found resemblance of Schallamach waves to patterned structures or wrinkling formed due to residual stresses observed in elastic thin films [125, 126]. There have been no systematic study for Schallamach waves on rough surfaces.

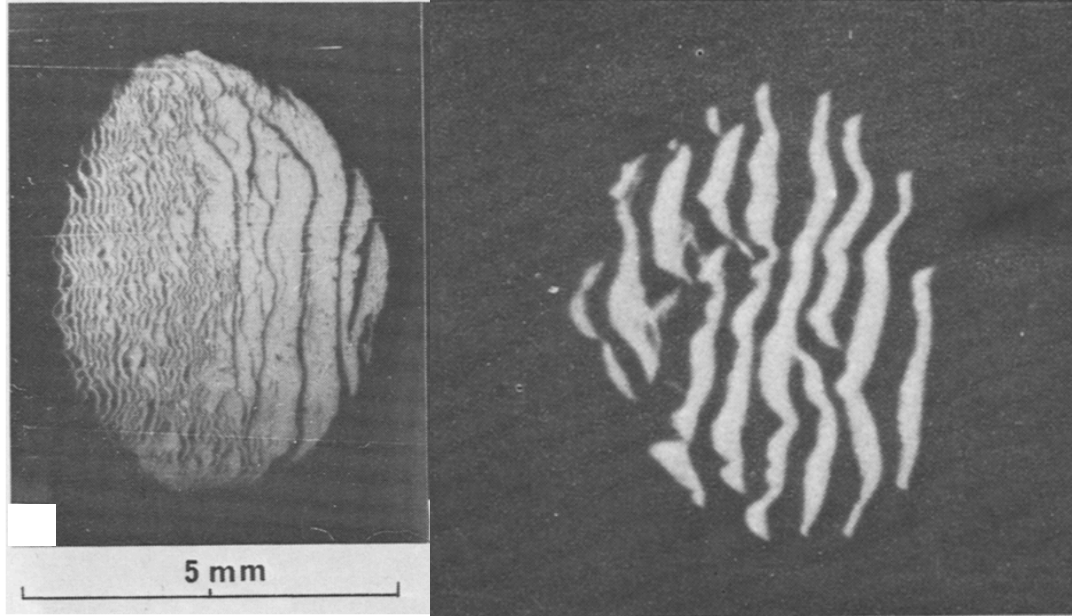


Figure 2.31: Contact between natural rubber and perspex track, $v=0.23$ c/s. Single frame of a film of the contact between perspex and a butyl sphere sliding over it at 0.043 c/s.

Thus, it is now clear why the laws of solid friction have little relevance to rubber friction, since for rubber friction the coefficient of friction or shear stresses depend on normal load, roughness, velocities and temperature.

2.5.1.1 Persson's Theory of Rubber Friction

The discussion in section 2.4.3.2 was for stationary surfaces in contact. In case of sliding, we need to take into account the elastic modulus as a function of perturbing frequency, $E(\omega)$, where ' E ' is a complex quantity and $\omega = v/\lambda$ where v is the sliding velocity and λ is the wavelength of oscillation. According to Persson's rubber friction theory, the imaginary part is related to the internal friction of the rubber or energy dissipation. The mechanism is not well established but empirically is derived by Bhowmick et al. as[127],

$$\Delta E = \pi \gamma_0^2 E''(\omega). \quad (2.59)$$

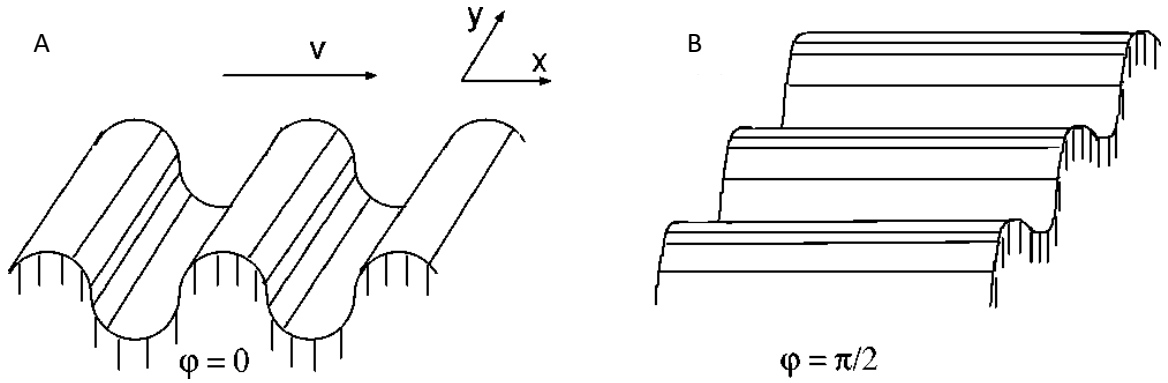


Figure 2.32: A cosine roughness profile with the wave vector A along, and B perpendicular to the sliding direction. Only in case A will the surface roughness generate time-dependent (fluctuating) deformations of the rubber block.

Where γ_0 is the strain and E'' is the loss modulus. Persson's equation for shear stress during rubber friction in ref. [27] is also based on similar dissipated energy concept. He writes,

$$\Delta E = \sigma_f A_0 v t_0. \quad (2.60)$$

Here, σ_f denotes the frictional shear stress for the time period t_0 , A_0 being the surface area. The velocity of sliding ' v ' can be written as a derivative of displacement field. Without mentioning all the details, the shear stress as a function of roughness looks as follows,

$$\sigma = \frac{1}{2} \int dq q^3 C(q) \cos \phi \operatorname{Im} \frac{E(qv \cos \phi)}{1 - \nu^2}. \quad (2.61)$$

Where, $C(q)$ is the power spectral density of rough surface, $q = 2\pi/\lambda$ is the wave vector. Where ν is the Poisson's ratio, $\operatorname{Im} E$ is the loss modulus obtained from bulk measurements and ϕ is the angle at which the roughness profile is oriented from the sliding direction, as shown in the Fig.2.32. So far the equation is valid

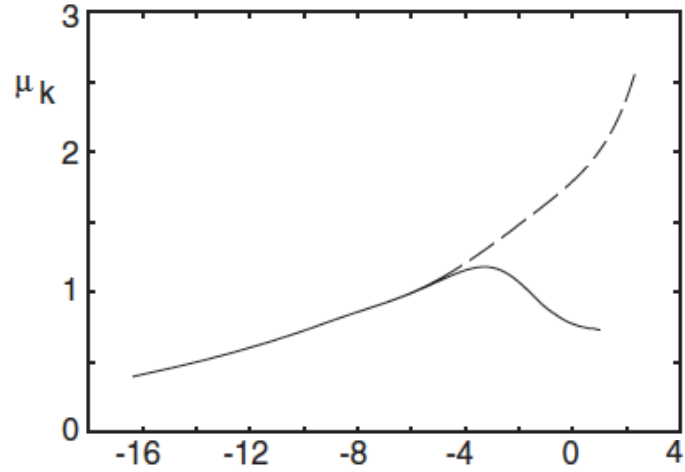


Figure 2.33: The kinetic friction coefficient as a function of the logarithm of the sliding velocity. The solid and dashed curves are with and without flash temperature effects, respectively.

for most randomly rough surfaces. However, Persson further derived complete expression for self-affine surfaces where he equated the real area of contact as a function of the roughness and complex elastic modulus of the rubber. The impact of heat generation/flash temperature on friction clearly indicate that the effect is dominant at extremely high velocities(above \sim m/sec), which is not the scope of this thesis for the experiments performed are below the predicted velocities [128]. Furthermore, Persson’s Theory has been explicitly applied to experiments assuming surfaces to be self-affine [129, 130].

2.5.1.1 Rubber Friction Experiments with Roughness

Rubber friction is more complicated than the non-adhesive term derived in eq. 2.61. It is influenced by two decoupled phenomena just as in case of adhesion, the adhesive term and the hysteresis/deformation term,

$$\mu_{shear} = \mu_{adhesion} + \mu_{deformation} \quad (2.62)$$

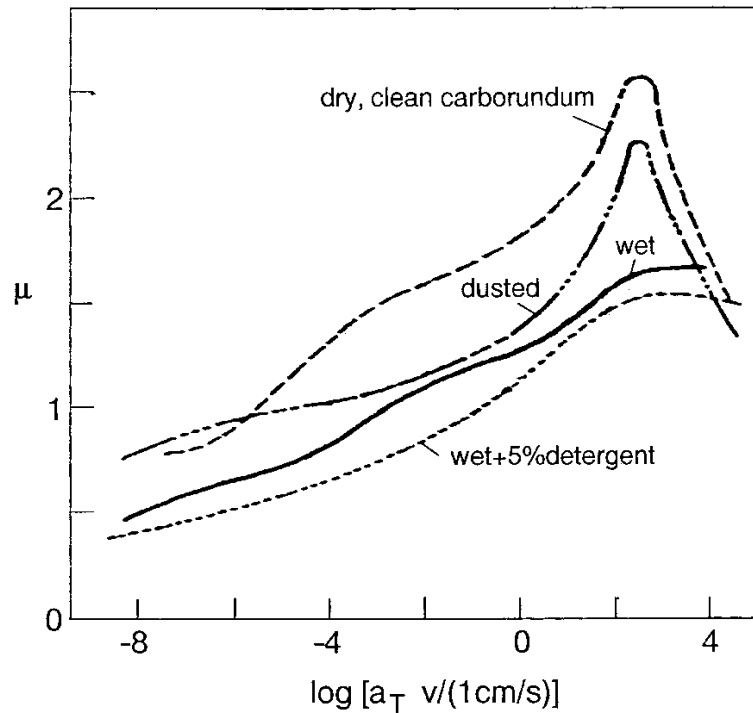


Figure 2.34: The kinetic friction coefficient for rubber sliding on a carborundum surface under different conditions [20]. Experimental results for a rubber block sliding on dry clean ~dashed line, dusted ~dashed?dotted, and wet ~solid line carborundum stone surfaces.

Surfaces under friction such as tire treads are usually contaminated and change the roughness profile of the surface such that the small and big asperities of the size of contaminants particles are no more rigid. Further reducing the effective contact area and thus adhesion. Similarly, oil and other liquid contaminants would create interfacial patches. It is well known that the tire traction is much higher on a dry road surface after a heavy rainfall. Grosch's experiments in the example shown in Fig. 2.34 demonstrate the nature of friction forces. The figure also show results for wet surfaces with an added ~5% detergent. It has been shown that polar substances like soaps prevent direct contact between track and rubber; this explain why the friction is slightly lower for the wet 5% detergent case, compared to the wet, clean carborundum surface.

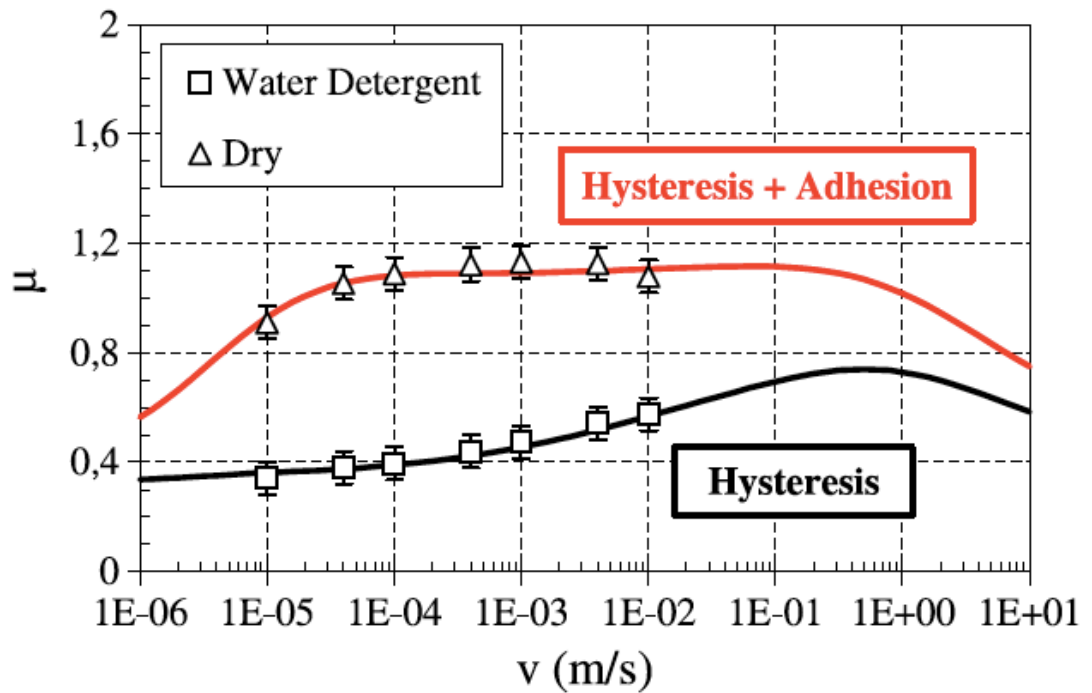


Figure 2.35: Extended correlations of hysteresis and adhesion friction under wet and dry conditions for carbon black filled Solution-Styrene Butadiene Rubber on rough granite [21].

In Fig. 2.35, the simulation and experimental results for sliding of a carbon-black filled rubber over a rough granite surface as a function of velocities are compared from ref. [21]. It is quite evident that when the surface is wet with detergent containing water, there is no plateau as compared to dry friction which has a plateau over a wide range of velocities. Instead there is a single peak observed for wet surface at higher velocity. The adhesion component contributes to friction in dry conditions at low sliding velocities while the deformation/hysteresis component is a major component at higher velocities.

2.5.1.2 Tire Traction

Although there are no direct experiments related to tire materials in the following chapters, the physics of rubber friction is invariably applied to tire be-

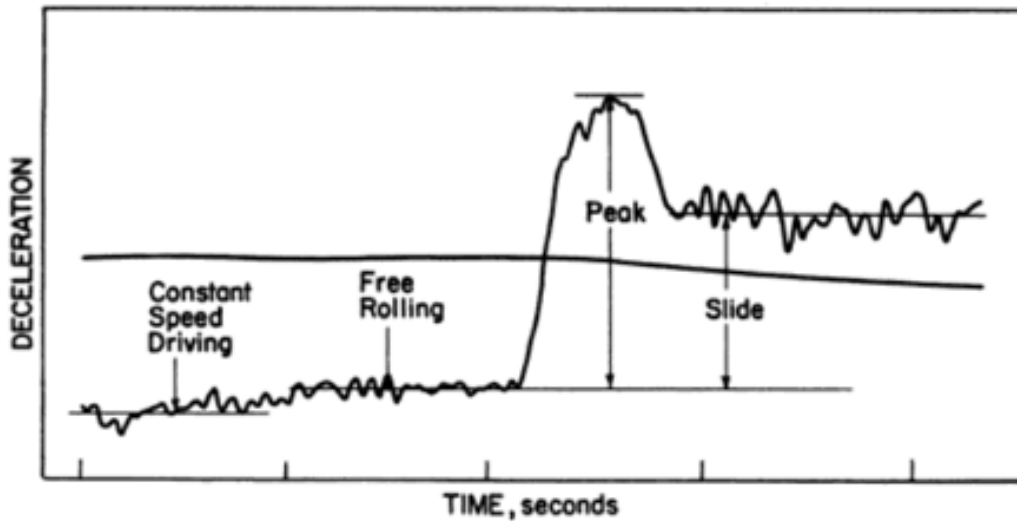


Figure 2.36: Time record of the deceleration of a car in a locked wheel braking experiment.

havior on road surfaces and all the concepts discussed so far in the background are relevant to tire mechanics. Furthermore, some of the theoretical and experimental developments in understanding tire behavior can help draw parallels to how elastomer bulk properties relate to interfacial adhesion and friction.

Since in the previous section we discussed observations from Grosch and Schallamach for rubber friction coefficient with varying velocities, let us first discuss some of the concepts they related from rubber friction to tire mechanics [131]. The friction coefficient in Fig. 2.29 as a function of velocities can be imagined as friction forces occurring during deceleration after application of brakes. The braking force rises with time, passes through a maximum and remains constant that is constant sliding. All these dynamic changes are a result of change in contact area whose origins are still not known for both dry and wet surfaces. It can be hypothesized that the contact area is full of Schallamach waves or in stick-slip regime during sliding which causes all the poor traction with road surfaces.

The above introductions to fundamental concepts of rubber friction would be useful in much of chapter 5 of this thesis.

CHAPTER III

EXPERIMENTAL

3.1 WATER CONTACT ANGLE

For any contact experiment the first and foremost important criterion is a check of surface energy. Water being of higher surface tension ($72 \text{ mJ}/\text{m}^2$), the contact angle formed between water and the surface can give an indication if the surface is 'hydrophilic' or 'hydrophobic'. In the context of adhesion and surface roughness, there are many aspects of contact angle that we would not deal with in this thesis however, as described in the section in background, the Young-Dupre equation can be used to extract the surface energy of the solid surface. Thus, we have used water contact angle to confirm the theoretical surface energies of the surfaces used in our experiments. A Drop Shape Analyzer (DSA) goniometer from Kruss was used for measuring contact angle and contact angle hysteresis. For static measurement, a $5 \mu\text{L}$ water droplet was formed on the surface and contact angle was measured through obtained images after 5 seconds of equilibration time. Advancing and receding measurements are done with the lowest possible volumetric speed using the goniometer i.e. $1\mu\text{L}/\text{min}$. The difference in advancing and receding contact angles is known as contact angle hysteresis (CAH).

3.2 FABRICATION OF SELF-ASSEMBLED MONOLAYERS

For the preparation of octadecyltrichlorosilane (OTS) (Gelest Inc.) monolayer on a silicon wafer obtained from Silicon Inc., the wafers were treated with piranha solution (3:7 ratio of 30% Hydrogen Peroxide: Sulfuric Acid (concentrated)). Silicon wafers are cleaned with an ample amount of water before use. The wafers are blown dry with nitrogen and plasma-treated before dipping in 1 wt.% OTS solution in toluene under nitrogen purge for 8 hours. The method described is similar to procedures from Defante et. al. and Tyrode et. al [132, 133]. The static water contact angle obtained was 110 ± 2 with negligible contact-angle hysteresis. The fluorinated dishes used in making PDMS lenses described below, were prepared by growing a monolayer of heptadecafluoro 1,1,2,2 tetrahydrodecatrichlorosilane (Gelest Inc.) on clean base-bath-treated borosilicate glass petri-dishes. Fluorination results into a static contact angle of 120 and the surface energy reported is about 7 mJ/m^2 that is lower than the surface energy of PDMS (about 22 mJ/m^2) [134, 135]. It is because of this difference in surface energy that a PDMS liquid or curing solution forms a contact angle on the fluorinated surface making it easier to cure as a hemispherical lens cap. The procedure is adopted from Vorvolakos et. al and Yurdumakan et. al [23, 52].

3.3 FABRICATION OF ROUGH DIAMOND SURFACES

Nanodiamond films (Advanced Diamond Technologies, Romeoville, IL) were deposited using a tungsten hot-filament chemical vapor deposition (HFCVD) system with parameters as described by Zeng et. al [136]. An H-rich gas mixture was used, with the chamber pressure of 5 Torr and a substrate temperature of

750C. The ratio of boron to carbon was maintained at 0.3 at%, to achieve high conductivity in the final film. The CH₄-to-H₂ ratio is modified (as described by Auciello et al. [137]) to tune the grain size: achieving microcrystalline diamond (MCD), nanocrystalline diamond (NCD), and ultrananocrystalline diamond (UNCD). All films were grown to a thickness of 2 microns. Chemical-mechanical planarization was performed on an undoped UNCD film to create the polished UNCD samples. Previous surface analysis of synthetically grown diamond surfaces have shown similar surface composition regardless of grain size [138–140].

3.4 FABRICATION OF SOFT ELASTIC POLYDIMETHYLSILOXANE (PDMS)

The smooth, soft elastic hemispheres were composed of cross-linked PDMS. To achieve systematic variation in modulus, we have used simple network theory, where changing the crosslinking molecular weight changes the cross-linking density and subsequently elastic modulus[22, 23],

$$E \sim \frac{\rho RT}{M_c}, \quad (3.1)$$

where E is the elastic modulus, ρ is the density of the polymer, R is the gas constant, T is the temperature in Kelvin and M_c is the cross-linked molecular weight. The curing system consisted of materials obtained from Gelest Inc., vinyl-terminated PDMS of different molecular weights M_w (DMS V-05 ($M_w=800$ gm/mol), V-21 ($M_w=9000$ gm/mol), V-31 ($M_w=28000$ gm/mol) and V-41 ($M_w=62700$ gm/mol)), tetrakis-dimethylsiloxysilane (SIT 7278.0) as tetra-functional cross-linker, platinum carbonyl cyclo-vinyl methyl siloxane complex

(SIP 6829.2) as catalyst, 1,3,5,7-tetravinyl-1,3,5,7-tetramethyl cyclo-tetra siloxane (SIT 7900.0) as inhibitor. The vinyl-to-hydride molar ratio of 4.385 was maintained for all the samples avoiding excess cross-linker evaporation to minimize adhesion hysteresis from unreacted side chains as reported by Perutz et al.[24]. The catalyst was added as 0.1% of the total batch. An additional reaction inhibitor was added to the DMS V-05 batch to avoid early cross-linking (5 times the catalyst amount). Hemispherical lenses were cast on the bottom of fluorinated glass dishes using a needle and a syringe. Since PDMS mixture has a higher surface energy than fluorinated surface, the drops form a contact angle on the surface giving a shape of a hemispherical lens. They were cured at 60 C for 3 days in a heating oven and Soxhlet-extracted using toluene at 124 C for 24 hours. After 12 hours of drying in open air the hemispheres were dried under vacuum at 120 C overnight. The sol fraction for all of the batches was found to be less than 5%. With similar synthesis procedure, we also casted about 1 mm thick PDMS sheets to test any change in surface energy as a consequence of varying elastic modulus. The water contact angle on these sheets was found to be very similar about 97 - 100, showing no practical change in surface energy.

3.5 DYNAMIC MECHANICAL ANALYSIS OF CROSS-LINKED PDMS

The bulk viscoelasticity analysis at different frequencies and temperatures were performed using a TA Instruments RSA Dynamic Mechanical Analyzer (DMA) over a range of temperatures ranging from -130C to 180C with 5C interval each and frequencies of 0.1 Hz to 100 Hz. For DMA measurements, about 1mm thick PDMS sheets were cast from the same mixture used for making lenses and

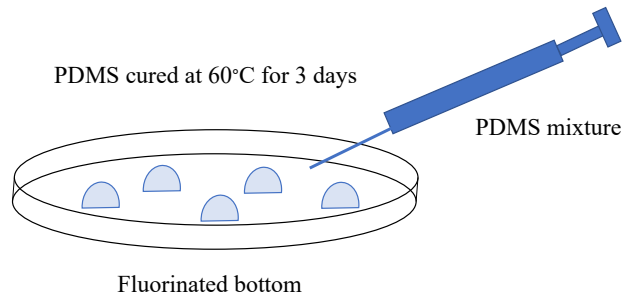
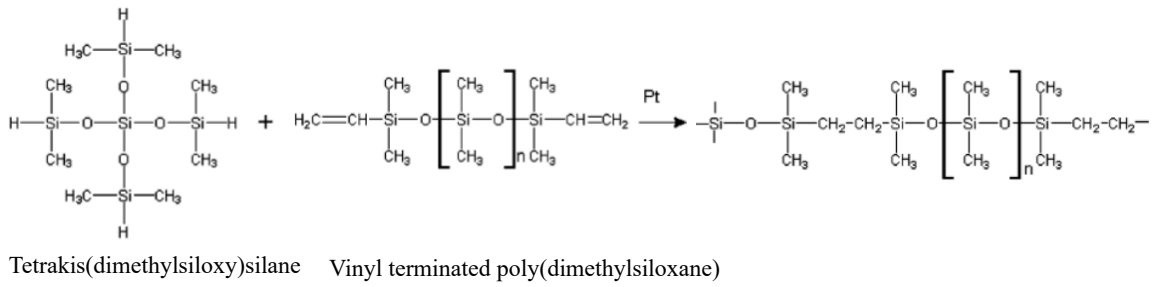


Figure 3.1: Casting procedure for elastic PDMS lenses inspired by works in refs. [22–24].

were Soxhlet extracted to remove unreacted PDMS and create networks similar in bulk to the lenses (as discussed in previous section). With the known dimensions of length, breadth and height before and after the application of various frequencies, the stress-strain curves and thus the storage, loss, complex modulus and other mechanical properties were easily obtained in tension fixture.

3.6 SURFACE TOPOGRAPHY CHARACTERIZATION

All of the work in this section related to roughness characterization and analysis is credited to Abhijeet Gujrati from Dr. Tevis Jacobs's lab at University of Pittsburgh, while the derivation for expression to calculate topographical area is credited to Dr. Lars Pastewka from University of Freiberg, Germany.

3.6.1 LARGE-SCALE TOPOGRAPHY CHARACTERIZATION: STYLUS PROFILOMETRY

The largest scales of topography were measured using one-dimensional line scans with a stylus profilometer (Alpha Step IQ, KLA Tencor, Milpitas, CA) with a 5- μm diamond tip. Data were collected at a scanning speed of 10 $\mu\text{m}/\text{s}$, with data points every 100 nm. A total of 8 measurements were taken on each substrate, with 2 measurements each at scan sizes of 0.5, 1, 2, 5 mm. These measurements were taken at random orientations of the sample and did not show meaningful variations with direction. A parabolic correction was applied to all measurements which removed the tilt of the sample and the bowing artifact from the stylus tool. In two sessions (for the UNCD and polished UNCD), the larger scan sizes exhibited consistent non-parabolic trends due to instrument artifacts. In these cases, this was corrected by performing reference scans on polished silicon wafers and subtracting the averaged profiles from the reference measurements. Representative scans of stylus profilometry for all four materials are shown in Fig. 3.2 below.

3.6.2 MID-SCALE TOPOGRAPHY CHARACTERIZATION: ATOMIC FORCE MICROSCOPY

The substrates were measured using an atomic force microscope (AFM) (Dimension V, Bruker, Billerica, MA) in tapping mode with diamond-like carbon-coated probes (Tap DLC300, Mikromasch, Watsonville, CA). For all substrates, square measurements were taken with the following lateral sizes: 3 scans each at 100 nm, 500 nm, and 5 μm ; 1 scan each at 250 nm and 1 μm . The scanning speed was maintained at 1 $\mu\text{m}/\text{s}$ for all scans. Each scan had 512 lines, with 512 data

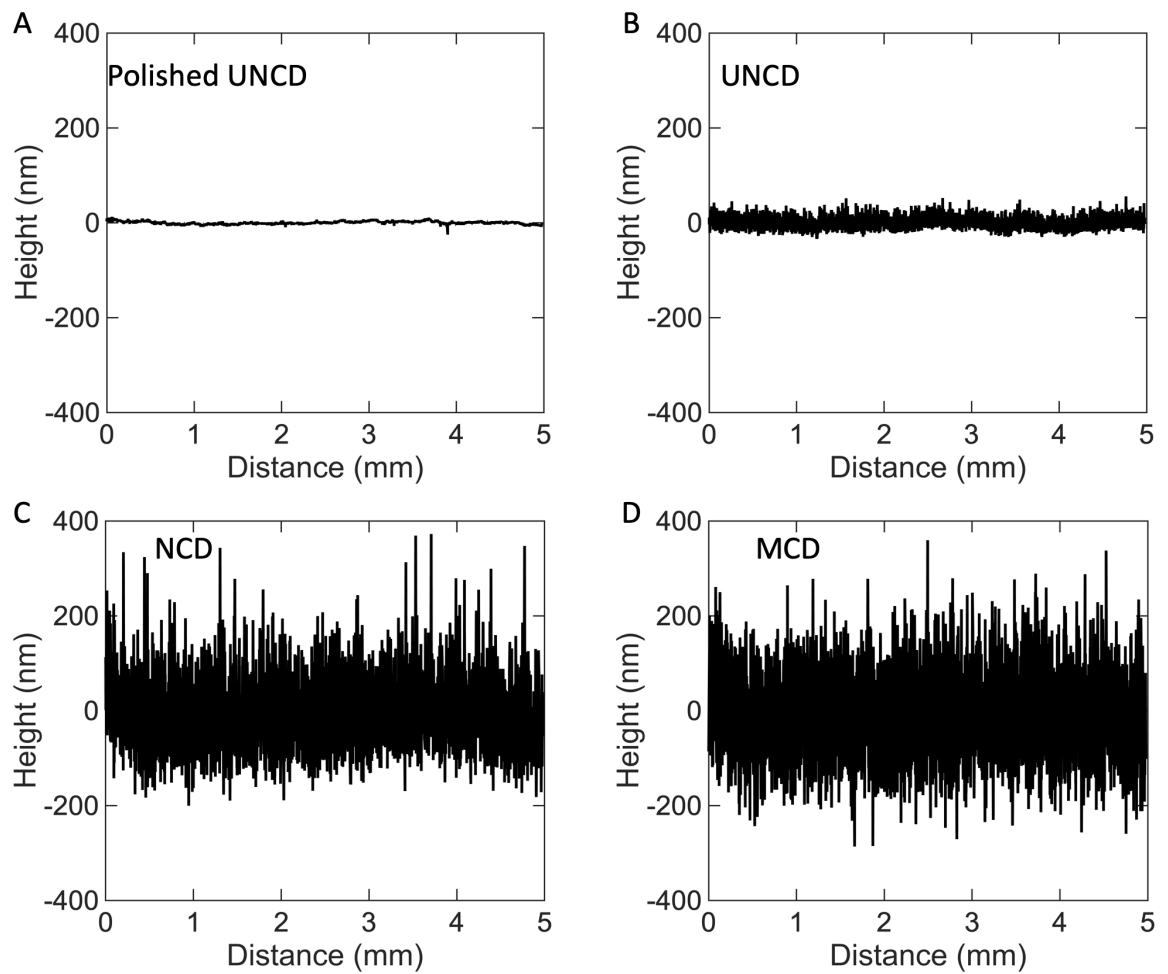


Figure 3.2: Stylus profilometry of the polished UNCD (A), UNCD (B), NCD (C) and MCD (D).

points per line, corresponding to pixel sizes in the range of 0.2 to 98 nm. The values of free-air amplitude and amplitude ratio were kept in the range of 37 to 49 nm and 0.15 to 0.3, respectively. While AFM provides a two-dimensional map of surface topography, the data were analyzed as a series of line scans, both to facilitate direct comparison with other techniques and to avoid apparent anisotropy due to instrument drift. Representative scans of atomic force microscopy for all four materials are shown in the Fig. 3.3 below.

3.6.3 SMALL-SCALE TOPOGRAPHY CHARACTERIZATION: TRANSMISSION ELECTRON MICROSCOPY

Topography was measured on scales from microns to Angstroms following the approach developed in Ref. [141]. For the UNCD, NCD, and MCD, the "wedge deposition technique" was used, whereas for polished UNCD, the "surface-preserving cross-section technique" was used [141]. Briefly, the wedge deposition technique involves depositing the film of interest, in the same batch, on both flat silicon wafers (used for adhesion testing) and on standardized TEM-transparent silicon wedge samples (for TEM imaging). The surface-preserving cross-sectioning technique is similar to conventional techniques for extraction of a TEM cross-section from a bulk sample (using grinding, polishing, dimple-grinding, and ion etching); however, modifications to the ion etching step ensure that the original surface topography is unmodified from its original state. The samples were imaged using a TEM (JEOL JEM 2100F, Tokyo, Japan) operated at 200 keV. The images were taken with a 2000x2000-pixel camera using magnification levels from 5000x to 600,000x.

The nanoscale surface contours were extracted from the TEM images using custom Matlab scripts that create a digitized line profile based on a series of points selected by the user. The TEM images obtained were first rotated to make the surface horizontal and then the outer-most boundary was traced. While the vast majority of the measured surface were well-behaved functions (i.e., there was a single value of height (y-axis) for each horizontal position (x-axis), there were some cases where two adjacent points were captured with identical or decreasing horizontal position, the latter point was removed. In just 12 out of the 210 measurements, there were small portions of the profile that were reentrant. This character is not necessarily physically meaningful as it depends on the rotation of the TEM image during image analysis. Because the mathematical analyses require well-behaved functions, these regions were excluded from analysis.

3.6.4 COMBINATION OF ALL MEASUREMENTS INTO COMPLETE, MULTI-SCALE PSD CURVES

The combined PSD describing a surface is computed as the arithmetic average of all of the individual PSDs. For the tip-based measurement techniques, the tip-radius artifacts [142, 143] were eliminated using the criterion described in Eq. 2 of Ref. [2]. PSD data for wavevectors above this cutoff were eliminated as unreliable. For every topography measurement, the power spectral density was computed using the conventions described in Refs. [2, 142]. The line scans from stylus profilometry, atomic force microscopy, and transmission electron microscopy all yield descriptions of the height $h(x)$ over lateral position x . The Fourier transform of the surface topography is given by,

$$\tilde{h}(q) = \int_0^L h(x)e^{-iqx} dx. \quad (3.2)$$

The PSD is computed as the square of the amplitude of $\tilde{h}(q)$; i.e.,

$$C(q) = L^{-1}|\tilde{h}(q)|^2. \quad (3.3)$$

Since all collected data was analyzed as 1D line scans, then the computed PSDs were of the form of C_{1D} , using the nomenclature of Ref. [2]. All topography measurements in the present investigation are analyzed as 1D line-scans, and therefore the 1D PSD is presented in Fig. 3.3. However, the calculations proposed by Persson and Tosatti (and their modifications) employ a two-dimensional isotropic PSD. Under the assumption of isotropic roughness, the 2D PSD can be calculated from the 1D PSD, as described in Ref. [2]. For this, we use Eq. A.28 of Ref. [2]:

$$C^{iso}(q) \approx \frac{\pi}{q\sqrt{1 - (\frac{q}{q_s})^2}} C^{1D}(q), \quad (3.4)$$

where q_s is the short wavelength cut-off, in this case defined by the minimum wavelength at which roughness is measured (4 Å). This form of the 2D PSD is shown in Fig. 3.4 and is used in the calculations for stored elastic energy and true surface area.

3.6.5 CALCULATION OF SCALAR ROUGHNESS PARAMETERS

The power spectral density can be integrated (as described in Refs. [2, 142]) to compute scalar descriptions of the surface: the root-mean-square height h_{rms} , RMS slope h_{rms} , and RMS curvature h_{rms} . The value of these parameters will depend on the scale over which they are measured [142]; including all scales of topography yields the values shown in the table below,

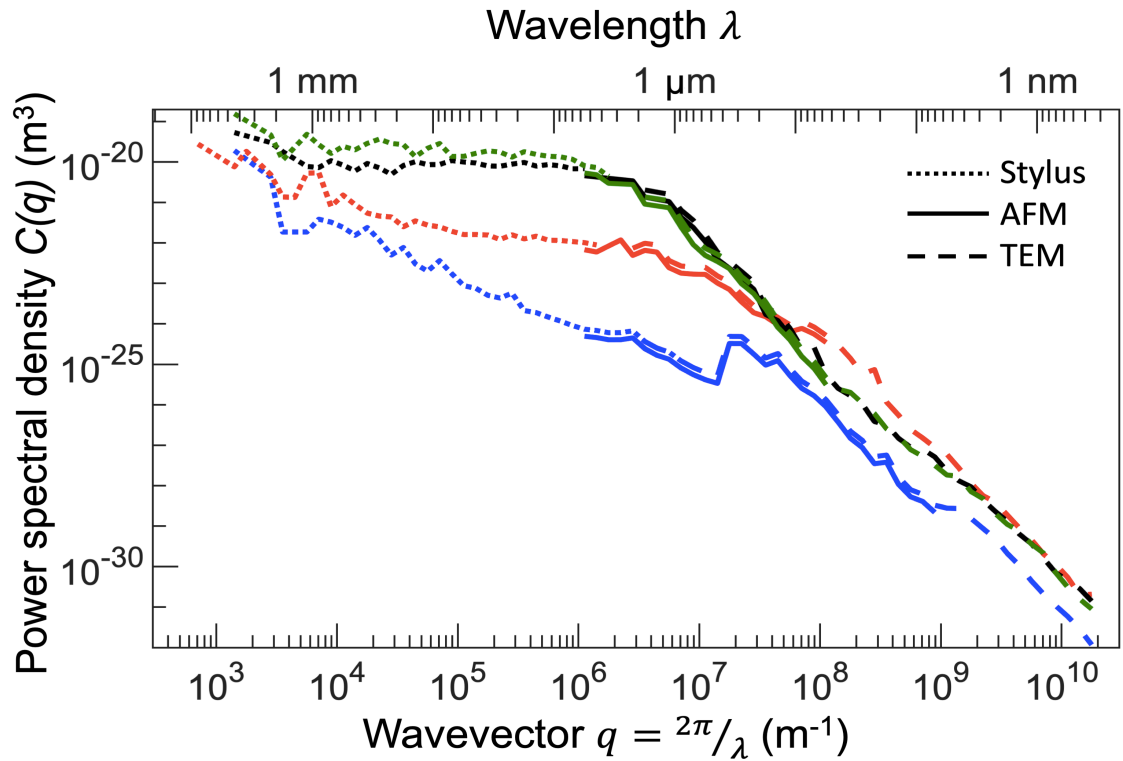


Figure 3.3: Power spectral densities of the four surfaces, with indication of the specific regimes of applicability of each technique. The present figure uses line style (solid, dashed, dotted) to indicate the specific bandwidth over which different techniques were applied. Because of the nature of tip artifacts, the minimum size from stylus and AFM data differ between surfaces.

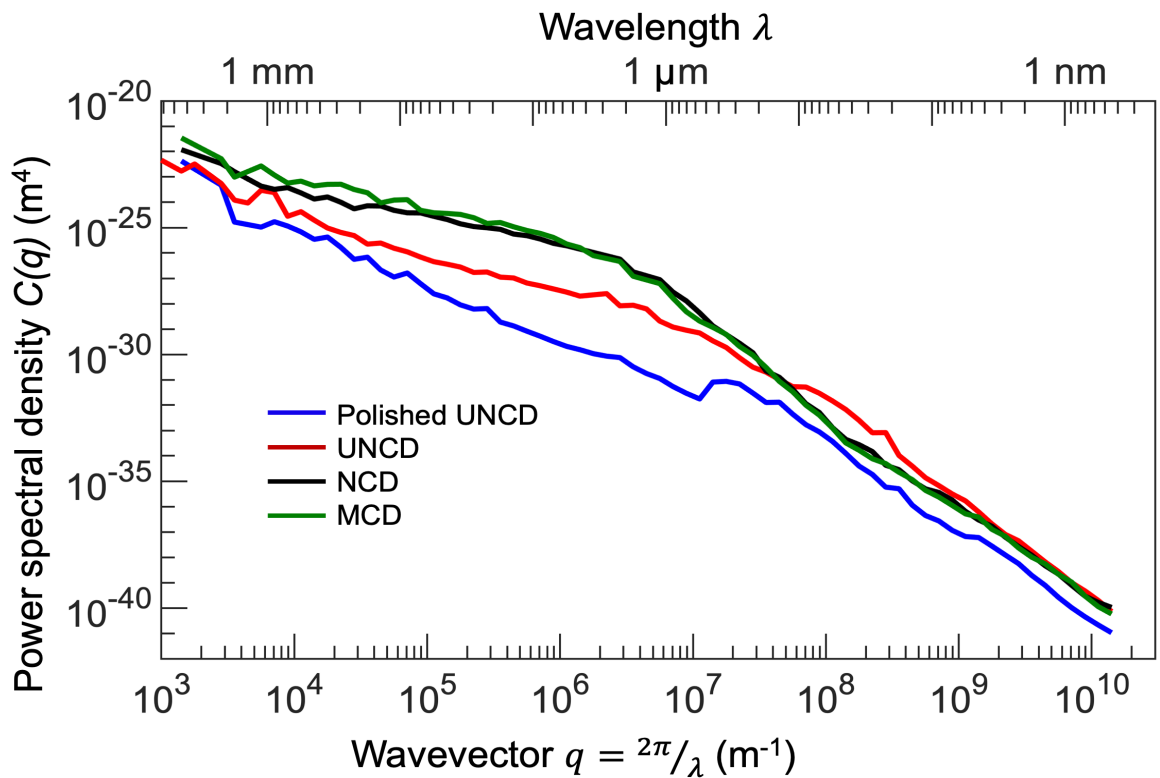


Figure 3.4: 2D power spectral densities, after conversion from the 1D values

Table 3.1: Roughness parameters (2D) of the nanodiamond substrates

Parameter	Polished UNCD	UNCD	NCD	MCD
RMS Height (nm)	4.6±0.8	23.4±1.3	121.7±13.4	126.6±8.2
RMS Slope	0.39±0.04	1.46±0.36	1.15±0.13	1.07±0.13
RMS Curvature (nm ⁻¹)	1.13±0.23	3.37±0.69	3.19±1.15	2.83±0.81

3.6.6 DERIVING AN EXPRESSION FOR THE INCREASE IN SURFACE AREA DUE TO ROUGHNESS FOR LARGE SLOPES

Prior work (e.g. Ref. [13]) has derived expressions for A_{true}/A_{app} in the limit of small slopes. Here, we derive an expression for A_{true}/A_{app} that works for arbitrary values of slope h'_{rms} . The derivation follows along the arguments given in the Supplementary Material of Ref. [142]. For a full two-dimensional topography map $h(x,y)$, the surface area A_{true} is straightforwardly obtained from an expression analogous to the arc length of a function:

$$A_{true} = \int_{A_{app}} \sqrt{1 + |\nabla h|^2} dx dy = A_{app} \sqrt{1 + \left(\frac{\partial h}{\partial x}\right)^2 + \left(\frac{\partial h}{\partial y}\right)^2} dx dy. \quad (3.5)$$

For small slopes $|\nabla h|$, the square-root can be expanded into a Taylor Series and truncated above quadratic order. This gives the well-known expression [13]:

$$A_{true} = \int_{A_{app}} \left(1 + \frac{1}{2}|\nabla h|^2\right) dx dy = A_{app} \left(1 + \frac{1}{2}h'_{rms}\right), \quad (3.6)$$

with

$$h'_{rms} = \int_{A_{app}} |\nabla h|^2 dx dy. \quad (3.7)$$

In order to arrive at an expression valid for large h'_{rms} , we now transform the integral over the surface area into an integral over slopes. We first define the slope distribution function,

$$\Phi(S_x, S_y) = \frac{1}{A_{app}} \int_{A_{app}} \delta(S_x - \frac{\partial h(x, y)}{\partial x}) \delta(S_y - \frac{\partial h(x, y)}{\partial y}) dx dy, \quad (3.8)$$

where δx is the Dirac delta function. Note that using the slope distribution function, we can express the integral over any function 'f' that depends on just slopes as

$$\int_{A_{app}} f(\frac{\partial h}{\partial x}, \frac{\partial h}{\partial y}) dx dy = A_{app} \int \Phi(S_x, S_y) f(S_x, S_y) dS_x dS_y. \quad (3.9)$$

We can hence re-express Eq. 3.5 as:

$$\frac{A_{true}}{A_{app}} = \int \Phi(S_x, S_y) \sqrt{1 + S_x^2 + S_y^2} dS_x dS_y. \quad (3.10)$$

We now make the assumption that our surfaces are isotropic and Gaussian. The slope distribution function is then given by

$$\Phi(S_x, S_y) = \frac{1}{\pi h'_{rms}} \exp(-\frac{S_x^2 + S_y^2}{h'_{rms}}), \quad (3.11)$$

with (see also Eq. 3.7)

$$h'_{rms} = \int_{A_{app}} |\nabla h|^2 dx dy = \int \Phi(S_x, S_y) (S_x^2 + S_y^2) dS_x dS_y. \quad (3.12)$$

Evaluating Eq. 3.8 using this slope distribution function yields,

$$\frac{A_{true}}{A_{app}} = \frac{2}{h'_{rms}} \int_0^\infty \exp(-\frac{S^2}{h'_{rms}}) \sqrt{1 + S^2} S dS = 1 + \frac{1}{2} h'_{rms} g(h'_{rms}), \quad (3.13)$$

with

$$g(h'_{rms}) = \sqrt{\pi} \exp(\frac{1}{h'_{rms}}) \operatorname{erfc}(\frac{1}{h'_{rms}}) / h'_{rms}. \quad (3.14)$$

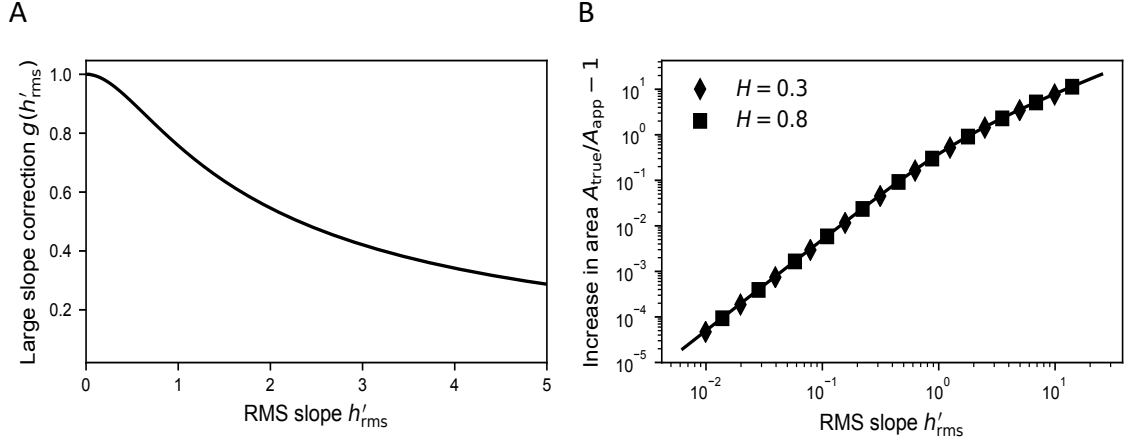


Figure 3.5: Plot of the correction $g(h'_{rms})$ to the small-slope approximation. For values of $g(h'_{rms}) \approx 1$ the small slope approximation is valid (A) Validation of Eq. 3.13 using computer-generated self-affine surfaces with varying RMS slope h'_{rms} and Hurst exponents H (B) The solid line shows the analytic result given by Eq. 3.13.

Note that the left-hand side of Eq. 3.13 is essentially Eq. B1 from Ref. [13]. The function $g(h'_{rms})$ can be regarded a correction to the small slope approximation Eq. 3.11. It has the property $g(h'_{rms}) \rightarrow 1$ as $h'_{rms} \rightarrow 0$ and hence we recover Eq. 3.11 from Eq. 3.18 in the small slope limit. Fig. 3.5 shows the function g up to slope of 5. Note that for slope of order unity, $g(1) \approx 0.76$ and hence the small slope approximation Eq. 3.6 would overestimate the area by 30%.

In order to numerically test the validity of Eq. 3.13, we have created a range of synthetic self-affine surfaces with 4096×4096 points and Hurst exponent $H = 0.3$ and 0.8 using a Fourier filtering algorithm [2, 144]. We then computed the true surface area by numerical integration of Eq. 3.5. Figure 3.5B shows that the analytic expression Eq. 3.13 describes the synthetic surfaces excellently up to slopes of the order 10.

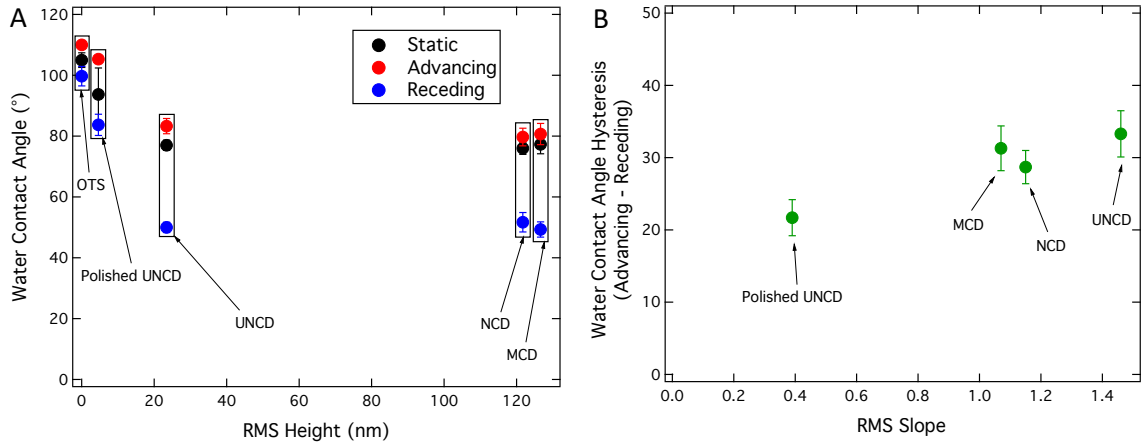


Figure 3.6: A. The comparison of static and advancing and receding angles for the smooth OTS coated silicon wafer and nanodiamond surfaces. As the roughness increases there is a decrease in static angle while the difference in advancing and receding is increased. B. shows the difference plotted as contact angle hysteresis (CAH) as a function of RMS slope for the surfaces.

3.7 CONTACT ANGLE AND CONTACT ANGLE HYSTERESIS OF NANODIAMOND

Fig. 3.6A depicts the static, advancing and receding contact angles for the rough four diamond surfaces in comparison with smooth OTS-coated silicon wafer. It is seen clearly that the smooth OTS and polished UNCD have a higher static contact angle as well as smaller hysteresis. While in case of surfaces with higher roughness namely UNCD, NCD and MCD there is a decrease in static contact angle and larger hysteresis. Given the chemical composition of diamond surfaces is similar, the observed contact angle and CAH is a result of surface roughness. For now these results show that the liquid water might form Wenzel state over the surface. In Fig. 3.6B, where we plot the hysteresis with RMS slope, we see that as the slope increases the CAH increases. However, it is not a linear dependence. The following results corroborate well with the adhesion results and further discussions in Chapter 4.

3.8 ADHESION MEASUREMENTS USING JKR-BASED SETUP

The contact experiment for each hemisphere-substrate combination was carried out using the setup shown in Fig. 3.7 where simultaneous force and contact area measurement were taken during loading and unloading. Optically transparent PDMS hemispheres of 2-3 mm diameter and height greater than 700 μm were used to avoid substrate effects from the hemisphere's sample mount [145, 146]. The maximum load applied for every measurement was 1 mN and the cycle was completed with a constant velocity of 60 nm/sec.

3.8.1 CONTACT EXPERIMENT ANALYSIS: EXTRACTING VALUES OF WORK OF ADHESION

To extract the apparent work of adhesion, the loading data is fit to the JKR equation. Since the contact radius, applied force, and radius of the lens R are known, then the apparent work of adhesion and elastic modulus can be computed.

3.8.2 TESTING PDMS FOR ADHESION HYSTERESIS

Before measuring work of adhesion on the rough nanodiamond substrates, the PDMS hemispheres were tested for inherent hysteresis against a low surface-energy OTS monolayer-coated smooth silicon-wafer surface. The work of adhesion values obtained for loading and unloading fits are listed in table 3.2 showing comparable values and low hysteresis. This OTS reference testing was repeated before and after the measurements on the nanodiamond substrates to rule out any permanent changes in the cross-linked structure of PDMS due to testing. The elastic moduli are calculated using the Poisson's ratio for elastomers as 0.5, and the values are comparable to Ref. [23].

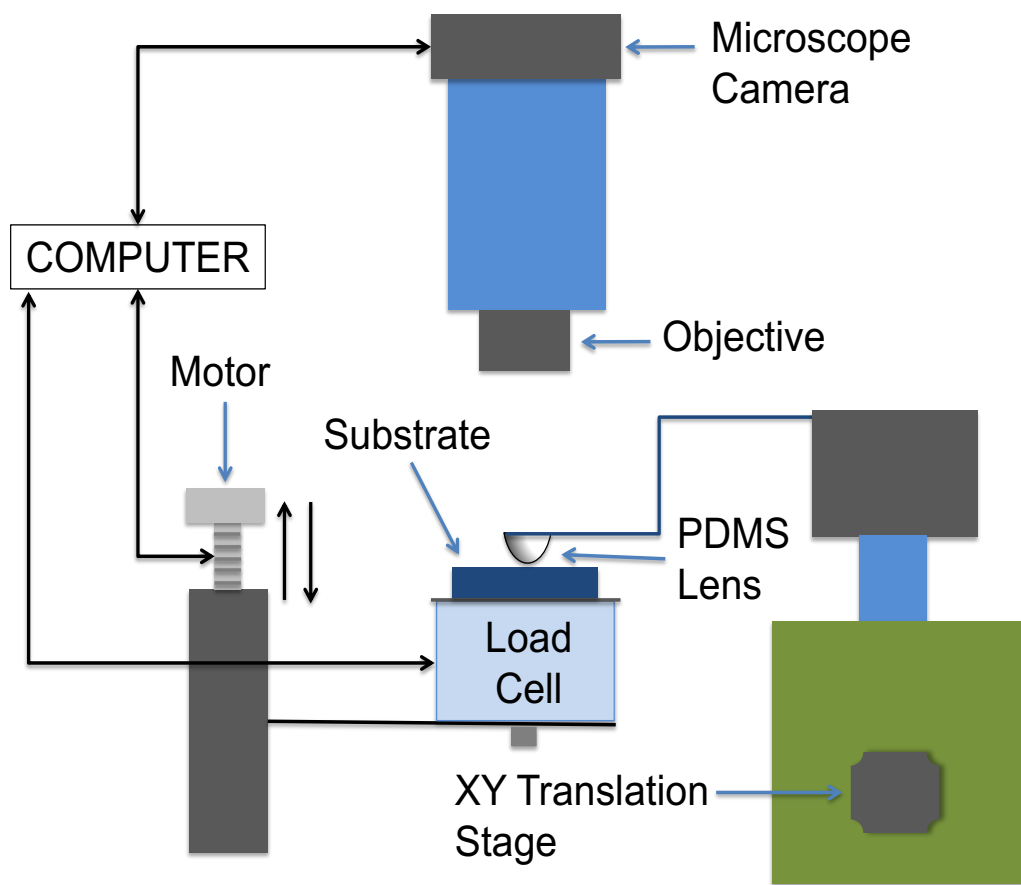


Figure 3.7: Schematic of the JKR apparatus.

Table 3.2: PDMS-OTS contact with JKR Analysis for four different moduli

M. wt. (gm/mol)	Elastic Modulus (MPa)	W(Loading) (mJ/m ²)	W(Unloading) (mJ/m ²)	Hysteresis (mJ/m ²)
800	10.0±0.9	51.0±4.8	56.4±1.8	3.4±6.2
9000	1.9±0.1	38.8±2.9	52.2±1.3	13.36±1.6
28000	1.0±0.0	36.8±0.8	52.5±4.8	15.7±4.4
62700	0.7±0.0	39.6±1.2	59.3±1.0	19.6±1.9

3.9 FRICTION MEASUREMENTS USING CANTILEVER SETUP

We have used two different diamond rough surfaces and four different elastic moduli for friction measurements. The friction measurements were done using velocities in the range nm/sec to m/sec using a nano-stepper motor (NewFocus) and a Servo Motor (Moog Animatics SM). With help of threads of different sizes attached to the motors we were able to cover the whole range of sliding velocities (Fig. 3.8). A normal load of 5mN was used throughout the measurement by a displacement-control motor. With the help of cantilever springs on which a PDMS lens is attached we could measure the shear force and with the corresponding observed, focused contact area through high speed camera on a microscope (Photron FASTCAM SA-04 camera attached to Olympus microscope), we can obtain the shear stress where $\sigma=F/A$. The contact areas were analyzed using an edge detection function in MATLAB with certain modification in the code to incorporate calibration and image contrast.

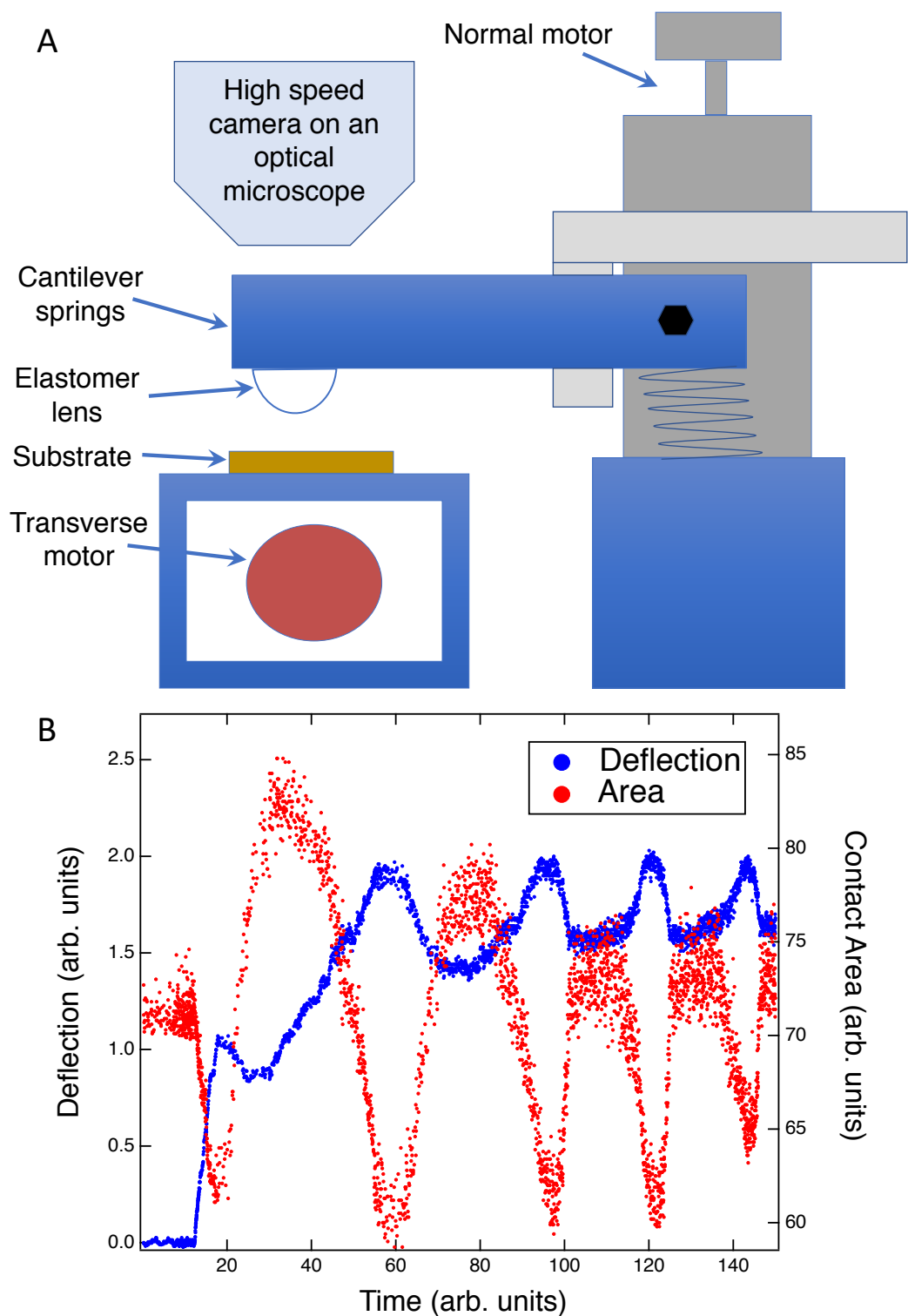


Figure 3.8: Schematic of the home built setup for measuring friction (A) showing simultaneous capture of friction force (from spring deflection and known spring constant) and contact area (from high speed camera). The frames analyzed through deflection tracking and edge detection are plotted as a function of time (B) were the raw data gives the apparent shear stress from force/area.

CHAPTER IV

LINKING ENERGY LOSS IN SOFT ADHESION TO SURFACE ROUGHNESS

To understand the dependence of adhesion on roughness, we performed in situ measurements of the load-dependent contact of sixteen different combinations of soft spheres and rough substrates. We have chosen PDMS as our elastomer and synthetically grown hydrogen-terminated diamond for hard rough surfaces because both have low surface energies. The choice of these two surfaces eliminates the possibility of adhesion hysteresis as a result of specific bonding [52, 53]. We used a recently developed approach to characterize the surface topography of four different nanodiamond substrates across eight orders of magnitude of size scale, including down to the Ångström-scale. More than 50 individual topography measurements were made for each substrate using transmission electron microscopy, atomic force microscopy, and stylus profilometry. Results were combined to create a single power spectral density for each surface that comprises a comprehensive description of topography at all scales. The PDMS hemispheres were loaded under displacement control to a maximum load of 1 mN before unloading to separation. Real-time measurements were made of contact radius, load, and displacement.

The apparent work of adhesion during approach W_{app} is extracted by using the JKR model to fit the measured contact radius a as a function of applied load. This yields a different value of apparent work of adhesion for each of the sixteen contacts. The surface chemistry of the PDMS and the nanodiamond is ex-

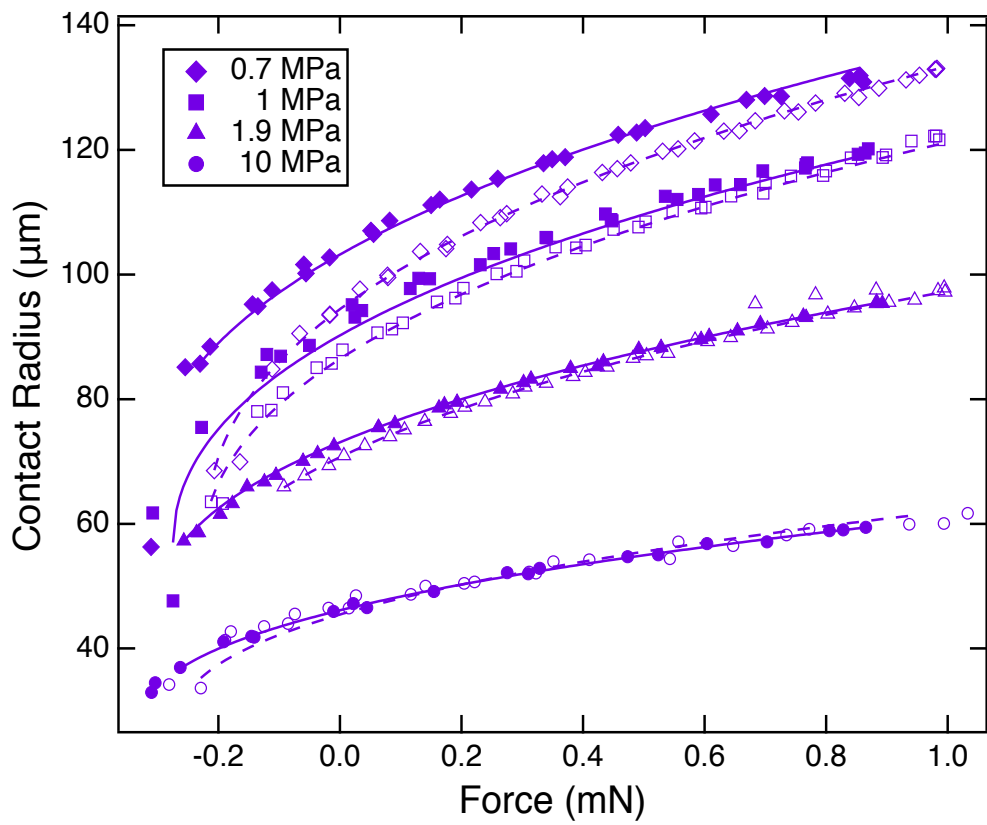


Figure 4.1: The contact radius data for the PDMS hemispheres on the OTS surface show low hysteresis between loading (empty symbols) and unloading (filled symbols). The dashed lines indicate JKR model fits for loading and solid lines indicate the JKR model fits for unloading.

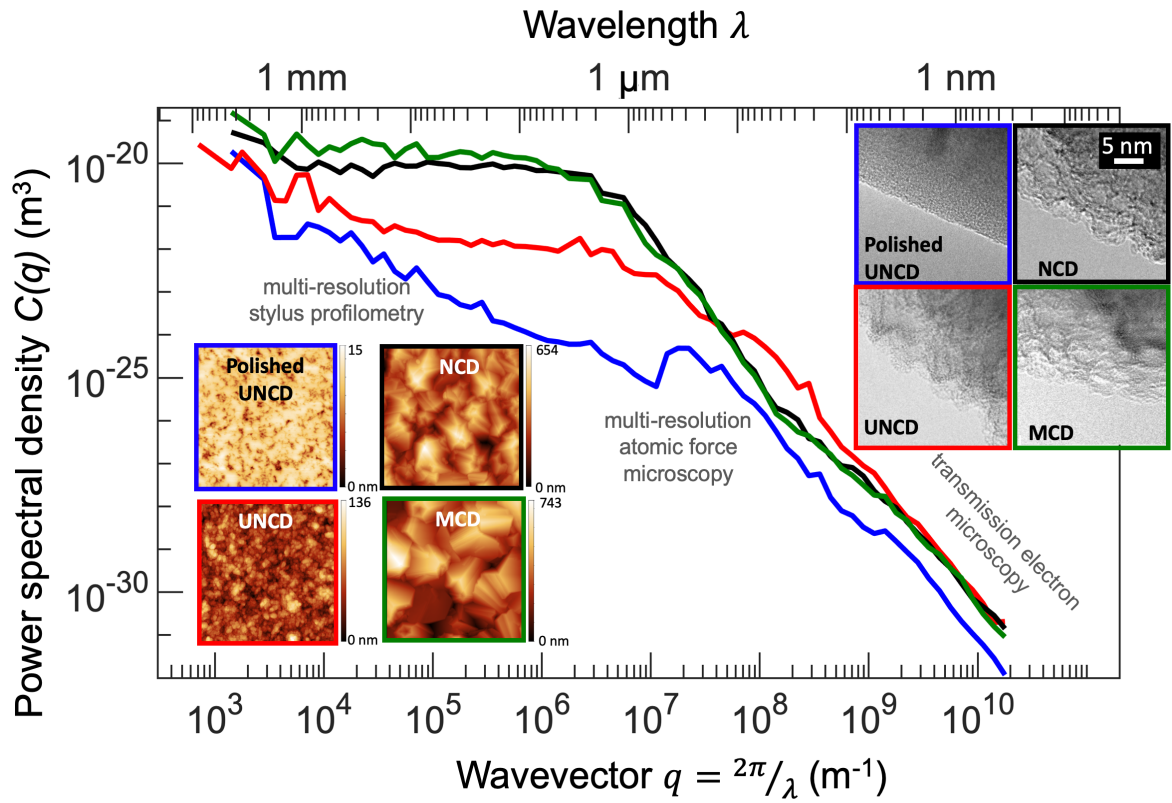


Figure 4.2: Comprehensive topography characterization for four rough nanodiamond surfaces. The surface topography was measured using a multi-resolution approach that combines transmission electron microscopy (rightmost region of the curves), atomic force microscopy (intermediate region), and stylus profilometry (leftmost region). The nanodiamond surfaces are designated using the following nomenclature: ultrananocrystalline diamond (UNCD) is shown in red; nanocrystalline diamond (NCD) in black; microcrystalline diamond (MCD) in green, and a polished form of UNCD (polished UNCD) in blue. AFM images (of 5-micron lateral size) are shown in the left inset; TEM images are shown in the right inset. More than 50 measurements for each surface are combined using the power spectral density, which reveals the contribution to overall roughness from different length scales (wavelengths). These comprehensive descriptions of surface topography enable the determination of true surface area and stored mechanical energy due to the topography, which are necessary to understand adhesion.

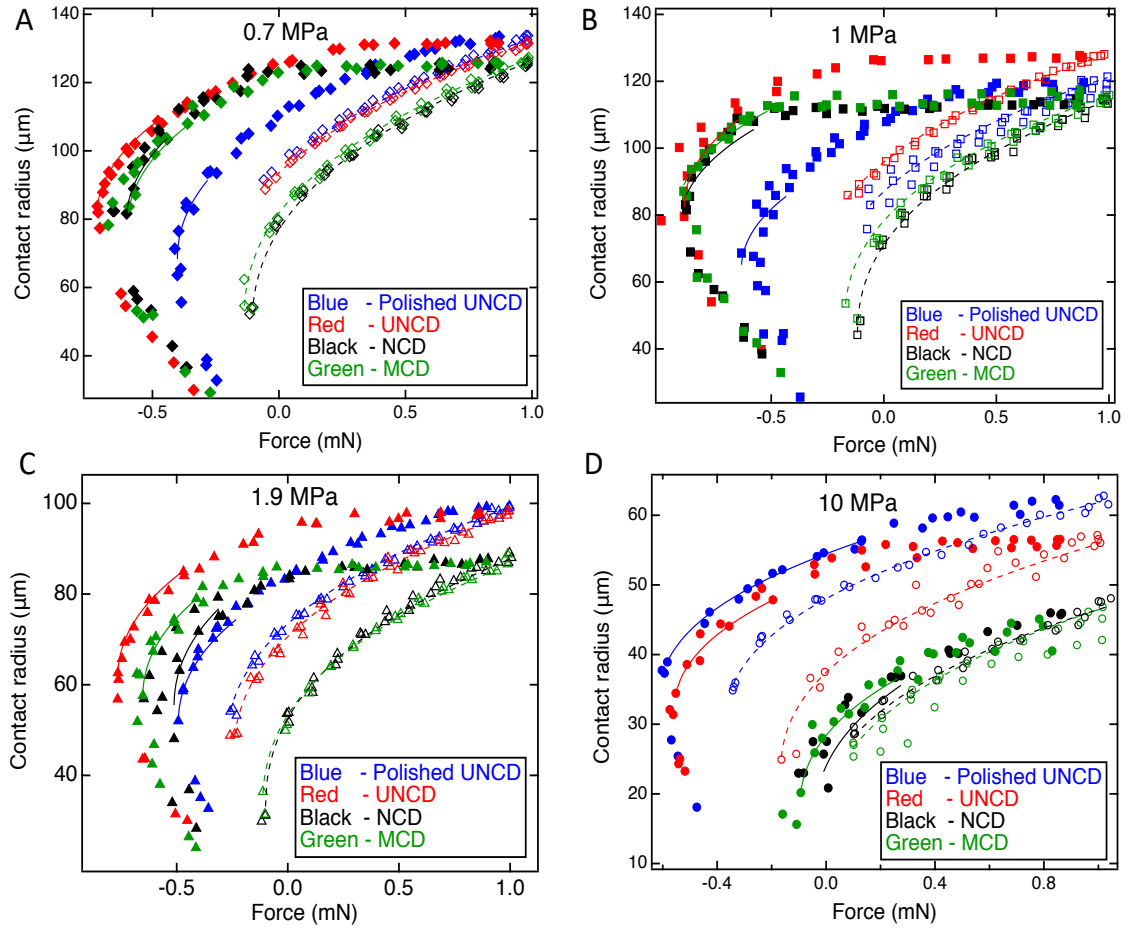


Figure 4.3: Contact radius was measured as a function of applied force plots for PDMS spheres with elastic modulus of 0.7 MPa (A), 1 MPa (B), 1.9 MPa (C), and 10 MPa (D). The loading data are represented using hollow symbols and are fit using Eq. 1 (dashed line) to extract the apparent work of adhesion W_{app} . The separation data are represented using filled symbols; a subset of the data are fit using Eq. S1 (solid line) to extract $W_{app,ret}$.

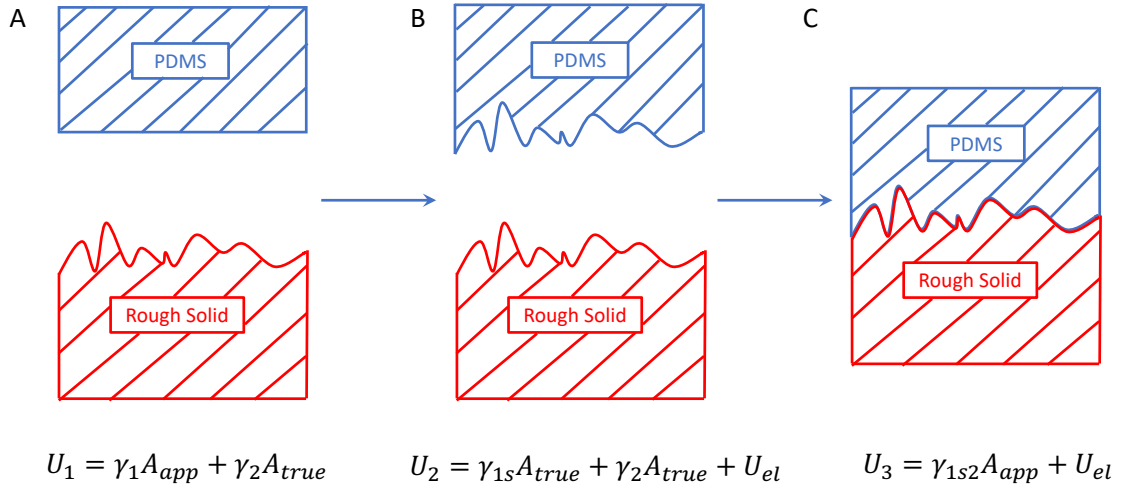


Figure 4.4: During adhesion, the materials go from the initial state (left) to the final state (right). However, to fully account for the energy change, one must consider the change in area of the soft material, which is represented schematically by including the intermediate state (middle).

pected to be similar in all cases, therefore all contacts should have approximately the same value of W_{int} . Before testing the hemispheres with rough surfaces, they were tested against a smooth silicon wafer coated with a low-surface energy octadecyltrichlorosilane (OTS) monolayer to verify that there is negligible adhesion hysteresis due to viscoelasticity (Fig. 4.1). To analyze the dependence of W_{app} on modulus and multi-scale surface topography, we use a model of conformal contact, based on Persson and Tosatti. Those authors postulated that the product of W_{app} and A_{app} (the apparent or projected area) is given by a balance of adhesive energy and stored elastic energy U_{el} :

$$W_{app} A_{app} = W_{int} A_{true} - U_{el}, \quad (4.1)$$

with $W_{int} = \gamma_1 + \gamma_2 - \gamma_{12}$, where γ_1 and γ_2 are the surface energies of the soft and hard surfaces, respectively, and γ_{12} is the interfacial energy between them. The term A_{true} is the true surface area of the rough hard surface. However, Eq. 4.1 makes

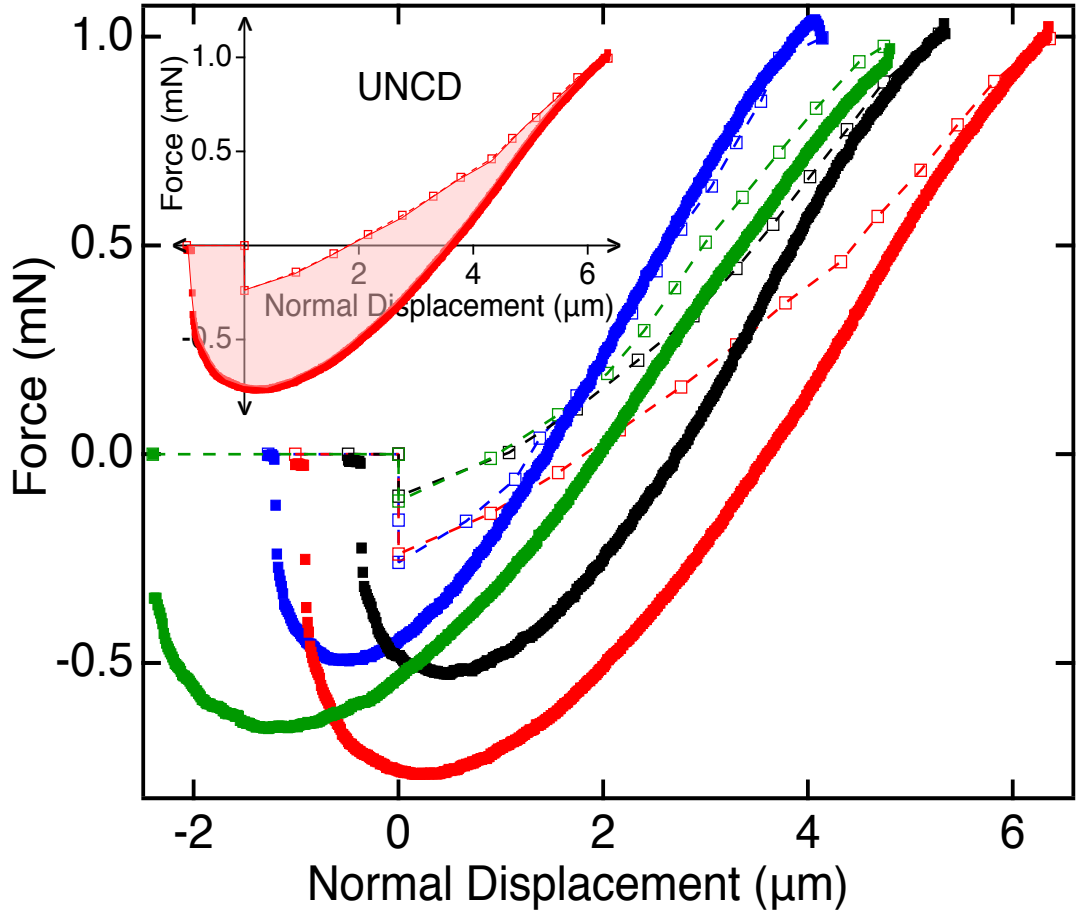


Figure 4.5: Adhesion measurements during approach and retraction. Loading and adhesion tests were performed with ultra-smooth PDMS hemispheres of varying stiffness from 0.7 to 10 MPa. Representative curves from one material (with $E=1.9$ MPa) are presented in this figure. The load-dependent contact radius (A) was measured using in situ optical microscopy. The apparent work of adhesion upon approach W_{app} was extracted by fitting the loading data (hollow points) using the JKR model (dashed lines). The force-displacement curves (B) were used to calculate the energy loss E_{loss} during contact by performing a closed-circuit integral (inset). Both approach and retraction experiments were conducted at a very low speed, 60 nm/s.

two important assumptions that must be addressed: it neglects the change in area of the soft elastomer surface from A_{app} to A_{true} upon contact; and it assumes that the surface energy of the soft material is independent of strain. These two assumptions can be corrected by modifying the energy balance to explicitly include the work done in increasing the surface area of the elastomer.

The Persson-Tosatti energy balance implicitly implies that the area of the PDMS surface does not change. While this may be valid for small-slope surfaces, in the more general case the area will increase from A_{app} to A_{true} , as shown schematically in Fig. 4.4.

To go from the initial state (Fig. 4.4A) to the intermediate state (Fig. 4.4B), there is an energy change from U_1 to U_2 . The PDMS is stretched and its surface energy changes depending upon the applied strain, which can be represented as a function of the area:

$$U_{1-2} = \int_{A_{app}}^{A_{true}} \gamma_1(A) dA + U_{el}. \quad (4.2)$$

Then, the energy to go from the intermediate state U_2 to the final state U_3 (Fig. 4.4C), there is an energy change of:

$$U_{2-3} = (\gamma_{1s2} - \gamma_{1s} - \gamma_2) A_{true}. \quad (4.3)$$

The total work to go from the initial state to the final state is equal to $\Delta U_{1-2} + \Delta U_{2-3}$:

$$\Delta U_{1-3} = \int_{A_{app}}^{A_{true}} \gamma_1(A) dA + U_{el} + (\gamma_{1s2} - \gamma_{1s} - \gamma_2) A_{true}. \quad (4.4)$$

This is the total energy change equal to $-A_{app}W_{app}$. Finally, we can re-write the total energy balance as:

$$W_{app}A_{app} = W_{int}^*A_{true} + \int_{A_{app}}^{A_{true}} \gamma_{1s}(A)dA - U_{el}, \quad (4.5)$$

where, $W_{int}^* = \gamma_{1s} + \gamma_2 - \gamma_{1s2}$, where γ_{1s} is the surface energy of the stretched elastomer. If we now make the assumption that the surface energy of the soft elastomer is not a strong function of strain [6], then $W_{int}^* = W_{int}$ and we can simplify the energy balance, and rearrange it to explicitly show W_{app} as a function of two roughness-dependent terms, A_{true}/A_{app} and U_{el}/A_{app} :

$$W_{app} = W_{int}^* \frac{A_{true}}{A_{app}} - \gamma_1 \left(\frac{A_{true}}{A_{app}} - 1 \right) \gamma_{1s} - \frac{U_{el}}{A_{app}}. \quad (4.6)$$

The stored elastic strain energy can be calculated from the power spectral density using the approach of Persson and Tosatti [13]:

$$\frac{U_{el}}{A_{app}} = \frac{E^*}{8\pi} \int_0^\infty q^2 C^{iso}(q) dq, \quad (4.7)$$

where C^{iso} is the radial average of the two-dimensional power spectral density. For calculating the power spectral density, we follow the conventions used in Ref. [2]. C^{iso} is calculated from the one-dimensional PSD (Fig. 4.2) as described in Chapter 3. Finally, we derived an equation for the roughness-dependent increase in surface area, which works for arbitrary values of root-mean-square surface slope h'_{rms} :

$$\frac{A_{true}}{A_{app}} = 1 + \frac{\sqrt{\pi}}{2} h'_{rms} \exp\left(\frac{1}{h'^2_{rms}}\right) \operatorname{erfc}\left(\frac{1}{h'_{rms}}\right), \quad (4.8)$$

with h'_{rms} calculated from the PSD as $(h'_{rms})^2 = \frac{1}{2\pi} \int_0^\infty q^3 C^{iso}(q) dq$. For generality, all integrals were performed over the entire range of size scales over which topography was measured; if the range of wavevectors is instead cut off at the contact size (c.a. 100 microns), the extracted results are identical (within 0.1%). Taken together, Eqs. 4.6 to 4.8 demonstrate the predicted dependence of W_{app} on material properties (E, μ) and topography C^{iso} .

The model for W_{app} (Eq. 4.6) is applied to the measured data as shown in Fig. 4.7A using $\gamma_1 = 25 \pm 5 \text{ mJ/m}^2$ [135, 147]. The minimum physically reasonable value of W_{app} is set to zero; predicted values below zero (for 10 MPa PDMS on NCD and MCD) imply that the surfaces will not perfectly conform. The best correlation between the experimentally measured work of adhesion and the predictions of Eq. 4.6 was obtained using the intrinsic work of adhesion of $37.0 \pm 3.7 \text{ mJ/m}^2$ ($R^2 = 0.67$). The explicit accounting for the change in area of the soft surface led to improved model predictions; if we do not account for this change (calculations shown in Chapter 3) the best fit to the measured data is significantly poorer ($R^2 = 0.28$) as shown in Fig. 4.6. The scatter in the experimental values as compared to the model could be a result of spot to spot variation because of larger asperities present on the diamond surface.

The retraction portion of contact differs sharply from approach (as shown in Fig. 4.3), and the JKR model does not provide an adequate fit to the unloading data. Despite the poor fit, the JKR model can be used to extract a value for work of adhesion upon retraction, either by applying it only to the pull-off point, or by applying it to the several (c.a. 6) points before pull-off. Doing so (Table 4.1) yields work of adhesion values in the range of 20 to 160 mJ/m^2 . However, there is

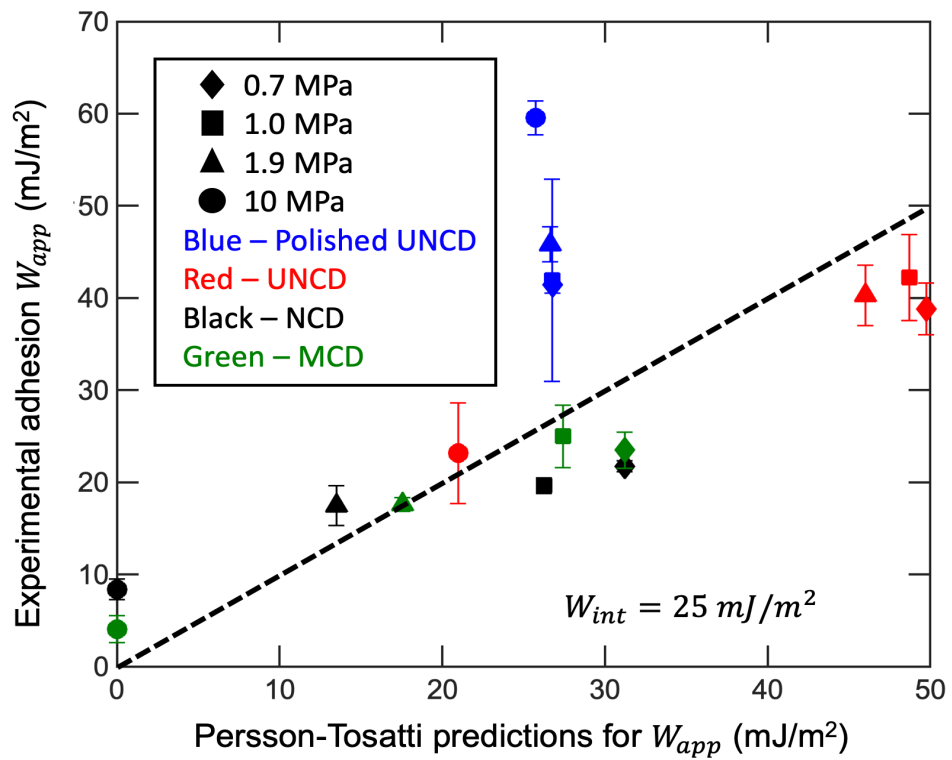


Figure 4.6: The experimental measurements of W_{app} can be compared against the unmodified Persson-Tosatti model, which does not account for the change in area of the soft elastomer.

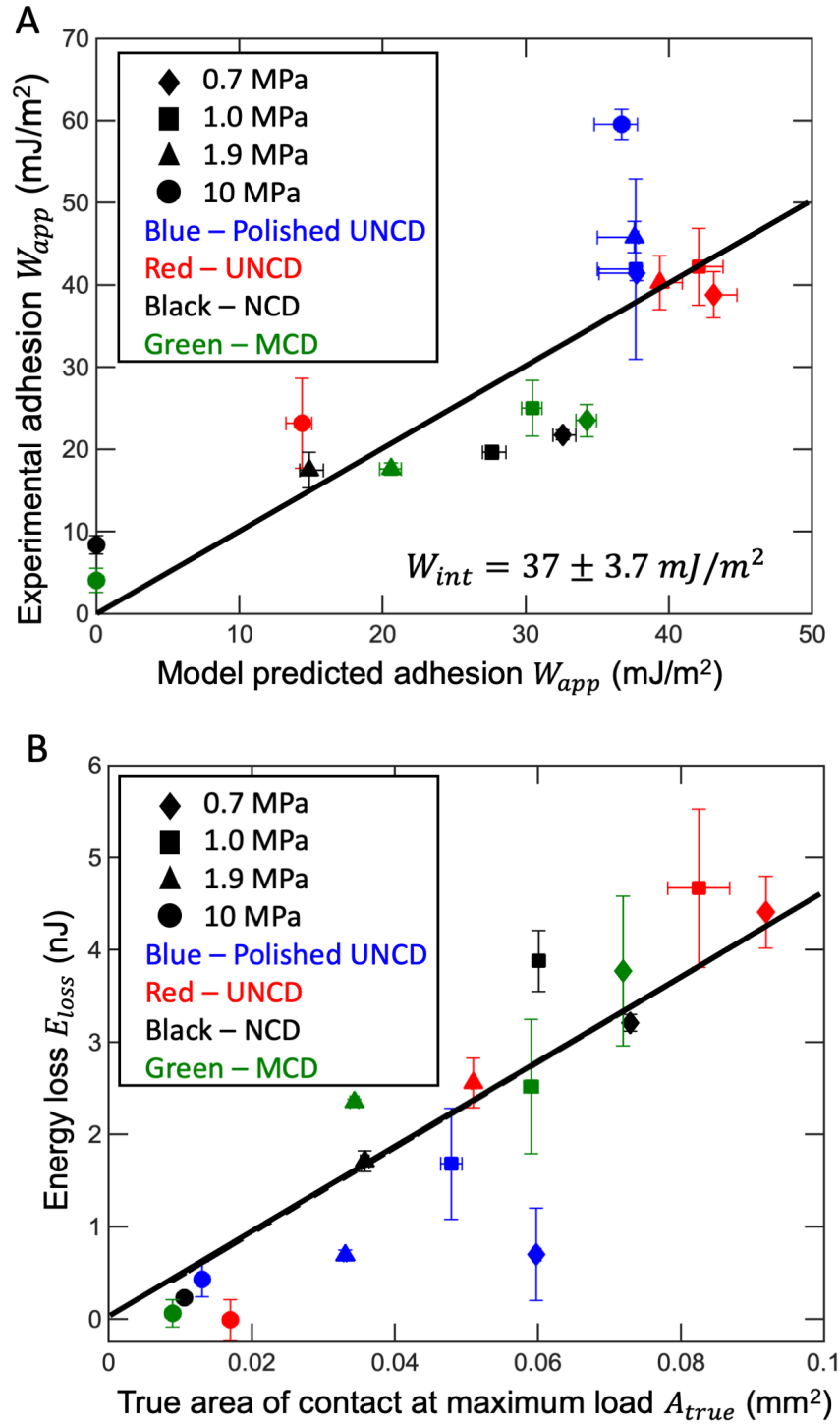


Figure 4.7: Comparison of work of adhesion and energy loss with the proposed model of conformal contact. Experimental measurements of apparent work of adhesion during approach (A) are well-fit using the balance of adhesive and elastic energy described in the Eqs. 4.6 to 4.8; here the solid line represents $y = x$. In panel B, the energy loss is plotted as a function of true contact area (Eq. 4.8). The solid line is a linear fit to the data and has a slope of $46.1 \pm 7.8 \text{ mJ/m}^2$ ($R^2 = 0.8$).

little consistency between these values and there is no connection to the intrinsic value of work of adhesion determined from the approach data.

Table 4.1: Comparison of different work of adhesion values for nanodiamond substrates

Work of Adhesion upon Approach (in mJ/m^2)				
Substrate	0.7MPa	1.0MPa	1.9MPa	10.0MPa
Polished UNCD	41.4 ± 0.9	41.9 ± 11	45.5 ± 1.9	59.6 ± 1.8
UNCD	38.8 ± 2.81	42.2 ± 4.7	40.28 ± 3.3	23.15 ± 5.5
NCD	21.7 ± 0.6	19.6 ± 0.9	17.5 ± 2.15	8.37 ± 1.12
MCD	23.5 ± 2.0	25.0 ± 3.4	17.6 ± 0.8	4.1 ± 1.46
Work of Adhesion from Pull-off using Eq. 2.26 (in mJ/m^2)				
Polished UNCD	74.7 ± 2.6	88.0 ± 2.3	83.0 ± 2.0	102.0 ± 1.0
UNCD	153.0 ± 2.5	147.6 ± 17.1	131.7 ± 1.0	94.4 ± 1.3
NCD	118.3 ± 5.1	142.0 ± 5.8	100.9 ± 10.7	17.2 ± 4.7
MCD	120.0 ± 8.2	145.0 ± 7.3	116.0 ± 3.4	21.4 ± 5.0
Work of Adhesion upon retraction using Eq. 2.25 (in mJ/m^2)				
Polished UNCD	72.7 ± 2.2	95.2 ± 6.8	80.7 ± 1.7	94.4 ± 1.4
UNCD	131.7 ± 1.7	143.9 ± 16.3	128.4 ± 0.0	88.2 ± 1.2
NCD	116.2 ± 5.8	144.0 ± 2.3	97.8 ± 11.5	13.8 ± 5.7
MCD	118.7 ± 8.7	142.5 ± 7.4	113.4 ± 3.7	19.0 ± 5.2

Instead, we analyze the total energy loss during contact and separation. This quantity is computed as the integral under the loading and unloading curve, as shown in the inset in Fig. 4.5. The in-situ measurements of contact size yield the apparent area of contact during testing; to determine the true area of contact, we must multiply by the roughness-induced increase in true surface area (Eq. 4.9). We now plot the energy loss E_{loss} versus the true area of contact A_{true} at maximum preload. Figure 4.7B shows a linear correlation:

$$E_{loss} = W_{int}A_{true}. \quad (4.9)$$

with a best-fit intrinsic work of adhesion of $46.2 \pm 7.7 \text{ mJ}/\text{m}^2$. This value is in good agreement with the intrinsic work of adhesion for PDMS-diamond extracted from approach, lending further confidence that the experiment is indeed measur-

ing the fundamental molecular interactions, rather than an apparent property that may be governed by experimental parameters. These results in Fig. 4 provide a simple physical mechanism to explain both the lower work of adhesion during approach and the adhesion hysteresis upon retraction. During approach, the apparent work of adhesion is reduced from W_{int} by the energy required to deform the soft material to achieve conformal contact. This reduction can be quantitatively calculated using comprehensive, multi-scale measurements of topography (Eqs. 4.6 to 4.8). Furthermore, the energy loss during contact and separation matches with the product of W_{int} and the true contact area A_{true} at the maximum preload. Surface heterogeneities are known to pin the contact edge such that the retraction process depins the surface in instantaneous jumps over small localized microscopic regions[148]. We show that Griffith’s argument can be applied: these jumps occur once the elastic energy available is equal to the interface energy, and all elastic energy is dissipated in the creation of new surface[90].

The results show significant adhesion hysteresis in the absence of viscoelastic dissipation, and therefore demonstrate a fundamental origin of irreversible energy loss in soft materials that arises due to the roughness-induced increase in surface area and Griffith-like separation of the contact. The above results demonstrate how elastic materials behave on rigid rough surfaces. We think the above study provides helpful insights into designing reversible adhesives without the use of external stimulus such as electrical conductance or heat.

CHAPTER V

SHEAR BEHAVIOR OF ELASTOMER SLIDING ON ROUGH SURFACES

5.1 Introduction

With the ubiquitous use of soft elastic matter in daily human life, the nature of soft-hard interface becomes crucial in various mechanical elements such as wiper blades, tires, gaskets, footwear and adhesive tapes [11, 149, 150]. It is also crucial to understand the wall-slippage of rubber and dense polymers during processing and nowadays during additive manufacturing which can lead to severe material losses [151]. Additionally, there exist knowledge gaps in applying current principles of friction to soft robotics and sensing technologies where feedback due to shear forces and adhesion is effective only when substantial real interfacial contact exists [36]. Most surfaces we come across have hierarchical fractal roughness resulting in complicated interfacial friction responses, thus making it imperative to perform systematic experiments followed by comparison with theoretical models for friction on rough surfaces[152].

Pioneering work of Grosch on rubber friction have shown that during sliding the friction forces increase with velocity to reach a maximum and then decrease [56]. Grosch's major contribution lies in being able to draw a master curve for friction time-temperature superposition as theorized by William, Landell and Ferry (WLF) [97], that has been discussed extensively in the background chapter of this thesis. As a result of adhesion and stretching, the surface chains can

attach and detach from surfaces. The kinetics depends largely on molecular weight and consequently on the deformation behavior of rubber network. The bonding-debonding follows a reaction rate and thus Arrhenius theory of certain activation energy having a rate constant similar to shift factor in the WLF theory. Chernyak and Leonov theorized this stochastic bond formation and breaking as a probability distribution function that depends upon the network chain density and the chain length (ability to stretch the network) [58].

$$\tau = \Sigma_0 \frac{\int_0^\infty \phi\left(\frac{r(t)}{\delta}\right) p(V, t) dt}{V[\langle t \rangle_b + \langle t \rangle_f]} \quad (5.1)$$

For eq. 5.1, Σ_0 is the areal density of chain network ends, $\phi\left(\frac{r(t)}{\delta}\right)$ is the stored deformation energy in the network and $p(V, t)$ is the transition probability of the different attachment points between the network-chain ends and the surface. While, it is inversely proportional to the mean distance travelled by the chain as a product of velocity of sliding V , residence time or the time chain ends are bonded at the adhesive interface $\langle t \rangle_b$ and the free time when they are not bonded $\langle t \rangle_f$. The model suggests that the observed shear stress is proportional to the work done in stretching the polymer network so as to detach from the interface. Thus, a quantitative molecular model for frictional adhesive sliding is established.

While adhesive steady sliding is extensively studied, the observation of other transition states at higher velocities remain less explored. The transition from steady state sliding to stick-slip at higher velocities, which can be periodic or chaotic, is often attributed to competition between adhesion hysteresis and stress relaxation. However, very little theoretical background, that explains the origin of stick-slip dynamics, exists till date [153–155].

At very high velocities there is an occurrence of air pockets in the contact region as a result of very low relaxation time and adhesion for the rubber at the interface[124]. These air pockets generated at particular frequency move from the front of the contact region to the rear end creating wave-like patterns first observed by Schallamach [57]. Thus, depending on energy dissipation mechanism at different velocities there could be different states of the frictional interface [156]. It has been shown before that during friction there could be discrete contact regions for asperities even when complete contact was established in normal adhesion, especially in case one of them is rough. Thus, there could be two separate components for friction, especially for cross-linked elastomers, as a result of interfacial adhesion and deformation [157–159]. The equation can be written as:

$$F_{shear} = F_{adhesion} + F_{deformation}. \quad (5.2)$$

The above relation assumes that there is little or no contribution to friction force from wear and tear that occurs at the sliding rubber interface (which does not represent reality and might significantly contribute to shear forces). Shear adhesion would depend upon the real area of contact and the interfacial strength which could be similar to eq. 5.1 where,

$$F_{shear} = A_{real} \times \tau + F_{deformation}. \quad (5.3)$$

Elastomer friction on rough surfaces is one of the most relevant and less explored subjects. After the understanding that friction is a response to shear motion in combination with adhesive forces and normal load, there have been theoretical studies that point to the effect of roughness on friction [26, 42]. Grosch in his

independent study of rubber sliding on a surface with magnesia particles spread showed that maximum shear stresses were reached at much lower velocities as compared to smooth surfaces. However, these experiments had free particles that were stuck to the rubber surface instead of a stationary rough substrate. Persson has performed a series of systematic studies that predict coefficient of friction on rough surfaces having a known surface roughness power spectrum or power spectral density (PSD) [27]. A PSD function is a mathematical tool to represent surface roughness that is defined as the Fourier transform of the height autocorrelation function of the waves having different wavelengths and amplitudes. Thus, we have seen from earlier chapters that with the help of PSD, surfaces can have well-defined roughness. Taking advantage of this known roughness system there could be accurate measurement of friction response with controlled surface chemistry and bulk properties.

Rewriting eq. 5.3 in terms of shear stresses we get,

$$\frac{F_{shear}}{A_{app}} = AreaRatio \times \tau + \frac{P}{A_{app}}. \quad (5.4)$$

Here, $\frac{P}{A_{app}}$ is the stress corresponding to deformation as a result of applied load which is non-adhesive. Now the deformation shear stress for non-adhesive contact can be substituted from eq. 21 derived by Persson in ref. [27] and section 2.5.1.1,

$$\sigma = AreaRatio \times \tau + \frac{1}{2} \int dq q^3 C(q) Im \frac{E(qv)}{1 - \nu^2}. \quad (5.5)$$

5.2 Experimental

To test the above model, we have measured friction between elastomeric lenses of different moduli with rough diamond surfaces with the corresponding

observation of the dynamic changes in interfacial area of contact. We observe a rate and state transition for shear stresses and contact area over velocities ranging from nm/sec to m/sec with elastomer modulus ranging from 0.7 MPa to 1.9 MPa. The roughness of the diamond surfaces is varied by changing the power spectral density functions as described in Chapter 4. We have also compared our data to Persson's predicted equation with the knowledge of surface roughness of nanodiamond and viscoelasticity of rubber material. The method for measuring friction is described in Chapter 3 with complete details. Before testing the elastomer lenses on rough surfaces, friction was performed on a smooth Octadecyltrichlorosilane (OTS) monolayer deposited on a silicon wafer surface. This would not only serve as a control for comparison with rough surfaces but also verify the molecular processes that happen during sliding of an elastomer (eq. 1) experimentally shown by Vorvolakos et al. previously [23].

5.3 Results

As shown in Fig. 5.1, the shear stress increases with velocity reaches a maximum and then either plateaus out or decreases. Stress is higher for higher modulus or lower cross-linked molecular weight. The observed maxima for the stress after fitting a Gaussian curve comes out to be close to a particular velocity independent of the modulus. There is observation of state processes during sliding where at low velocities there is steady-state sliding ($\mu\text{m}/\text{sec}$), at intermediate velocity we see stick-slip ($100 \mu\text{m}/\text{sec}$) and at high velocities (mm/sec) we see Schallamach waves, as evident from Fig. 5.2. Thus, both rate and state process are verified on smooth surfaces. In their work, Vorvolakos et al. were able to

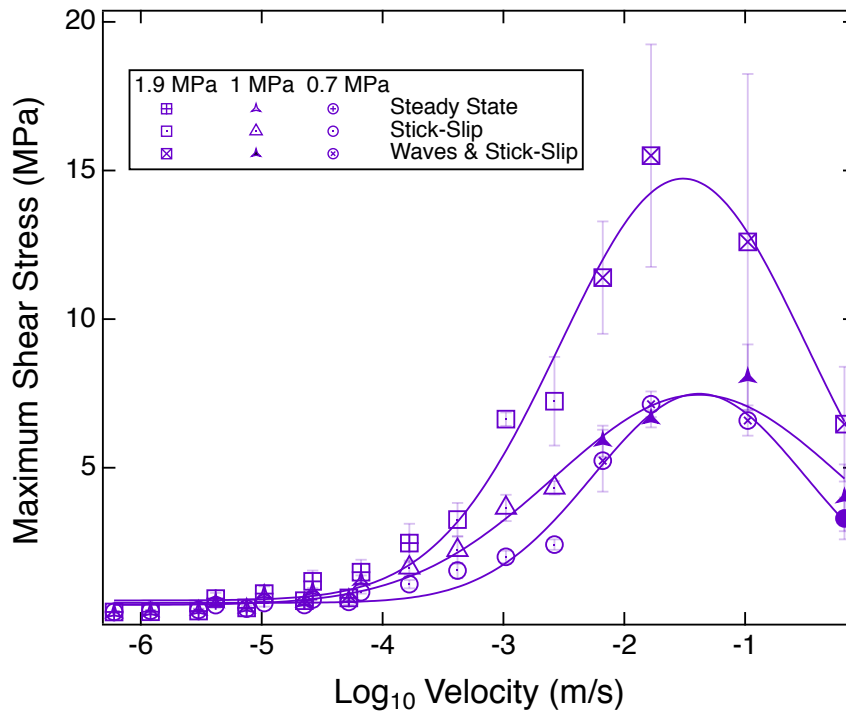


Figure 5.1: Real shear stress observed by averaging the maxima obtained from the stress curves as a function of modulus and sliding velocity. The solid lines are the Gaussian fitting functions to the shear stress curves as a function of velocity, similar to eq. 1 showing maxima at a particular velocity independent of elastic modulus. However, as the modulus increases the shear stress increases proportionally.

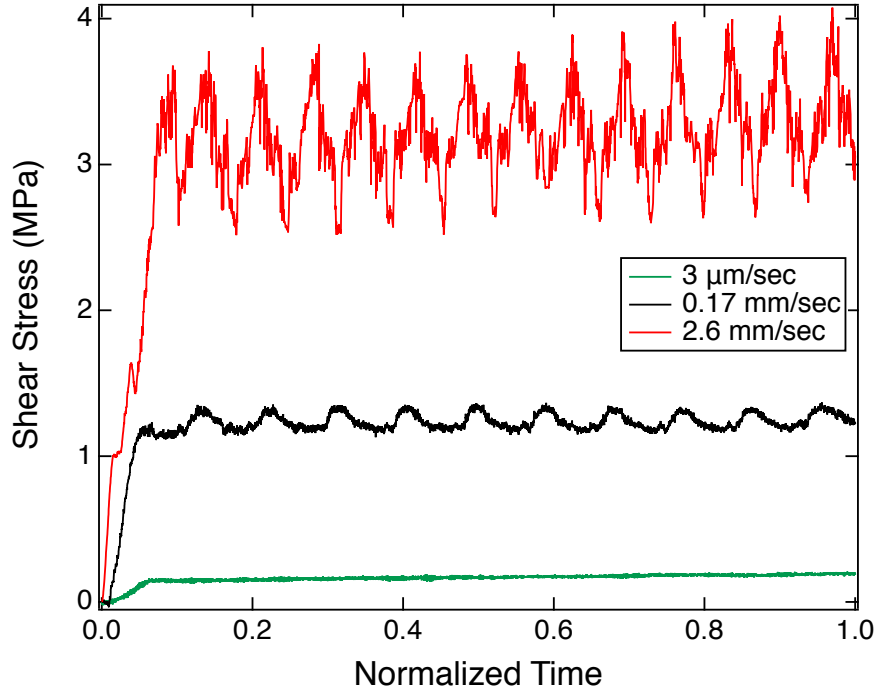


Figure 5.2: The plot of shear stress curves as a function of time for 0.7 MPa PDMS on OTS surface at three different velocities showing three different states of steady state sliding (2.6 mm/sec), periodic stick-slip (0.17 mm/sec) and Schallamach wave behavior (3 $\mu\text{m}/\text{sec}$).

observe stick-slip on low energy smooth surfaces, but it is for the first time that detachment waves are observed for such surfaces at very high velocities. This reiterates the predictions of Ludema et. al and Savkoor et. al where in as the sliding happens at higher velocities the energy stored as deformation is reduced and there is loss in contact area.

On rough surfaces, the observed trends with respect to states are similar but the onset is earlier as compared to smooth surfaces (see Fig. 5.3). The most striking observation for friction on rough surfaces is that the maximum shear stresses are large at low velocities and smaller at higher velocities as compared to smooth surfaces, where the difference between stresses on Polished UNCD and UNCD become dominant at higher velocities. Thus, the observation of Gaussian function with one single peak in case of a smooth surface is not applicable on

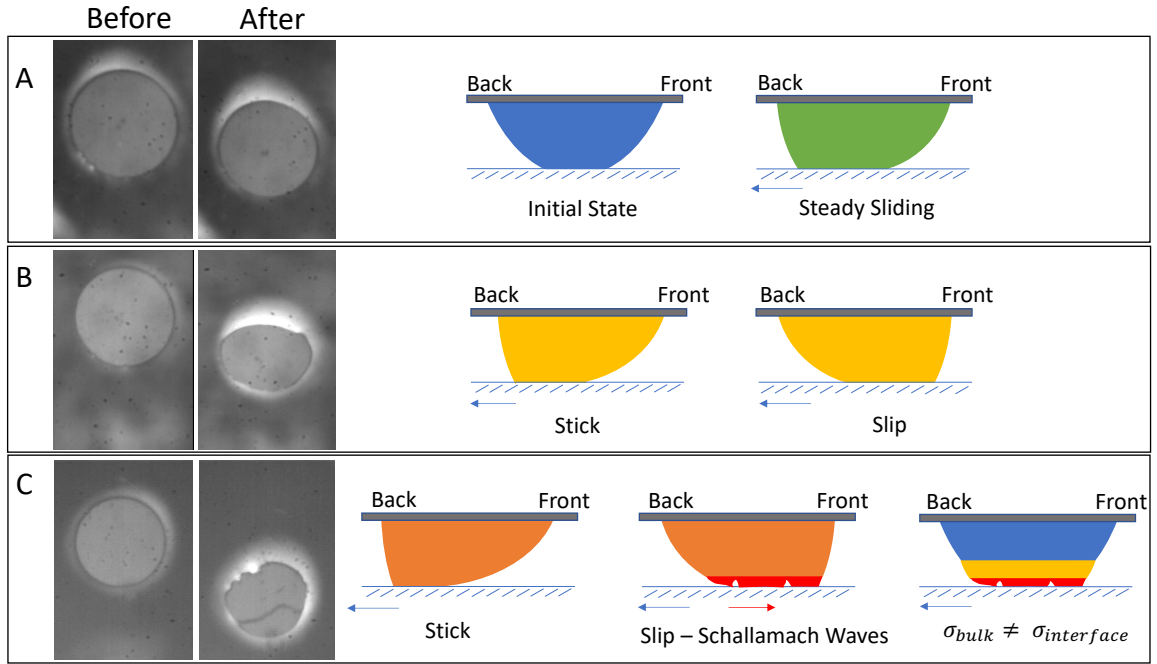


Figure 5.3: Depicts the three states through the contact area images captured before and after sliding on a rough UNCD surface wherein the detachment wave is visible in C. The different contact area changes during sliding along with the stress variations (through colors) are depicted qualitatively in the side view schematics drawn on the right-hand-side. The stresses increase according to the order of colors- blue, green, yellow, orange, red.

rough surfaces because of the added contact area and the elastic deformation.

Fig. 5.4A shows the comparison of 0.7 MPa PDMS lens sliding on smooth OTS surface and rough diamond surfaces. Similar trend is observed for 1 MPa and 1.9 MPa PDMS shown in Fig. 5.4B and C. The different states are clearly notified for corresponding velocities illustrating the stresses and velocities at which state transitions occur.

A major finding from the onset stresses for different moduli is that the critical shear stress necessary for the occurrence of different states scales with the modulus of the sliding elastomer (Fig. 5.5). This shows that deformation energy due to applied shear stresses changes resulting into frictional states. There was no such correlation obtained for critical stress as a function of velocity.

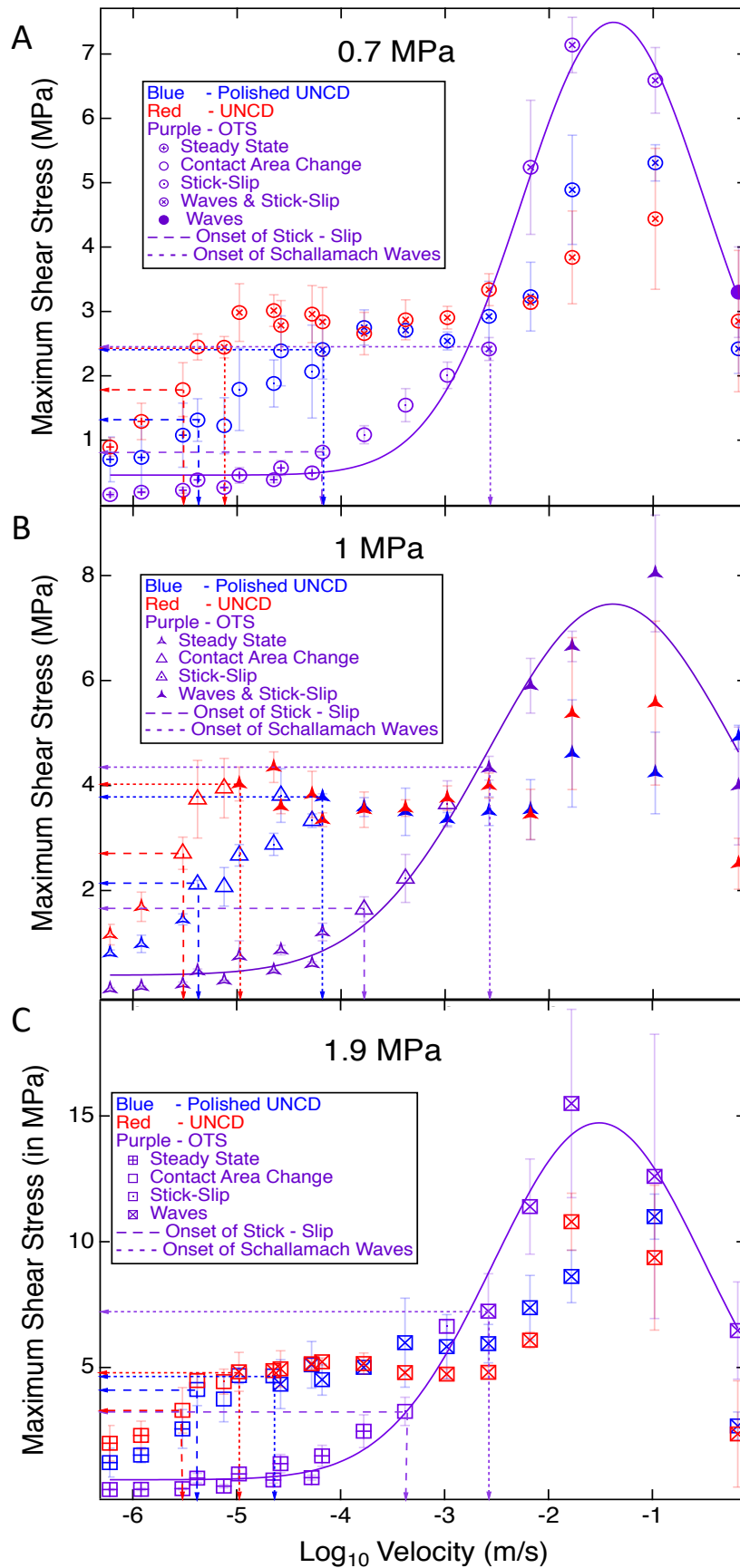


Figure 5.4: Comparative plot for the maximum shear stresses as a function of velocity between PDMS hemisphere and the rigid surfaces of smooth OTS monolayer and rough diamond surfaces i.e. UNCD and Polished UNCD for 0.7 MPa (A), 1 MPa (B) and 1.9 MPa (C). The different symbol types show distinction in moduli and frictional states.

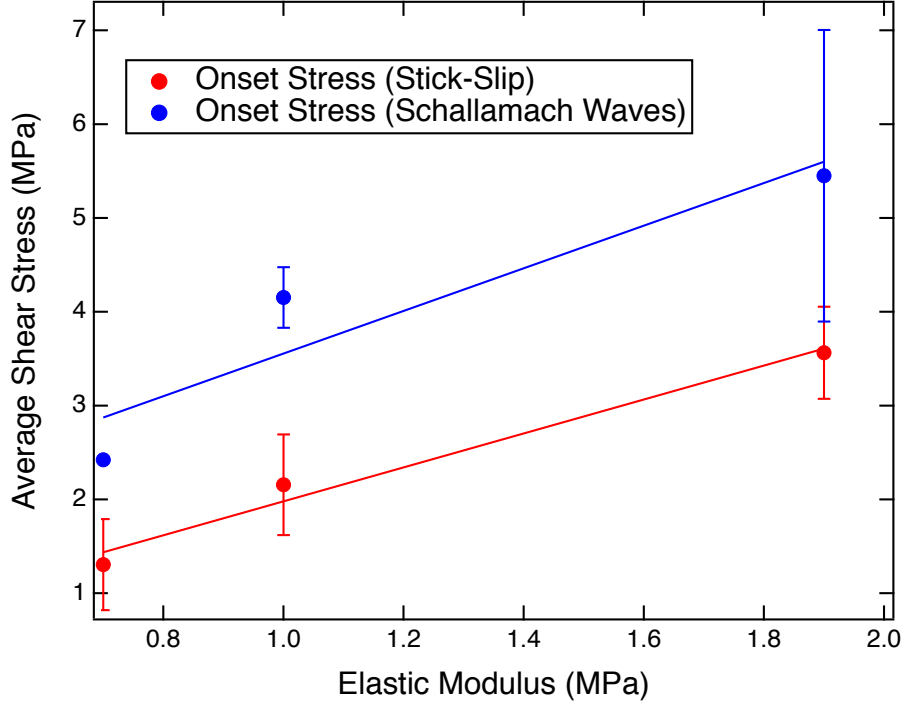


Figure 5.5: The increasing trend of critical stresses for the instabilities (stick-slip in red and detachment waves in blue) as a function of modulus for all the surfaces showing there is a critical stress irrespective of roughness. The solid lines are a guide to the eye.

To predict shear stress using eq. 5.5, the non-adhesive deformation component depends upon frequencies of vibration for the rubber network at the rough interface. These can be obtained by multiplying the roughness frequency ' q ' in space to the velocity ' v ' of sliding. These frequencies ' qv ' in a range correspond to the loss modulus of the rubber material from a standard Dynamic Mechanical Analysis (DMA) curve. To make such predictions we need to measure the bulk viscoelasticity of the elastomer at different frequencies and since the range of frequencies of vibration is large we needed to measure modulus at different temperatures and superpose them according to the time-temperature superposition (TTS) principle using the Williams-Landell-Ferry (WLF) model [97]. Temperature sweep plots in Fig. 5.6 and the TTS plots in Fig. 5.7 show the measured dynamic mechanical behavior of 1 mm thick elastic sheets made with similar cross-

linking chemistry as the lenses used in friction experiments. It is evident from the plot that the complex elastic modulus is not affected significantly by the loss modulus at lower frequencies which correspond to the ambient temperature conditions where the storage or complex moduli for the elastic materials are constant. We have labelled the three elastic materials according to the complex or storage moduli at room temperature that is 0.7, 1 and 1.9 MPa.

Fig. 5.8 A and B are the comparison for Polished UNCD and UNCD surface using predictions of eq. 5.5. The predictions do not match the observed shear stress on rough surfaces. This show that our understanding of shear behavior as a function of velocity is still missing a crucial component. We can discuss qualitatively what are the missing parameters in the theory. It is quite possible that the deformation term might play a significant role at even lower velocities especially on rough surfaces which is not captured by the deformation term in its current form. The plots show that the equation predicts higher shear stress at higher velocities for rough surfaces assuming the adhesive term (first term) encompasses the whole conformal contact, which is not the case as we know that Schallamach waves are air pockets that create detachment fronts. Moreover, at higher velocities there is significant amount of reduction in real contact area not captured by a microscopic video under visible light. Thus, a friction model will be complete only if it incorporates all the different state behaviors and the physics of their occurrence or nucleation.

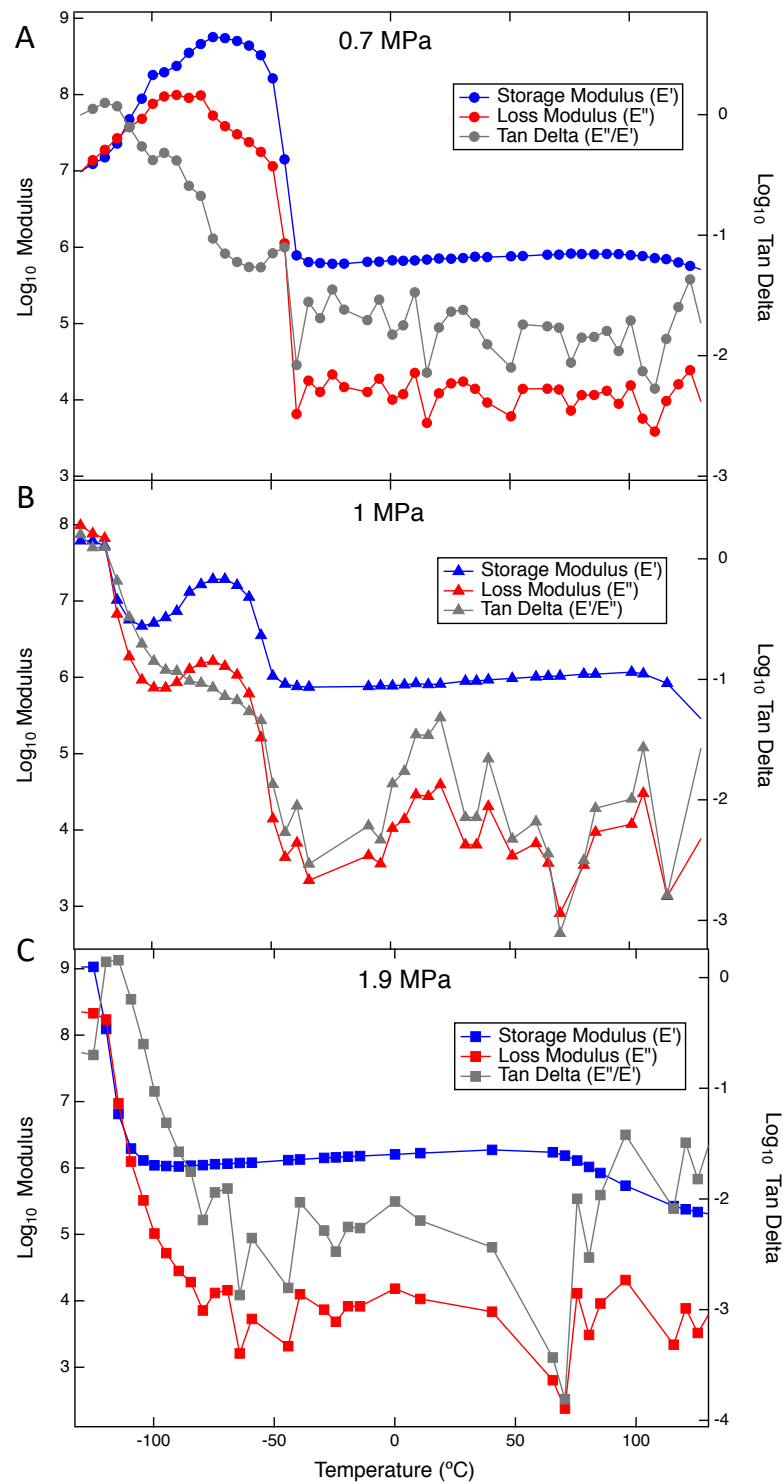


Figure 5.6: DMA temperature sweep plots for the 0.7 (A), 1 (B) and 1.9 MPa (C) PDMS sheets showing complex elastic, storage and loss moduli. The range of temperatures (-130 to 130 C) translates to the range of frequencies required for friction model.

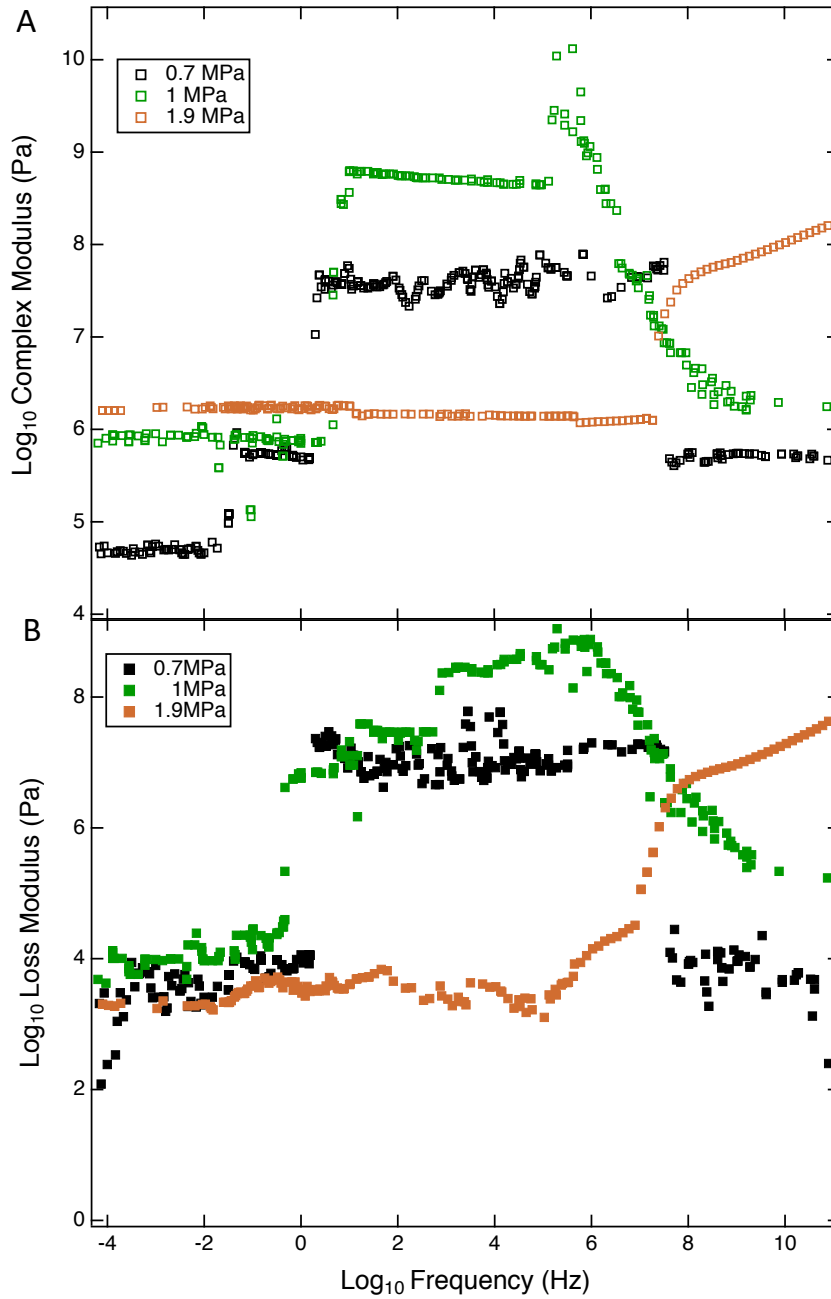


Figure 5.7: TTS plots for the 0.7, 1 and 1.9 MPa sheets showing complex elastic modulus and loss modulus for 15 orders of frequencies. The spline function for the loss moduli were used to predict the second term in eq. 5.5.

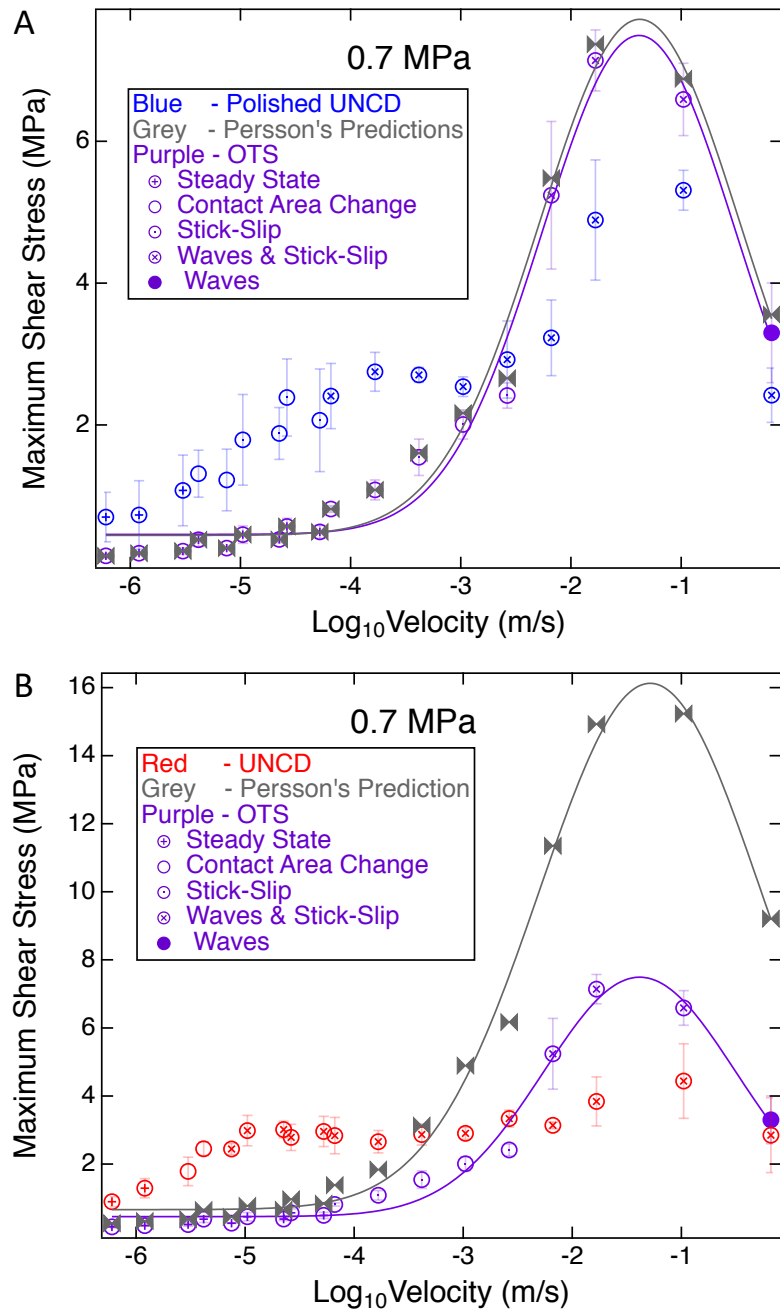


Figure 5.8: Predictions for frictional stress on rough surfaces as a function of velocity as compared to the experimental observations.

5.4 Discussion

Let us discuss the states of friction observed in the above cases. The simplest is the steady state behavior where in the sliding is purely based on Amontons' laws of friction. In stick-slip behavior, the contact area decreases as the force increases to reach a critical stress, followed by a decrease in stress and an increase in contact area; this behavior repeats over time. As the sliding velocity increases the elastic material at the interface begins to buckle followed by the buckle propagating through the interface; simultaneously the system is also exhibiting the stick-slip behavior that is seen at lower velocities. As the sliding velocity is increased even more, the critical bulk stress to initiate a Schallamach wave decreases to zero. The maximum stress occurs before the critical bulk stress to propagate a Schallamach wave is zero. Once the critical bulk stress to propagate a Schallamach wave reaches zero the observed stress to slide the elastic body decreases.

These observations suggest the following: at low velocities the bulk and interface experience the same stress (i.e. energy is uniformly distributed within the body), and at some critical stress the interface must buckle as the interfacial strength is not capable of sustaining the stress, this allows the system to spend elastic energy to increase the sliding velocity, or decrease the energy required to slide (i.e. a Schallamach wave is a way for the system to convert elastic energy into kinetic energy); as the sliding velocity increases the stress and energy within the system becomes more localized to the interface, such that the interface and bulk are under different amounts of stress (this suggests that there is an energy diffusion rate from the interface to the bulk); at some critical velocity the energy is completely localized to the interface and Schallamach waves propagate at zero

bulk stress and the force required to slide begins to decrease. The open question then is how does the material and interface properties control this behavior?

We can see that the critical stress to propagate a Schallamach wave is independent of the surface roughness, however the critical sliding velocity is a function of roughness. From this we know that it takes more energy to slide and conform to a rough surface than to slide and conform to a smooth surface. The interesting observation though is that once Schallamach waves begin to propagate the stress to slide plateaus until some much faster velocity. This is analogous to the "spurt" phase during extrusion, where many extrusion velocities are possible with a single applied stress. We observe that as the sliding speed increases during the plateau phase the rate of generation and velocity of the Schallamach waves increases. This suggests that as the applied power increases up to some critical amount Schallamach waves are completely capable of spending that additional energy otherwise one would observe an increase in the required force to slide. However, after some critical sliding velocity Schallamach waves are unable to accommodate the increased sliding velocity such that we observe a larger energy to slide. To accommodate the additional energy input per second during this phase the energy begins to become localized, where a critical amount of localization is achieved after the maximum stress corresponding to Schallamach waves being generated at zero bulk stress. This energy localization causes a decrease in the observed sliding force and coefficient of friction.

We observe for the smooth surface there is a gaussian like curve that represents the maximum stress as a function of sliding velocity. The increase in stress is due to increased energy dissipation within the bulk of the material.

Since the bulk material must deform to slide, and the rate of deformation must increase as sliding speed increases, less energy elastic energy is converted into kinetic energy. Once a critical stress is achieved Schallamach waves are generated and an inflection point occurs in the stress vs velocity curve signifying the system is becoming more efficient at converting elastic energy into kinetic energy. As the sliding velocity increases the energy (as in the rough surfaces) begins to localize to the interface; as in the rough surfaces the bulk stress to propagate a Schallamach wave approaches zero after the maximum. The detachment waves are physically similar to a dimple that could be caused in an elastomer brought in contact at very high velocity in the presence of liquid. Depending on the thickness of the elastomer the formation of dimple could vary, observed by Frechette et. al [160]. This might be one of the reasons why Vorvolakos et. al did not observe detachment waves since they were using PDMS thin films transferred onto a lens of higher modulus avoiding elastic deformation.

5.5 Summary

In the presence of adhesion and deformation of rubber during friction we obtain three transitory states for the contact area namely static, stick-slip and elastic instability (Schallamach waves). These states are the shear stress relaxation mechanisms that only occur in rubber materials as a result of bulk deformation. However, this dependence is not solely because of the adhesion of the rubber with the surface but also the hysteresis or deformation of the material. On surfaces which have roughness at many length scales, the occurrence of Schallamach waves is at far lower velocities than on smooth surfaces showing early nucleation of

waves due to the added roughness and very short relaxation time available for the deformed material to maintain contact during sliding.

CHAPTER VI

CONCLUSIONS

The above dissertation work is a step towards intriguing questions in the field of contact mechanics which might be incomplete but have been able to provide certain clues for solving the puzzle that has existed for decades. It was mere coincidence that at this point of time the scientific and technological capabilities enabled us to design experiments and verify adhesion and friction models.

For adhesion, the JKR model was a useful methodology to calculate work of adhesion between surfaces for a given range of elastic modulus. However, it failed to incorporate the effect of surface roughness. We have made an attempt to predict the apparent work of adhesion on rough surfaces using the apparent contact area obtained for an applied load using JKR formalism and then relate it to real work of adhesion for known surface roughness. With the help of controlled surface chemistry and roughness we have seen that adhesion of soft materials depends upon the change in surface energy as a result of applied strain. Most importantly, intimate contact is achieved as a result of this modified work of adhesion. Persson's theory helps in predicting the apparent work of adhesion on rough surfaces. All the energy lost as adhesion hysteresis during pull-off is proportional to the total intimate contact area formed, that satisfies the Griffith's criterion from fracture mechanics. The model that we propose is still incomplete since it has not unified the energy balance proposed by JKR theory for both

loading and unloading incorporating roughness. This will be complete only when similar JKR experiments are performed with change in normal loads and velocities in air as well as liquid environments, that pose numerous experimental challenges. Changes in work of adhesion and Griffith's energy loss as a result of application of normal loads and higher velocities need to be verified with the awareness of boundary conditions of linear elasticity and non-equilibrium effects.

In the shear experiments, we wanted to relate adhesion hysteresis to friction observed on rough surfaces and incorporate molecular theory of rubber friction and Persson's theory of non-adhesive friction that calculates deformation energy due to roughness, into one single theory. However, we had surprising observations for amount of stress observed on rough and smooth surfaces. The onset of states happen at a critical stress values for a particular elastic modulus independent of roughness. In addition, we concluded that the stresses on rough surfaces are higher at lower velocities and lower at higher velocities as compared to smooth surfaces. A qualitative reason for this observation is the deformation energy or hysteresis which at lower velocities is higher for rough surfaces and decreases with increasing velocity. The interplay of contact area and deformation causes adhesion to vary with velocities and thus friction. However, it is not easy to quantify this velocity and roughness dependent shear stresses and further mathematical rigor is necessary. A true breakthrough in understanding rubber adhesion and friction is possible if we are able to probe the true contact area formed on rough surfaces. There are different spectroscopic and fluorescence techniques that enable this active area of research but not without individual limitations. Viscoelasticity, wear and material losses are some of the unknown bulk changes that are constantly

happening during contact and deformation. There are hardly any characterization tools that focus solely on understanding such phenomena.

The above experiments have shown that there are many open questions in the field of contact mechanics. Investigations so far are not sufficient to understand the relation between adhesion and friction and how roughness can affect these properties which are relevant to many modern technologies. At the same time, thermodynamic laws should have been universally applicable to adhesion hysteresis, contact angle hysteresis and friction. There exists clearly differences and linkages in all these interfacial phenomena at various levels through the observations above.

REFERENCES

- [1] Gadelmawla, E.; Koura, M.; Maksoud, T.; Elewa, I.; Soliman, H. *Journal of materials processing Technology* **2002**, *123*, 133–145.
- [2] Jacobs, T. D.; Junge, T.; Pastewka, L. *Surface Topography: Metrology and Properties* **2017**, *5*, 013001.
- [3] Majumdar, A.; Bhushan, B. *Journal of tribology* **1990**, *112*, 205–216.
- [4] Israelachvili, J. N. *Intermolecular and surface forces*; Academic press, 2015.
- [5] De Gennes, P.-G.; Brochard-Wyart, F.; Quéré, D. *Capillarity and wetting phenomena: drops, bubbles, pearls, waves*; Springer Science & Business Media, 2013.
- [6] Liang, H.; Cao, Z.; Wang, Z.; Dobrynin, A. V. *ACS Macro Letters* **2018**, *7*, 116–121.
- [7] Chaudhury, M. K.; Owen, M. J. *Langmuir* **1993**, *9*, 29–31.
- [8] Man, K. *Contact mechanics using boundary elements*; 1994.
- [9] Kinloch, A. *Journal of Materials Science* **1982**, *17*, 617–651.
- [10] Creton, C.; Ciccotti, M. *Reports on Progress in Physics* **2016**, *79*, 046601.
- [11] Persson, B. N.; Albohr, O.; Tartaglino, U.; Volokitin, A.; Tosatti, E. *Journal of physics: Condensed matter* **2004**, *17*, R1.
- [12] Persson, B. N. *Surface science reports* **2006**, *61*, 201–227.
- [13] Persson, B.; Tosatti, E. *The Journal of Chemical Physics* **2001**, *115*, 5597–5610.
- [14] Fuller, K.; Tabor, D. *Proceedings of the Royal Society of London. A. Mathematical and Physical Sciences* **1975**, *345*, 327–342.
- [15] Briggs, G.; Briscoe, B. *Journal of Physics D: Applied Physics* **1977**, *10*, 2453.
- [16] Deng, W.; Kesari, H. *Scientific reports* **2019**, *9*, 1639.
- [17] Woydt, M.; Wäsche, R. *Wear* **2010**, *268*, 1542–1546.

- [18] Andablo-Reyes, E.; Hidalgo-Álvarez, R.; de Vicente, J. *Soft Matter* **2011**, *7*, 880–883.
- [19] Schallamach, A. *Proceedings of the Physical Society. Section B* **1952**, *65*, 657.
- [20] Grosch, K. *Rubber Chemistry and technology* **1996**, *69*, 495–568.
- [21] Le Gal, A.; Klüppel, M. *Journal of Physics: Condensed Matter* **2007**, *20*, 015007.
- [22] Vaenkatesan, V.; Li, Z.; Vellinga, W.-P.; de Jeu, W. H. *Polymer* **2006**, *47*, 8317–8325.
- [23] Vorvolakos, K.; Chaudhury, M. K. *Langmuir* **2003**, *19*, 6778–6787.
- [24] Perutz, S.; Kramer, E.; Baney, J.; Hui, C.-Y.; Cohen, C. *Journal of Polymer Science Part B: Polymer Physics* **1998**, *36*, 2129–2139.
- [25] Bowden, F. P.; Tabor, D. *Proceedings of the Royal Society of London. Series A. Mathematical and Physical Sciences* **1939**, *169*, 391–413.
- [26] Archard, J. *Proceedings of the Royal Society of London. Series A. Mathematical and Physical Sciences* **1957**, *243*, 190–205.
- [27] Persson, B. *The Journal of Chemical Physics* **2001**, *115*, 3840–3861.
- [28] Niewiarowski, P. H.; Stark, A. Y.; Dhinojwala, A. *Journal of Experimental Biology* **2016**, *219*, 912–919.
- [29] Spolenak, R.; Gorb, S.; Arzt, E. *Acta biomaterialia* **2005**, *1*, 5–13.
- [30] Gao, H.; Wang, X.; Yao, H.; Gorb, S.; Arzt, E. *Mechanics of Materials* **2005**, *37*, 275–285.
- [31] Autumn, K.; Majidi, C.; Groff, R.; Dittmore, A.; Fearing, R. *Journal of Experimental Biology* **2006**, *209*, 3558–3568.
- [32] Cho, H.; Wu, G.; Jolly, J. C.; Fortoul, N.; He, Z.; Gao, Y.; Jagota, A.; Yang, S. *Proceedings of the National Academy of Sciences* **2019**, 201818534.
- [33] Holten-Andersen, N.; Harrington, M. J.; Birkedal, H.; Lee, B. P.; Messersmith, P. B.; Lee, K. Y. C.; Waite, J. H. *Proceedings of the National Academy of Sciences* **2011**, *108*, 2651–2655.
- [34] Linghu, C.; Wang, C.; Cen, N.; Wu, J.; Lai, Z.; Song, J. *Soft matter* **2019**, *15*, 30–37.
- [35] Linghu, C.; Zhu, H.; Zhu, J.; Li, C.; Song, J. *Extreme Mechanics Letters* **2019**, *27*, 76–82.

- [36] Ayyildiz, M.; Scaraggi, M.; Sirin, O.; Basdogan, C.; Persson, B. N. *Proceedings of the National Academy of Sciences* **2018**, *115*, 12668–12673.
- [37] Hertz, H. R. *Verhandlung des Vereins zur Beforderung des Gewerbefleißes, Berlin* **1882**, 449.
- [38] Johnson, K. L.; Kendall, K.; Roberts, A. *Proceedings of the royal society of London. A. mathematical and physical sciences* **1971**, *324*, 301–313.
- [39] Maeda, N.; Chen, N.; Tirrell, M.; Israelachvili, J. N. *Science* **2002**, *297*, 379–382.
- [40] Luengo, G.; Pan, J.; Heuberger, M.; Israelachvili, J. N. *Langmuir* **1998**, *14*, 3873–3881.
- [41] Tiwari, A.; Dorogin, L.; Bennett, A.; Schulze, K.; Sawyer, W.; Tahir, M.; Heinrich, G.; Persson, B. *Soft Matter* **2017**, *13*, 3602–3621.
- [42] Greenwood, J.; Williamson, J. P. *Proceedings of the royal society of London. Series A. Mathematical and physical sciences* **1966**, *295*, 300–319.
- [43] Nayak, P. R. *Journal of lubrication Technology* **1971**, *93*, 398–407.
- [44] Yang, C.; Persson, B. *Physical review letters* **2008**, *100*, 024303.
- [45] Persson, B.; Scaraggi, M. *The Journal of chemical physics* **2014**, *141*, 124701.
- [46] Silberzan, P.; Perutz, S.; Kramer, E. J.; Chaudhury, M. K. *Langmuir* **1994**, *10*, 2466–2470.
- [47] Choi, G. Y.; Kim, S.; Ulman, A. *Langmuir* **1997**, *13*, 6333–6338.
- [48] Chen, Y.; Helm, C.; Israelachvili, J. *The journal of physical chemistry* **1991**, *95*, 10736–10747.
- [49] Pickering, J.; Van Der Meer, D.; Vancso, G. J. *Journal of adhesion science and technology* **2001**, *15*, 1429–1441.
- [50] Peressadko, A.; Hosoda, N.; Persson, B. *Physical review letters* **2005**, *95*, 124301.
- [51] Kesari, H.; Doll, J. C.; Pruitt, B. L.; Cai, W.; Lew, A. J. *Philosophical Magazine & Philosophical Magazine Letters* **2010**, *90*, 891–902.
- [52] Yurdumakan, B.; Harp, G. P.; Tsige, M.; Dhinojwala, A. *Langmuir* **2005**, *21*, 10316–10319.
- [53] She, H.; Malotky, D.; Chaudhury, M. K. *Langmuir* **1998**, *14*, 3090–3100.
- [54] Luan, B.; Robbins, M. O. *Nature* **2005**, *435*, 929–932.

- [55] Mo, Y.; Turner, K. T.; Szlufarska, I. *Nature* **2009**, *457*, 1116–1119.
- [56] Grosch, K. *Proceedings of the Royal Society of London. Series A. Mathematical and Physical Sciences* **1963**, *274*, 21–39.
- [57] Schallamach, A. *Wear* **1971**, *17*, 301–312.
- [58] Chernyak, Y. B.; Leonov, A. *Wear* **1986**, *108*, 105–138.
- [59] Blake, T. D. *Journal of colloid and interface science* **2006**, *299*, 1–13.
- [60] Gent, A. *Langmuir* **1996**, *12*, 4492–4496.
- [61] Wang, Y.-Q.; Zhang, F.-Q.; Sherwood, P. M. *Chemistry of materials* **1999**, *11*, 2573–2583.
- [62] Somorjai, G. A.; Li, Y. *Introduction to surface chemistry and catalysis*; John Wiley & Sons, 2010.
- [63] Turcotte, D. L. *Pure and applied Geophysics* **1989**, *131*, 171–196.
- [64] Dowson, D. *Journal of Lubrication Technology* **1977**, *99*, 382–386.
- [65] Mandelbrot, B. *Science* **1967**, *156*, 636–638.
- [66] Mandelbrot, B. B.; Passoja, D. E.; Paullay, A. J. *Nature* **1984**, *308*, 721–722.
- [67] Van der Waals, J. D. *Over de Continuïteit van den Gas-en Vloeïstoftoestand*; Sijthoff, 1873; Vol. 1.
- [68] Langmuir, I. *Journal of the American chemical society* **1916**, *38*, 2221–2295.
- [69] Langmuir, I. *Journal of the American chemical society* **1917**, *39*, 1848–1906.
- [70] Fox, H.; Zisman, W. *Journal of Colloid Science* **1950**, *5*, 514–531.
- [71] Fox, H.; Hare, E.; Zisman, W. *The Journal of Physical Chemistry* **1955**, *59*, 1097–1106.
- [72] Zisman, W. A. *Relation of the equilibrium contact angle to liquid and solid constitution*; ACS Publications, 1964.
- [73] Girifalco, L.; Good, R. J. *The Journal of Physical Chemistry* **1957**, *61*, 904–909.
- [74] Good, R. J.; Girifalco, L. A.; Kraus, G. *The Journal of Physical Chemistry* **1958**, *62*, 1418–1421.
- [75] Good, R. J.; Girifalco, L. *The Journal of Physical Chemistry* **1960**, *64*, 561–565.
- [76] Fowkes, F. M. *The Journal of Physical Chemistry* **1962**, *66*, 382–382.

- [77] Shuttleworth, R. *Proceedings of the physical society. Section A* **1950**, *63*, 444.
- [78] Nadermann, N.; Hui, C.-Y.; Jagota, A. *Proceedings of the National Academy of Sciences* **2013**, *110*, 10541–10545.
- [79] O’connell, P.; McKenna, G. *Science* **2005**, *307*, 1760–1763.
- [80] Style, R. W.; Boltyanskiy, R.; Che, Y.; Wettlaufer, J.; Wilen, L. A.; Dufresne, E. R. *Physical review letters* **2013**, *110*, 066103.
- [81] Xu, Q.; Jensen, K. E.; Boltyanskiy, R.; Sarfati, R.; Style, R. W.; Dufresne, E. R. *Nature communications* **2017**, *8*, 555.
- [82] Jensen, K. E.; Style, R. W.; Xu, Q.; Dufresne, E. R. *Physical Review X* **2017**, *7*, 041031.
- [83] Schulman, R. D.; Trejo, M.; Salez, T.; Raphaël, E.; Dalnoki-Veress, K. *Nature communications* **2018**, *9*, 982.
- [84] Maugis, D. *Contact, adhesion and rupture of elastic solids*; Springer Science & Business Media, 2013; Vol. 130.
- [85] Derjaguin, B. V.; Muller, V. M.; Toporov, Y. P. *Journal of Colloid and interface science* **1975**, *53*, 314–326.
- [86] Muller, V. M.; Yushchenko, V. S.; Derjaguin, B. V. *Journal of Colloid and Interface Science* **1983**, *92*, 92–101.
- [87] Maugis, D. *Journal of colloid and interface science* **1992**, *150*, 243–269.
- [88] Tabor, D. *Plenary and Invited Lectures*; Elsevier, 1977; pp 3–14.
- [89] Muller, V.; Yushchenko, V.; Derjaguin, B. *Journal of Colloid and Interface Science* **1980**, *77*, 91–101.
- [90] Griffith, A. A. *Phil. Trans. Roy. Soc. A* **1921**, *221*, 163–198.
- [91] Irwin, G. R. *Trans. ASME, Ser. E, J. Appl. Mech.* **1957**, *24*, 361–364.
- [92] Gent, A.; Kinloch, A. *Journal of Polymer Science Part A-2: Polymer Physics* **1971**, *9*, 659–668.
- [93] Andrews, E.; Kinloch, A. J. *Proceedings of the Royal Society of London. A. Mathematical and Physical Sciences* **1973**, *332*, 401–414.
- [94] Andrews, E.; Kinloch, A. J. *Proceedings of the Royal Society of London. A. Mathematical and Physical Sciences* **1973**, *332*, 401–414.
- [95] Gent, A.; Schultz, J. *The Journal of Adhesion* **1972**, *3*, 281–294.

- [96] Gent, A.; Petrich, R. *Proceedings of the Royal Society of London. A. Mathematical and Physical Sciences* **1969**, *310*, 433–448.
- [97] Williams, M. L.; Landel, R. F.; Ferry, J. D. *Journal of the American Chemical Society* **1955**, *77*, 3701–3707.
- [98] Sneddon, I. Crack Problems in the Theory of Elasticity. Developments in Theoretical and Applied Mechanics: Proceedings of the Third Southeastern Conference on Theoretical and Applied Mechanics. 2013; p 73.
- [99] Peykova, Y.; Guriyanova, S.; Lebedeva, O. V.; Diethert, A.; Müller-Buschbaum, P.; Willenbacher, N. *International journal of adhesion and adhesives* **2010**, *30*, 245–254.
- [100] Holm, R. *Electric contacts: theory and application*; Springer Science & Business Media, 2013.
- [101] Hyun, S.; Pei, L.; Molinari, J.-F.; Robbins, M. O. *Physical Review E* **2004**, *70*, 026117.
- [102] Pohrt, R.; Popov, V. L. *Physical Review Letters* **2012**, *108*, 104301.
- [103] Bush, A.; Gibson, R.; Thomas, T. *Wear* **1975**, *35*, 87–111.
- [104] Carbone, G.; Bottiglione, F. *Journal of the Mechanics and Physics of Solids* **2008**, *56*, 2555–2572.
- [105] Persson, B. *The European Physical Journal E* **2002**, *8*, 385–401.
- [106] Briggs, G.; Briscoe, B. *Nature* **1976**, *260*, 313.
- [107] Deng, W.; Kesari, H. *Modelling and Simulation in Materials Science and Engineering* **2017**, *25*, 055002.
- [108] Desaguliers, J. T. *A course of experimental philosophy*; John Senex, 1734; Vol. 1.
- [109] Tomlinson, G. *The London, Edinburgh, and Dublin philosophical magazine and journal of science* **1929**, *7*, 905–939.
- [110] Coulomb, C. A. *Théorie des machines simples en ayant égard au frottement de leurs parties et à la roideur des cordages*; Bachelier, 1821.
- [111] Hisakado, T. *Bulletin of JSME* **1970**, *13*, 129–139.
- [112] Stribeck, R. *Kugellager für beliebige Belastungen*; Buchdruckerei AW Schade, Berlin N., 1901.
- [113] Stribeck, R. *Zeitschrift des Vereines Deutscher Ingenieure* **1902**, *46*, 1341–1348.

- [114] Hersey, M. D. *Journal of the Washington Academy of Sciences* **1914**, *4*, 542–552.
- [115] Ruina, A. *Journal of Geophysical Research: Solid Earth* **1983**, *88*, 10359–10370.
- [116] Thompson, P. A.; Robbins, M. O. *Science* **1990**, *250*, 792–794.
- [117] Gourdon, D.; Israelachvili, J. N. *Physical Review E* **2003**, *68*, 021602.
- [118] Urbakh, M.; Klafter, J.; Gourdon, D.; Israelachvili, J. *Nature* **2004**, *430*, 525–528.
- [119] Yurdumakan, B.; Nanjundiah, K.; Dhinojwala, A. *The Journal of Physical Chemistry C* **2007**, *111*, 960–965.
- [120] Schallamach, A. *Proceedings of the Physical Society. Section B* **1953**, *66*, 386.
- [121] Greenwood, J.; Tabor, D. *Proceedings of the Physical Society* **1958**, *71*, 989.
- [122] Schallamach, A. *Wear* **1963**, *6*, 375–382.
- [123] Best, B.; Meijers, P.; Savkoor, A. *Wear* **1981**, *65*, 385–396.
- [124] Rand, C. J.; Crosby, A. J. *Applied physics letters* **2006**, *89*, 261907.
- [125] Vella, D.; Boudaoud, A.; Adda-Bedia, M. *Physical review letters* **2009**, *103*, 174301.
- [126] Kolinski, J. M.; Aussillous, P.; Mahadevan, L. *Physical review letters* **2009**, *103*, 174302.
- [127] Kar, K. K.; Bhowmick, A. K. *Journal of applied polymer science* **1997**, *64*, 1541–1555.
- [128] Persson, B. N. *Journal of Physics: Condensed Matter* **2006**, *18*, 7789.
- [129] Li, Q.; Popov, M.; Dimaki, A.; Filippov, A.; Kürschner, S.; Popov, V. *Physical review letters* **2013**, *111*, 034301.
- [130] Popov, V. L.; Dimaki, A.; Psakhie, S.; Popov, M. *Scientific reports* **2015**, *5*, 11139.
- [131] Schallamach, A.; Grosch, K. *Mechanics of pneumatic tires* **1981**, *5*, 365–474.
- [132] Defante, A. P.; Burai, T. N.; Becker, M. L.; Dhinojwala, A. *Langmuir* **2015**, *31*, 2398–2406.
- [133] Tyrode, E.; Liljeblad, J. F. *The Journal of Physical Chemistry C* **2013**, *117*, 1780–1790.

- [134] Bright, L. K.; Baker, C. A.; Agasid, M. T.; Ma, L.; Aspinwall, C. A. *ACS applied materials & interfaces* **2013**, *5*, 11918–11926.
- [135] Chaudhury, M. K. *Materials Science and Engineering: R: Reports* **1996**, *16*, 97–159.
- [136] Zeng, H.; Konicek, A. R.; Moldovan, N.; Mangolini, F.; Jacobs, T.; Wylie, I.; Arumugam, P. U.; Siddiqui, S.; Carpick, R. W.; Carlisle, J. A. *Carbon* **2015**, *84*, 103–117.
- [137] Auciello, O.; Pacheco, S.; Sumant, A. V.; Gudeman, C.; Sampath, S.; Datta, A.; Carpick, R. W.; Adiga, V. P.; Zurcher, P.; Ma, Z.; Yuan, H.-c.; Carlisle, J. A.; Kabius, B.; Hiller, J.; Srinivasan, S. *IEEE Microwave Magazine* **2007**, *8*, 61–75.
- [138] Sumant, A. V.; Grierson, D. S.; Gerbi, J. E.; Birrell, J.; Lanke, U. D.; Auciello, O.; Carlisle, J. A.; Carpick, R. W. *Advanced Materials* **2005**, *17*, 1039–1045.
- [139] Härtl, A.; Schmich, E.; Garrido, J. A.; Hernando, J.; Catharino, S. C.; Walter, S.; Feulner, P.; Kromka, A.; Steinmüller, D.; Stutzmann, M. *Nature materials* **2004**, *3*, 736.
- [140] Fuentes-Fernandez, E.; Alcantar-Peña, J.; Lee, G.; Boulom, A.; Phan, H.; Smith, B.; Nguyen, T.; Sahoo, S.; Ruiz-Zepeda, F.; Arellano-Jimenez, M.; Gurman, P.; Martinez-Perez, C.; Yacaman, M.; Katiyar, R.; Auciello, O. *Thin Solid Films* **2016**, *603*, 62–68.
- [141] Khanal, S. R.; Gujrati, A.; Vishnubhotla, S. B.; Nowakowski, P.; Bonifacio, C. S.; Pastewka, L.; Jacobs, T. D. *Surface Topography: Metrology and Properties* **2018**, *6*, 045004.
- [142] Gujrati, A.; Khanal, S. R.; Pastewka, L.; Jacobs, T. D. *ACS applied materials & interfaces* **2018**, *10*, 29169–29178.
- [143] Church, E. L.; Takacs, P. Z. Effects of the nonvanishing tip size in mechanical profile measurements. *Optical Testing and Metrology III: Recent Advances in Industrial Optical Inspection*. 1991; pp 504–514.
- [144] Ramisetty, S. B.; Campaña, C.; Anciaux, G.; Molinari, J.-F.; Müser, M. H.; Robbins, M. O. *Journal of Physics: Condensed Matter* **2011**, *23*, 215004.
- [145] Deruelle, M.; Hervet, H.; Jandeau, G.; Leger, L. *Journal of adhesion science and technology* **1998**, *12*, 225–247.
- [146] Wald, M.; Considine, J.; Turner, K. *Experimental Mechanics* **2013**, *53*, 931–941.
- [147] Chaudhury, M. K.; Whitesides, G. M. *Science* **1992**, *255*, 1230–1232.

- [148] Persson, B. *Wear* **2003**, *254*, 832–834.
- [149] Heinrich, G.; Klüppel, M. *Wear* **2008**, *265*, 1052–1060.
- [150] Zhang Newby, B.-m.; Chaudhury, M. K. *Langmuir* **1997**, *13*, 1805–1809.
- [151] Denn, M. M. *Annual Review of Fluid Mechanics* **2001**, *33*, 265–287.
- [152] Rubinstein, S.; Cohen, G.; Fineberg, J. *Physical review letters* **2006**, *96*, 256103.
- [153] Viswanathan, K.; Sundaram, N. K.; Chandrasekar, S. *Soft matter* **2016**, *12*, 5265–5275.
- [154] Viswanathan, K.; Sundaram, N. K.; Chandrasekar, S. *Soft matter* **2016**, *12*, 9185–9201.
- [155] Viswanathan, K.; Sundaram, N. K. *Wear* **2017**, *376*, 1271–1278.
- [156] Viswanathan, K.; Mahato, A.; Chandrasekar, S. *Physical Review E* **2015**, *91*, 012408.
- [157] Bowden, F.; Tabor, D. *British Journal of Applied Physics* **1966**, *17*, 1521.
- [158] Ludema, K.; Tabor, D. *Wear* **1966**, *9*, 329–348.
- [159] Savkoor, A.; Briggs, G. *Proceedings of the Royal Society of London. A. Mathematical and Physical Sciences* **1977**, *356*, 103–114.
- [160] Wang, Y.; Dhong, C.; Frechette, J. *Physical review letters* **2015**, *115*, 248302.